Author:
Monroy Ruz, Jorge A

Title:
Spatial and spectral control of diamond NV centres for scalable spin-photon interfaces.

Heterogeneous integration of nanodiamonds with silicon nitride photonics for quantum optical technologies

Spatial and spectral control of diamond NV centres for scalable spin-photon interfaces.

Heterogeneous integration of nanodiamonds with silicon nitride photonics for quantum optical technologies

By

JORGE ARTURO MONROY RUZ

Quantum Engineering Centre for Doctoral Training
UNIVERSITY OF BRISTOL

A dissertation submitted to the University of Bristol in accordance with the requirements of the degree of DOCTOR OF PHILOSOPHY in the Faculty of Science.

SEPTEMBER 2021

Abstract

There is a global effort to implement networks capable of distributing quantum entanglement. In this context, nodes based on spins in solid state have been identified as one of the most viable routes towards achieving large scale quantum networks. For this reason, the development of scalable and efficient spin-photon interfaces is crucial. While there has been plenty of work on increasing both photon extraction efficiency and the entangling fidelity between these spin-photon systems, many of these implementations are only possible in restrictive a research facility environment or using materials difficult to produce in mass leading to issues of scalability.

The purpose of the research described in this thesis focuses on this last point: working towards the design and fabrication of scalable spin-photon interfaces. The approach explored here combines the inclusion of nanoparticles hosting spin defects with foundry compatible photonic platforms. From the selection of a spin defect and a photonics platform, to the design, fabrication and testing of nanophotonic structures around deterministically positioned spin defects, this thesis details the first steps required for demonstrating the scope of the proposed approach.

It was found that negatively charged nitrogen vacancy centres (NV^-) in nanodiamonds are compelling spin systems to test this approach with. Furthermore, research proved that it is possible to integrate NV^- centres with silicon nitride photonics by modifying the silicon nitride's stoichiometry, thereby suppressing its immanent photoluminescence. This allows for the detection of NV^- centres buried within the silicon nitride. It was also found that it is possible to attain spatial control of the nanodiamonds using scalable lithographic deposition methods. Finally, the fabrication of optical resonators designed to both increase the collection efficiency and enhance the NV^- centre zero phonon line emission was demonstrated.

Whilst the results shown here present several challenges and opportunities for improvement, they also show a promising path towards the fabrication of scalable spin-photon interfaces.

Dedication and acknowledgements

There is a big list of people in Bristol and abroad that have supported me and have contributed to the completion of this journey who I would like to thank.

First and foremost, I would like to thank my supervisor Krishna for his guidance, patience and encouragement as well as the never-ending stream of exciting ideas that made (and continue to make) every weekly meeting a boost of motivation.

Thank you, John, for always making the time to catch up and for providing invaluable insight to the project. A big thank you to my fellows in the diamond team, Joe Smith and Cecile Skoryna Kline. Together we have formed a fantastic team with complimentary skills. Thank you both, for your patience and understanding always. A big thank you to Andrew Murray and Pisu Jiang for all the advice in the cleanroom.

I would like to thank CONACYT and Mexico's government for the funding that gave me the opportunity to pursue this goal. Special gratitude to the CDT management past and present (Pete, Andrea, Lin, Jorge, Becky, Sorrel and all CDT lecturers) and QETLabs for funding and supporting my position at the University. Thank you for believing I was a valuable addition to the programme and for always being there to help. Big shout out to the QET Labs ops team that make everything run smoothly and are always ready to support the students.

To my friends from Cohort 3 (Brian, David, George, Giorgos, Joe, Konstantina, Max, Rachel, Ross, and Will). Thank you for being my first UK family. Thank you, Max, for your friendship from day one, and for helping me to learn fast about the life in the UK. Thank you to the Hawthornes' Friday company for providing a great place to bounce science ideas off of each other in the friendliest environment. Thank you to Angie, Francesca and Estelle for all the caring and support. You are incredible friends. Thank you to Becky and Sam for being extraordinary neighbours and friends. Thank you all of my extended family and friends in the UK, Mexico, and beyond, for always offering a kind ear or word of support.

I would like to thank Alison, Ian, Holly, Imi, Digby, Lily and Keith for letting me be a part of your beautiful family in Bristol and for supporting me unconditionally. Thank you, Holly, for being the most supportive, loving, encouraging, and understanding partner anyone would hope to have. You have lifted me up in the most difficult days. Without you

this would not have been possible.

Finally I would like to dedicate this thesis to my family. In particular, to the memory of my dad, who gave everything he had to get me here. He was my strongest supporter and mentor for all but the last few months of my doctoral degree. This is for him, Mum and Ale. Your unconditional love and support has been indispensable. Thank you, always.

COVID-19 Statement

The following statement is a summary of planned research activities disrupted by Covid-19 restrictions and the extent to which the work included in this thesis was impacted and adapted in the circumstances.

This research project was primarily focused on the in-house fabrication and testing of nanophotonic devices. The fabrication of these devices was done using the cleanroom facilities at the University of Bristol in the School of Physics, and the testing of the devices was done in two of the University's laboratories. This research was significantly affected by the closure of these facilities and access restrictions due to the COVID-19 pandemic. The total closure of facilities from March to July 2020 resulted in a four-month delay on the planned experimental work. Furthermore, after some restrictions were lifted, room capacity limitations disrupted the time allowed in the facilities which mainly limited turn around speed of the iterations made in the nanofabrication processes.

The results shown in section 4.2.2 of this thesis are results obtained on numerical simulations carried out during the complete closure of the facilities as an adaptation due to the circumstances, and were not originally planned to be part of this thesis. Although these additions proved to be valuable for the project, the impact on the practical work was critical. Experiments requiring fully functional versions of the devices shown in chapter 5 were curtailed by the emergency. The four months of closure would have provided enough time to fix the lithography overlay issues encountered on the fabrication on the devices and consequently allowed said experiments.

AUTHOR'S DECLARATION

I declare that the work in this dissertation was carried out in accordance with the requirements of the University's *Regulations and Code of Practice for Research Degree Programmes* and that it has not been submitted for any other academic award. Except where indicated by specific reference in the text, the work is the candidate's own work. Work done in collaboration with, or with the assistance of, others, is indicated as such. Any views expressed in the dissertation are those of the author.

SIGNED: ..... DATE: .....

Table of Contents

List of Tables

Table **Page**

List of Figures

Figure **Page**

CHAPTER 1

INTRODUCTION AND THESIS PLAN

The development of quantum mechanics at the beginning of the twentieth century provided a theory to understand and exploit collective behaviour of matter and light, providing technologies like lasers and semiconductor integrated circuits that drastically changed the way people live and perceive the world. Whilst these revolutionary technologies were made possible through quantum mechanics, the use of the term *Quantum Technologies* at least over the last two decades does not refer to all the technologies developed through the use of quantum mechanics. Instead, *Quantum Technologies* refers to technologies that harness the benefits that can be found in *storing* and *transmitting* information encoded in quantum states of light and matter.

Concepts like quantum computation, quantum communication and quantum sensing fall under the umbrella of what could more accurately be called **Quantum Information Technologies**. These broad areas of research share the aim of taking advantage of the unique properties that quantum systems exhibit, to surpass the known limits of their classical counterparts. Theoretical work has shown that by encoding information in quantum states, it is possible to achieve communications that are protected by the fundamental quantum nature of the information carriers [1], to build sensors that surpass the sensitivity allowed by classical information theory [2], and to compute problems that are classically intractable [3][4].

To implement said schemes, special infrastructure like quantum networks is needed.

There is a global effort in the quantum information technology community to develop quantum coherent networks comprised of nodes, that are capable of processing quantum information and communication channels between nodes, where quantum information can be potentially distributed over long distances. In the simplest version of a quantum network, the node would be formed by a stationary qubit in which information can be stored, manipulated and coherently transferred to a quantum information carrier, or flying qubit, that in turn moves the information to the next node.

Although remarkable proof-of-principle physical implementations have been demonstrated over the last few years [5], for these technologies to become practical, the size of the networks and the rate at which quantum information can be distributed needs to scale up. This poses the challenge of finding ways of building nodes that can not only handle quantum information with exquisite control, but that can be reproduced thousands of times.

Solid state spin defects are promising systems that can be used as nodes in a future quantum network. There are particular material defects with spin dependant optical transitions that are capable of transferring quantum information to optical photons. However, to efficiently use these photons, photonic structures need to be formed around the defect, creating the challenge of fabricating photonic devices with materials hosting the defects.

The aim of this thesis is to explore an alternative way of building spin-photon interfaces based on a solid state spin defect. The approach proposed here is to rely on the scalability shown by the mass production of photonic circuits. Whilst foundry photonic platforms do not usually use the materials that host the spin defects of interest, it should be possible to integrate the spin defects with photonic circuits by taking **nanoparticles** of the material hosting the spin defects and incorporating them within the material layers used to build the photonic circuits. This way, photonic structures such as optical resonators, waveguides and splitters can be patterned around single spin defects with the quality and reproducibility that foundry photonics have to offer.

1.1 Thesis layout

In this thesis, the initial steps to fabricate scalable spin-photon interfaces based on the integration of nanoparticles with commercially available photonic platforms are shown.

Chapter 2 will present some of the main reasons to use nitrogen vacancy (NV^-) centre in diamond for the approach proposed in this project. A quick review of the NV^- centre's physical system and the key features to look out for throughout this thesis are detailed. Also, some of the work done to create spin-photon interfaces using NV^- centres in diamond is analysed, highlighting the strengths and challenges in these demonstrations and motivating the nanoparticle integration approach proposed in this project.

In chapter 3, materials that would allow the integration of solid state spin defects and the building of quantum photonic circuits with platforms are discussed. This exploration leads to the conclusion that silicon nitride (Si_3N_4) is most likely to give the optimal results, although background photoluminescence in this material poses a major challenge. Efforts were therefore made to modify the photoluminescence of the in-house deposited silicon nitride films, enabling measurements to be taken of single NV centres encapsulated within the material.

For devices built using the proposed nanoparticle integration approach to be considered scalable, spatial control over the defects is needed. Chapter 4 presents the efforts taken to attain spatial control over NV^- centres. The implications of the method used in terms of yield and scalability are discussed. Methods to identify the orientation of the NV^- centres and the effect the orientation has on the emission rate and collection efficiency are explored as well as the scope of using orientation and brightness information to identify single emitters.

Once a material has been chosen and deterministic positioning of the NV^- centres has been achieved, the fabrication of photonic structures around the NV^- centres can be achieved. Chapter 5 describes the design, fabrication and characterisation procedures of optical resonators made to increase the collection efficiency and to enhance the NV^- centres zero phonon line emission, showing that the nanoparticle integration technique has exciting potential for future development.

Finally, chapter 6 summarises the key points throughout the thesis and presents a list of the improvements needed that are part of the future work and scope of this project.

CHAPTER 2

BACKGROUND: SOLID STATE SPIN-PHOTON INTERFACES AND NV^- CENTRES

The work presented here including the construction of the confocal microscope setup, and the characterisation measurements are my own

Through the development of technologies based on condensed matter physics, defects in solid state matter have taken the roles of both the villain and the hero. Whilst for some applications defects are detrimental, for some other applications they represent a whole complex system that can exhibit unique properties. Defects in solid-state that have electronic spin states that can be linked to optical transitions, and are capable of transferring the quantum state from the spin state to the photon state, are of great interest for the implementation of quantum networks.

One of the most studied spin defects for quantum information purposes is the NV^- centre in diamond, for its unrivalled long electron spin state coherence time at room temperature along with the mechanism of reading out the electron spin state through optical transitions. These characteristics have led to the demonstration of the violation of Bells inequalities, whilst simultaneously closing the causality and measurement loopholes [6], and more recently the demonstration of the distribution of entanglement between three nodes [5], placing the NV^- centre at the forefront of the development

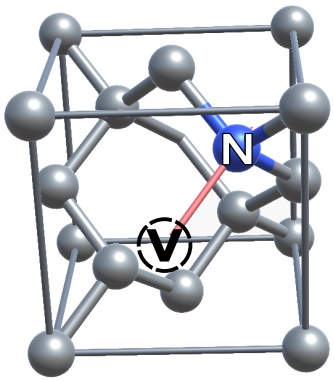

Figure 2.1: Nitrogen-vacancy (NV) centre in diamond. The NV centre is formed by the substitution of a carbon C atom (grey) with a nitrogen N (blue) atom and by a vacancy in the lattice (dashed line).

of spin-photon interfaces. However, the rate at which the entanglement was created between the nodes of those demonstrations is rather low, and is unsuitable for the implementation of practical applications. The low rate at which entanglement can be achieved is a consequence of the non-ideal optical properties of the NV^- centre, and methods for overcoming these restrictions have been the main focus of research into spin-photon interfaces using NV^- centres.

For the work presented in this thesis the NV^- centre is used as the spin system to integrate, despite the challenges that the poor optical properties generate. Whilst other spin defects with better optical properties might be explored in the future, the NV^- centres in nanodiamonds represented an ideal "test pilot" for initially exploring the integration with foundry photonics due to its room temperature spin coherence and the amount of research that has already been done into the electronic structure of the defect.

2.1 NV^- centres in diamond

The nitrogen-vacancy (NV) is a point defect with trigonal symmetry (C_{3v} point group) in the diamond lattice, formed by the substitution of a C atom by a N atom and by a vacant site in the lattice (figure 2.1). Although NV centres can exist in the neutral charge state NV^0, the negatively charged state NV^- has attracted more attention for quantum information technologies due to its remarkable spin properties, which are explained later in this section.

The symmetry of the defect and the number of unbonded electrons in the defect define which molecular orbitals the electrons can occupy. In the NV^- charge state, six electrons are involved. Five unbonded electrons coming from the dangling bonds of the carbon atoms and the nitrogen atom, plus an additional electron from a nearby donor, occupy two molecular orbitals with A symmetry (a and a') and a doubly degenerate molecular orbital E (ex,ey) [7]. First-principle calculations predicted that the molecular orbital a' has the lowest energy and lies in the diamond valence band (VB) [8]. The other two orbitals, however, are highly localised and have energies within the diamond wide band-gap (5.5 eV) making the NV^- centre a *deep defect* with a $^3A_2$ triplet ground state and a ^3E triplet excited state as pictured in figure 2.2 a). This is one of the many attractive features of the defect, since the transitions used for quantum information purposes do not involve the valence band (VB) or the conduction band (CB).

2.1.1 Spin properties

The structures of the $^3A_2$ triplet ground state are determined by the following Hamiltonian:

$$\hat{H} = \Delta_{gs}\hat{S_z}^2 + g_{gs}\mu_B\vec{\mathbf{B}}\cdot\hat{\mathbf{S}} + \hat{H_{HF}} \tag{2.1}$$

where Δ_{gs} is the zero-field-splitting with a value Δ_{gs} =2.87 GHz, $\hat{\mathbf{S}}$ is the electron spin operator with $\hat{S_z}$ the component along the z-axis (taken as the N-V axis), g_{gs} is the Lande g-factor, and μ_B with $g_{gs}\mu_B = 2\gamma$ =2.8 MHz/G. The term $\hat{H_{HF}}$ encompasses the spin-spin and spin-orbit interactions with the nuclear spins nearby (hyperfine interactions).

This Hamiltonian shows that even in the absence of an external magnetic field, the m_s =0 and $m_s = \pm 1$ states are split due to spin-spin interactions. The presence of an external magnetic field breaks the degeneracy between the sub levels $m_s = +1$ and $m_s = -1$ (figure 2.2 b). For quantum information implementations the spin state m_s =0 and one of the m_s =1 states are used as the $|0\rangle$ and $|1\rangle$ states respectively. The single qubit gates can be implemented by applying microwave (MW) pulses with the frequency of the transition and delivered with a MW antenna near the sample.

There are two strong motivations for choosing the NV^- centre as the spin defect to demonstrate the proposed approach of scalable integration. The first one is that even

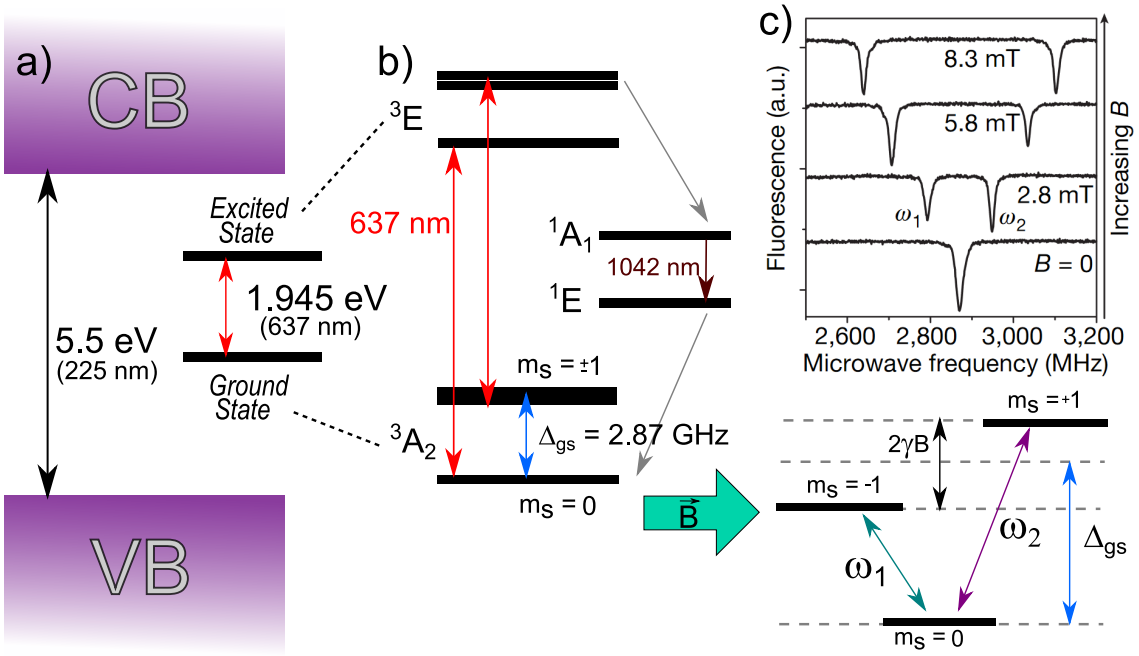

Figure 2.2: Fine structure of the $^3A_2$ triplet ground state. a) Energy of the NV^- centres ground and excited states with respect to the valence band (VB) and conductive band (CB). b) Fine structure of the triplet ground and excited states as well as the intermediate singlet states. In the bottom right corner the splitting generated by the application of an external magnetic field is shown. c) Example of optically detected magnetic resonance (ODMR) measurements for different values for the intensity of the external magnetic field applied. This plot is taken from [9]

.

at room temperature, the coherence time (T_2) of the NV^- centre electron spin state can be as long as 700 μs for bulk diamond [10] and 400 μs for nanodiamonds [11], both with natural isotopic abundance of ^{13}C. Furthermore, these times can be extended using Carr-Purcell-Meiboom-Gill (CPMG) microwave pulse sequences reaching times on the order of 10 ms at cryogenic temperatures [12]. The T_2 is a critical parameter for the use of the spin state as part of a node in a quantum network, since it defines the timescales required for control, initialisation and measurement [13]. In a spin defect, T_2 is typically limited by the magnetic local environment. For the NV^- centre in bulk diamond the magnetic environment is close to ideal, since most of the atoms surrounding the defect (carbon isotope ^{12}C) have no nuclear spin, with the exceptions of the nitrogen (^{14}N) atom in the vacancy, other nearby ^{14}N atoms and the few (< 2%) ^{13}C. A long spin coherence time at room temperature allows for faster testing of devices through the exploratory stage of this project.

The second reason this defect was chosen has to do with the spin state read-out mechanism. The transition between the $^3A_2$ ground and the ^3E excited triplet states is an optical spin-preserving transition, meaning that the optical excitation of the electron state does not directly change the spin state. However, when the electron spin state is $m_s = +1$ or $m_s = -1$, and is excited into the triplet excited system, there is a non-negligible chance that the system decays via two intermediate singlet states ($^1A_1$ and ^1E). The decay from the excited state to the $^1A_1$ and the decay from the singlet state ^1E are non-radiative, whilst the decaying between the two singlet states produces a photon on the near infra-red region of the spectrum (1042 nm). This decaying route leads exclusively to the m_s =0 ground state as pictured in figure 2.2 b). This means that the decay from the singlet state ^1E produces spin polarisation.

In practice, this phenomenon is observed as electron spin state dependant fluorescence, which provides a mechanism to read-out the spin state even at room temperature. Spin state dependant fluorescence is the basis of a technique called optically detected magnetic resonance (ODMR). What this means is that this mechanism can be used to find the exact energy transition between electron spin states, as pictured in figure 2.2 c) taken from the work of Balasubramanian and co-authors [9]. By sweeping the frequency of MW pulses radiated by an antenna near the NV^- centre, dips in the fluorescence appear, with the minimum being the precise transition frequency between the spin states. The plot shows that the separation between the two dips depends on the magnetic field applied. It also shows that in the absence of an external magnetic field $B = 0$ the $m_s = \pm 1$ shows a signal dip due to the degeneracy.

2.1.2 Optical properties

Whilst the spin properties of the NV^- centre are very promising, the optical properties present a more challenging scenario. The transition between the $^3A_2$ ground and the ^3E excited triplet states is an optical transition with a zero-phonon line (ZPL) of 1.945 eV that corresponds to a wavelength of λ_{ZPL} =637.4 nm. The spectral coherence of this transition is hindered by the efficient coupling of optical phonons from the lattice. These phonons allow incoherent above-resonance excitation (commonly done with a 532 nm laser shown in figure 2.3). After a few picoseconds, the NV decays to the excited state, and a few nanosecond after, the NV excited state decays again. This causes some of the energy to get carried away by the phonons, creating a broad phonon side-band (PSB) in the photoluminescence (PL) spectrum. An example of an NV^- centre spectrum at room

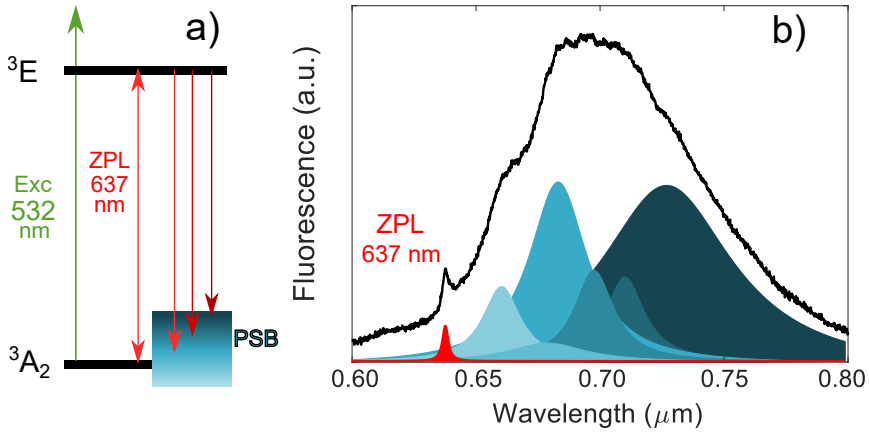

Figure 2.3: NV^- centre spectrum. Upon above-resonance excitation (usually with a green laser with wavelength 532 nm) the NV^- centre emission fluorescence comes from the zero-phonon-line (ZPL) and the phonon-side band (PSB).

temperature can be seen in figure 2.3 b). From this image it is clear that the contribution of the PSB dominates the emission. The ratio between the pure radiative decay (ZPL) and the phonon assisted radiative decay (PSB) is known as the Debye-Waller factor and for an NV^- centre in bulk diamond it is only between 3-4% even at low temperatures.

Due to the symmetry of the excited state ^{3}E, the radiative decay into the ground state is associated with a degenerate dipole transition (x and y directions) perpendicular to the symmetry axis, which corresponds to the axis that connects the N atom, and the vacancy site also denoted N-V axis. Understanding the emission pattern of the defect is important because it determines the strategies that need to be followed to recover the emitted light. This emission pattern can be modeled as the emission of two orthogonal electric dipoles in the plane perpendicular to the N-V axis. At low temperatures, the degeneracy can be broken by the presence of mechanical stress comparable with the spin-spin and spin-orbit interaction [14] electric fields.

The energy level structure described in this section is for NV^- centres at room temperature. At low temperature, the excited state splits into a richer structure. Whilst describing in detail the structure of the excited triplet state at cryogenic temperatures is beyond the scope of this thesis, it is worth pointing out that within the transitions in this richer structure there are some that involve a change electronic orbital angular momentum. One of the most used methods to generate spin-photon entanglement is through the use of these transitions [15].

For the realisation of quantum networks, it is not just necessary to have entanglement between the NV^- centre spin and a photon; a protocol to entangle two nodes (i.e. two spins in different NV^- centres) is also needed. This is commonly called entanglement distribution and the most common technique is to use heralded entanglement [16][17], where the entanglement of two spin-photon pairs of two separate NV^- centres gets converted to spin-spin entanglement upon the interference of the photons in a beamsplitter. If the photons coming from the two NV^- centres are indistinguishable in every regard except for the degree of freedom that is entangled with their respective electron spin, then coincidence detection of the photons projects the NV^- centre spin state onto an entangled state.

For solid-state spin defect systems, one of the limiting factors of the entanglement rates using two-photon interference is the coupling of the emission with phonons in the lattice. Only photons emitted on the zero phonon line (ZPL) can be indistinguishable, as photons emitted on the phonon side band (PSB) leave "which-path" information on the crystal vibrations. This essentially means that photons in the PSB can not be truly indistinguishable because they are entangled with phonons in the crystal lattice. The use of optical cavities has been the paradigmatic solution for enhancing the emission of a quantum emitter into the ZPL and demonstrations of emitters coupled to optical cavities producing photons with high indistinguishability are available in the literature [18][19]. Unfortunately, indistinguishability is limited by the vibration of the lattice. In fact, it has been shown that, for quantum dots, the use of spectral filters or even optical cavities cannot achieve near-unity efficiency and indistinguishability simultaneously since the coupling with phonons is unavoidable even at cryogenic temperatures [20].For the NV^- centres the situations is not different, and can be even worse than in quantum dots due to the low Debye-Weller factor. Nevertheless, the use of optical cavities is crucial for the development of spin-photon interfaces capable of distribute entanglement. An insightful analysis on the achievable indistinguishability with NV^- centres couple to small volume cavities is given in [21].

The next section gives a quick review of the demonstrations of NV^- centres in optical cavities.

2.2 Optical interfaces NV^- centre emission enhancement

To enhance the rate at which entanglement is distributed across a quantum network, there are two main challenges that need to be solved:

- *Collection efficiency*. For a piece of bulk diamond, the extraction of photons from an NV^- centre is limited by the total internal reflection (TIR), due to the high refractive index contrast between diamond and air. To overcome this the fabrication of micro structures around the NV^- centre have been used, with the solid immersion lenses (SIL) being the most used structure for this purpose [22]. Other approaches include diamond nanowires [23] and circular Bullseye gratings [24].

- *Spectral shaping of the NV^- centre fluorescence*. As explained before, to increase the rate of entanglement protocols it is necessary to increase the fraction of fluorescence emitted into the ZPL. The paradigmatic solution for enhancing the emission of a quantum emitter has been the use of optical cavities. In the weak coupling regime, also called Purcell regime, the enhancement is measured by the Purcell factor defined as

$$F_p = \frac{3}{4\pi^2}\left(\frac{\lambda}{n}\right)^3 \frac{Q}{V} \tag{2.2}$$

  where λ is the wavelength, n is the effective refractive index of the cavity mode, Q is the quality factor of the cavity and V is the mode volume. From this expression it is clear that high Q and small mode volume V cavities lead to high Purcell factors that increase the NV^- centre emission into the ZPL.

  There have been many demonstrations of cavities fabricated around NV^- centres with this purpose. From ring resonators [25] to one-dimensional [26][27] and two-dimensional photonic crystal cavities [28] [29], the realisation of cavities reaching Purcell factors as high as 70 can be seen in the work of Faraon *et.al.*[29].

Whilst remarkable efforts have been made to fabricate these optical cavities on bulk diamond, the fabrication undercut methods are laborious and many times the performance of the device can be hindered by the poor uniformity of the thickness of the

diamond membranes used. Also, the suspended diamond geometry used in many of these cavities reduces the versatility in terms of the allowed structures to fabricate.

The purpose of this project is to explore alternatives to using bulk diamond as the material platform for the fabrication of photonic structures such as optical cavities. The alternative proposed here is the use of nanoparticles of diamond, or nanodiamonds (NDs), to incorporate NV^- centres with other photonic materials that have proven to be more suitable for mass production.

The use of NDs as hosts of NV^- centres has been explored for various applications, from being used as bio-markers [30], to being used as magnetometers [31], and interestingly they have been proposed to be used in experiments where the connection between gravity and quantum mechanics can be tested [32][33]. For many years, the use of NV^- centres in NDs for quantum information was very limited due to their reported low spin coherence times [34][35]. However, in recent years, spin coherence times longer than 200 μs have been reported for nanodiamonds obtained from chemical vapour deposition (CVD) grown diamond either by plasma etching [36] or ball milling [11] putting NDs again in the map for pursuing many of the applications mentioned above.

For context, the NDs used in this work come from milled high-pressure high-temperature (HPHT) synthetic diamond with low concentration of impurities similar to the ones used in [37] where spin coherence times exceeding 60 μ have been reported. Although the maximum reported coherence time reported for NV^- centres in these NDs is an order of magnitude smaller that the CVD NDs, they are a good enough to test the approach of this project.

The integration of NDs with optical cavities for the extraction of indistinguishable photons from NV^- centres, has been explored before. One of the demonstrated routes has been to use open cavities formed by two independent mirrors with the ND sitting on top of one of them [38] [39][40]. An alternative route is to position the nanodiamond on top of nanophotonic structures such as two-dimensional photonic crystal cavities [41] or micro-disks [42] to enhance the NV^- centre fluorescence.

The lack of scalability of these approaches mainly originates from the random dispersion of the NDs. For example, in reference [41] the nanodiamond needs to be placed manually at the centre of the cavity with the help of an atom force microscopy (AFM) tip making the creation thousands of devices with these process unfeasible. The aim of

this project is to find a route to build devices. For this reason one of the main goals of the approach explored throughout this thesis is to achieve spatial control over the NDs.

2.3 Detecting single NV^- centres using confocal fluorescence microscopy

The most common approach to detect NV^- centres on a sample is to use confocal fluorescence microscopy. This technique consists of having an excitation source focused on the sample, usually using a high numerical aperture (NA) objective, and collecting the fluorescence using the same objective. The fluorescence is separated from the excitation optical path using either a beamsplitter or a dichroic mirror and then detected with a photo-detector placed right after the image plane where a pinhole aperture is used to filter spatially the collected light as shown in figure 2.4.

Compared with wide-field fluorescence microscopy, confocal fluorescence microscopy offers an improvement on the axial (along the optical axis) resolution. This means that only the light emitted within a small volume defined by the point spread function (PSF) of the system is detected reducing the background noise from other emitters or the substrate.

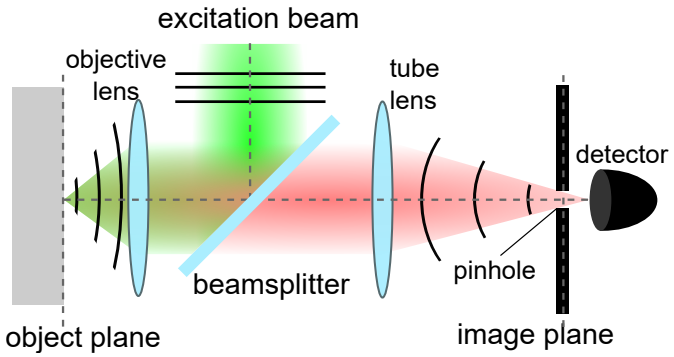

Figure 2.4: Schematic representation of a confocal fluorescence microscope. An excitation beam is focused on the object plane to produce fluorescence that, in turn is collected by the same objective lens and collimated. With the use of a beamsplitter, the fluorescence is separated from the excitation optical path and focused on the image plane by the use of a tube lens. A pinhole is placed at the image plane to achieve axial resolution. The solid lines represent the wave fronts of the excitation and fluorescence beams

2.3.1 Setup

The main tool used throughout this project was a home-built confocal microscopy setup. A schematic can be followed in figure 2.5 a). A 532 nm continuous wave (CW) excitation laser (LaserQuantum GEM) is focused on a sample using a microscope objective with a numerical apperture NA = 0.9. Before reaching the objective, the laser passes through an acousto-optic modulator (AOM) that serves as a fast switch, a polariser, and half wave plate (HWP) to control the incident polarisation on the sample.

The sample is mounted on a printed circuit board (PCB) that has an radio-frequency (RF) antenna that is used to drive the NV^- centre spin transitions. The PCB is mounted on a 3-axis stage (Thorlabs Nanomax MDT630B) with closed loop piezo-electric actuators and stepper motors for fine and coarse position control of the sample. To position the region of interest of the sample under the objective, the setup has a widefield imaging system integrated in the same path. Illumination from a white LED source can be introduced to the optical axis by the use of a removable mirror shown with a dashed line in the diagram. The sample can be observed with the aid of a CCD camera and a beamsplitter (BS).

The emitted photoluminescence (PL) from the NV^- centres is collected back with the same microscope objective and deflected from the excitation path by a dichroic mirror (DM)(Semrock FF580-FDi01) that reflects wavelengths above 580 nm. The PL signal from the NV^- centres is then passed through two additional filters, one notch filter to reject the pump (Semrock NFD01-532) and a long pass filter (LPF) to reject the Raman signal (Semrock LPBLP01-633R), and coupled to a single mode fibre (SMF) (Thorlabs 630HP). The core of the fibre is placed at the confocal plane and acts as the spatial filter instead of a pinhole aperture. The SMF is connected directly to an avalanche photo-diode (APD) (Excelitas AQRH 13-FC) in Geiger mode that creates a pulse for every detection event. These photo-detectors have an average dark counts rate of 250 counts per second. A raster scan produces an image pixel-by-pixel where the values assigned to each pixel are the number of detected photons for each of the positions. These confocal scans are generated by the synchronisation of the photon-counting logic and the displacement of the piezo stage.

An example of an image created with the setup usually called a confocal scan, is shown in figure 2.5 b). The sample consisted of a piece of diamond where a solid immersion lens (SIL) has been milled around a pre-identified NV^- centre. By etching this hemispherical

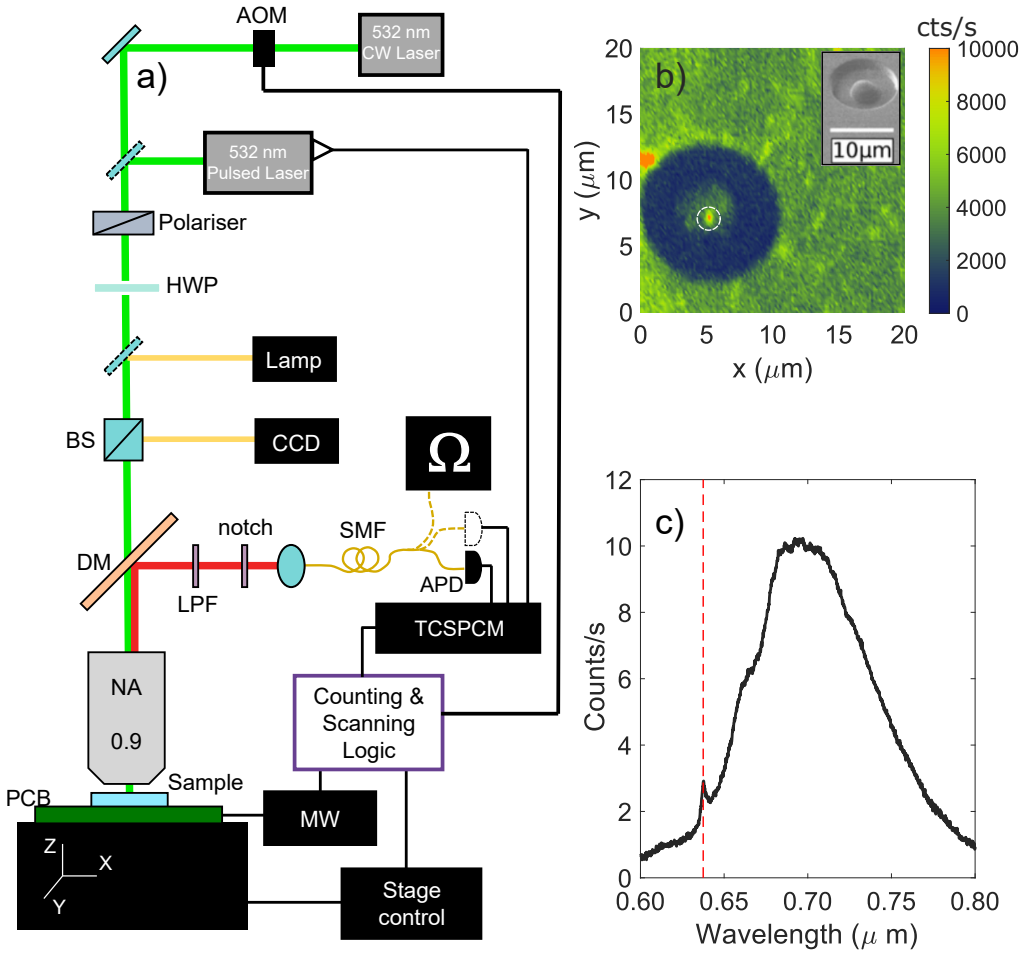

Figure 2.5: a) Schematic of the Home-built confocal microscopy setup. CW: continuous wave, AOM: acousto-optic modulator, HWP: half-wave plate, BS: beamsplitter, CCD: charge-coupled device camera, DM: dichroic mirror, PCB: printed circuit board, MW: microwave source, NA: numerical aperture, LPF: long-pass filter, SMF: single-mode fibre, APD: avalanche photo-detector, TCSPCM: time-correlated single photon counting module, Ω represents a spectrometer. b) Confocal scan of a diamond sample with a solid immersion lens (SIL) milled around a preselected NV^- centre to enhance collection efficiency. The inset in the figure shows an scanning electron microscopy image of the structure. c) Spectrum of the NV^- centre taking with the spectrometer (Ω). The dashed red line marks the zero phonon line (ZPL) wavelength.

SIL into the surface of the diamond using a focused ion beam system, the collection collection efficiency of the photons coming from the NV^- centre increases. The sample shown here is the same sample as the one used in [22]. In addition to the confocal scan, panel c) shows the spectrum of the NV^- centre in the SIL. A very clear sharp feature is seen at the NV^- centre zero phonon line.

For the measurement of the intensity auto-correlation ($g^{(2)}$) that are explained in the next section, the signal gets split by the use of a 1x2 fibre splitter (Thorlabs TG625R5B1) and each end is connected to a APD, which in turn are connected to a time-correlated single photon counting (TCSPCM) module (PicoHarp 300). For the measurement of the NV^- centre spectrum, one of the outputs of the splitter is connected to a spectrometer (Andor Shamrock 303i) equipped with an EMCCD camera (Andor Newton 940) shown in the diagram with the letter Ω.

For the lifetime measurements a pulsed laser at 532 nm (PicoQuant LDH P-FA 530B) with a repetition rate of 10 MHz and pulse widths <100 ps can be introduced to the optical axis to replace the CW laser as the excitation with the aid of a removable mirror. The internal clock of the laser and the signal of the single photon detector is connected to the TCSPCM.

To address the electron spin transition in the NV^- centres, a microwave (MW) source (Rohde and Schwartz SMB100A) is used to drive a loop antenna in the PCB. By programming synchronised pulse sequences using a high-speed, progammable pulse generator (Spincore PulseBlaster ESR-PRO), the AOM switch in the optical path and a microwave switch (Mini-Circuits ZASWA-2-50DR+) in the microwave path can be turned on and off at the right times to perform any of the common spin measurement protocols.

2.3.2 HBT measurements

For the fabrication of any type of device that requires an NV^- centre, the certainty that the device contains only one spin defect is important. Given the fact that a confocal scan is constructed only with the collected fluorescence signal from the sample, it is challenging to discern between one or many fluorescent defects that are closer to each other from the resolution of the the microscope. Therefore, additional characterisation is needed to identify single NV^- centres.

In general, the gold standard to distinguish between single and multiple quantum emitters is the use of photo-correlation measurements. Since single emitters can only emit one photon at a time, this means that there is a single-photon time signature embedded in the fluorescence collected from the emitter. To detect said signature, intensity auto-correlation ($g^{(2)}$) measurements are needed. Intensity auto-correlation is defined as:

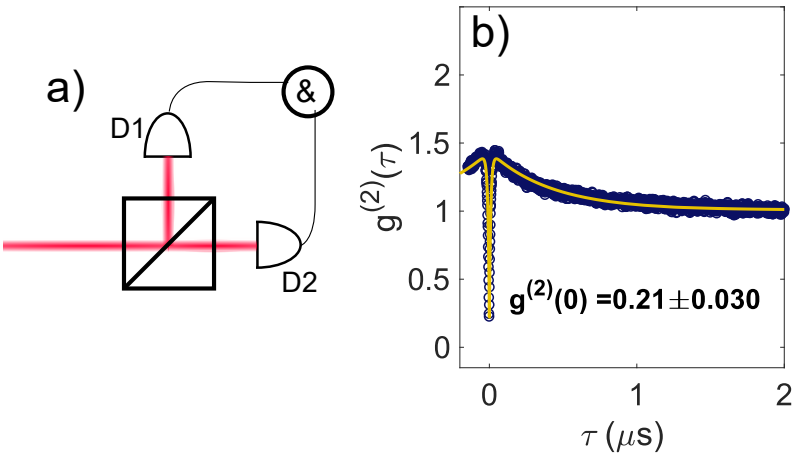

Figure 2.6: Intensity auto-correlation measurements. a) Hanbury-Brown - Twiss interferometer. The signal is split into two paths leading to photodetectors D1 and D2. Coincidence counts are registered for time windows separated by τ b) Auto-correlation measurement $g^{(2)}(\tau)$ data (blue circles) for the single NV^- centre shown in figure 2.5 b). The solid line is fitted based on the three-level model suitable for NV^- centres explained in [43].

$$g^{(2)}(\tau) = \frac{\langle I(t)I(t+\tau)\rangle}{\langle I(t)\rangle^2} \tag{2.3}$$

where $I(t)$ is the measured intensity of the signal over time t and the angled brackets $\langle\rangle$ indicate temporal average. In practice $g^{(2)}(\tau)$ can be measured by the use of a Hanbury-Brown and Twiss interferometer [44], where the signal is split in two paths by a 50:50 beamsplitter, with each path leading to single photon detectors D1 and D2 (figure 2.6 a) . This way the autocorrelation function can be obtained by recording the coincidences of photons arriving to D1 at time t and the photons arriving to D2 at time $t+\tau$ for different τ values. An auto correlation measurement from the NV^- centre in the calibration sample is shown in figure 2.6 b). The data is normalised by the value of $g^{(2)}(\tau = \infty) = 1$. The solid line shows a fitted model based on a three-level emitter like the NV^- centre [43] given by:

$$g^{(2)}(\tau) = 1 + c_2 e^{-\tau/\tau_2} + c_3 e^{-\tau/\tau_3} \tag{2.4}$$

According to quantum optical photon correlation theory, a $g^{(2)}(\tau = 0) < 1$ would statistically demonstrate non-classical behaviour of the optical signal. Furthermore,

a $g^{(2)}(\tau = 0) < 0.5$ gives a confirmation that the signal analysed comes from a single quantum emitter.

CHAPTER 3

NITROGEN-RICH SILICON NITRIDE FOR PHOTONIC INTEGRATION OF SOLID-STATE SPIN DEFECTS

*This chapter shows work that appears in Smith, Monroy-Ruz, Rarity and Balram "**Single photon emission and single spin coherence of a nitrogen vacancy centre encapsulated in silicon nitride**" [45]. The instrument control software, confocal scans, second order autocorrelation measurements, fluorescence lifetime, and Rabi nutation measurements presented in section 3.2 were performed by Joseph Smith. The rest of the work presented here is my contribution*

Most of the current approaches towards on-chip solid state spin defects coupled to photonic circuits are fabricated by etching photonic structures from the same material that hosts the spin defect. This poses a problem, as although fabrication of remarkable nanophotonic structures using host materials has been shown, the reality is that it's hard to fabricate with them and just a limited amount of geometric forms have been demonstrated. Additionally, the growth of many of these materials require conditions of pressure and temperature that are not compatible with large scale production photonic foundries. Hence, this approach has limitations on the scope of scaling to the intricate photonic circuits required for useful photonic quantum information processing.

The approach explored in this research proposes the heterogeneous integration of nanoparticles containing the spin defect of interest with materials that are readily

available at the foundry level. In this context, it is important to identify which materials are suitable for this approach.

Photonic structures like waveguides and photonic crystal cavities confine the electric field inside the material film, suggesting that the best way of integrating the nanoparticles containing spin defects is by encapsulating them within the material layer used for these devices. This way, the maximum interaction between the electric field and the atomic defect is achieved. For this reason, amorphous materials seem more suitable compared to crystalline materials. Growing crystalline materials onto irregular heterogeneous substrates presents all kinds of challenges due to the structural mismatch. A better option would be the use of an amorphous material, since the inclusion of a nanoparticle does not break the order and the material can grow around it. In addition, these amorphous materials can be deposited at relatively low temperatures, in comparison with their crystalline alternatives. There are however drawbacks to the amorphous materials, which are discussed later in this chapter.

An amorphous material useful for the approach described has to have a series of characteristics that makes them compatible with the spin defect in study. It is thought that the following criteria summarises the key features needed for integration with solid state spin defects:

1. **Low absorption in the visible spectral region.**

   Many solid state spin defects emit in the visible region of the spectrum, and therefore the chosen material needs to be transparent within that band.

2. **Low background photoluminescence (PL) in the relevant spectral band.**

   In order to successfully detect the emission from the spin defects, it is important to be able to distinguish between the optical signal coming from the emitter from the background noise. Since most of the initialisation and read-out of spins requires off-resonance excitation, it is important that the chosen material has low PL under this excitation.

3. **Preserve the intrinsic radiative quantum efficiency.**

   The embedding material should not change the intrinsic emission rate. The aim is to change the local density of states, and therefore the rate of emission, by fabricating photonic structures around the spin defects. However, introducing

atomic interactions that lead to an increase in the non-radiative rate of the emitter is not desirable.

4. **Minimize added dephasing effects on the spin defect.**

   Similar to the point above, it is required that the embedding material atom species and intrinsic magnetic defects interact as little as possible with the spin. For instance if the majority of the atomic nuclei of the embedding material have spin values different to zero, this would create a very unstable magnetic environment for the solid state spin defect.

5. **Use of established fabrication procedures for building integrated circuits.**

   To address the issue of large-scale fabrication, it is important that the technology to deposit or grow the chosen material is readily available, repeatable and robust. Also, it is important that the deposition or growth method guarantees the survival of the integrated spin defects.

Looking at these requirements, there are three materials that would have the potential to meet them: titanium dioxide(TiO_2), aluminum nitride (AlN) and silicon nitride (Si_3N_4).

Titanium dioxide (TiO_2)

TiO_2, is a wide band-gap semiconductor with a band-gap energy dependent on its structure. TiO_2 can be found in crystalline and amorphous phases. Rutile and Anatase are the most common crystalline phases. Both have a tetragonal structure but they have different crystal habits. Rutile is the most thermodynamically stable phase, making it the most common of the TiO_2 crystalline polymorphs. It is transparent at visible and near infra-red (NIR) wavelengths and exhibits a high refractive index as well as a high non-linear refraction, making it attractive for non-linear optics.

For integrated optical devices, amorphous TiO_2 films have been used [46]. Usually these films are deposited using atomic layer deposition (ALD) or radio-frequency (RF) sputtering.

Very recently high Q resonators on amorphous titanium dioxide deposited on diamond membranes were demonstrated [47]. The combination of these two materials suggests integration with colour centres in diamond. In fact, integration with nanodiamonds was

suggested in [48] where large-Q nanobeam cavities are designed for a potential coupling with NV^- centres in nanodiamonds.

Aluminum nitride (AlN)

AlN has gathered attention in recent years as an option for infrared [49] and visible [50] integrated photonic circuits. AlN is usually deposited at low temperatures (300°C) either by reaction direct current (DC) magnetron sputtering [51] or radio frequency (RF) magnetron sputtering [52], both resulting in c-axis oriented AlN crystalline films. AlN has a wide transparency window that expands into the ultraviolet (UV), and a high second order nonlinear optical coefficient [53], making it attractive for UV spectroscopy and electro-optic applications.

Although integration with NV centres in diamond has been hinted before [54][55], it hasn't been shown experimentally. Interestingly, defects in AlN itself have shown promising applications as bright room-temperature quantum emitters [56].

Silicon Nitride (Si_3N_4)

Of the three materials mentioned, Si_3N_4 is the one that has become the most important, both in the CMOS industry and in the photonics industry. Si_3N_4 is used in standard CMOS processes as an insulator for individual transistors [57].

Although Si_3N_4 can be created in crystalline phases, amorphous Si_3N_4 is the most common phase used for electronics and photonics. Thin films are usually deposited using chemical vapour deposition (CVD) technology. The two most relevant types of CVD for photonics applications are low pressure CVD (LPCVD) and plasma enhanced CVD (PECVD). In LPCVD, the deposition occurs at a reduced pressure around 0.1 mbar and at a temperature of around 750 °C. In contrast, PECVD lowers the deposition environment requirement by the use of a plasma made of precursor radicals, allowing a deposition at temperatures below 300 °C, making it much more compatible with other CMOS processes.

Si_3N_4 photonics offers low optical loss from the visible to near infra red and it is commercially available through multiple commercial foundry platforms such as LioniX's TripleX and IMEC's BioPIX. TripleX technology has shown outstanding propagation losses as low as 0.001 dB/cm for a LPCVD strip waveguide [58].

The main impediment of using Si_3N_4 as the material platform to integrate with solid state spin defects is the presence of intrinsic photoluminescence (PL) under laser excitation. There are several records describing how this intrinsic emission has made the separation between signal and background in applications difficult, ranging from Raman spectroscopy [59] to actual spin state read-out of NV^- centres in diamond [60]. In fact, one of the motivations of Lu, Mouradian and collaborators [54] for the use of AlN for integration with atom-like systems is that under visible excitation AlN presents a much lower PL than (Si_3N_4).

Finding a solution to the intrinsic PL would make Si_3N_4 the most appealing material platform for the integration of atom-like systems like solid state spin defect. With this in mind, it was decided that the films would be deposited using PECVD with different parameters to try to control the amount of intrinsic PL of the resulting material films. Before attempting to control the PL, it was important to understand it's origin.

3.0.1 On the origin of Si_3N_4 photoluminescence

The origin of the Si_3N_4 PL seems to be far from trivial. There is a large amount of available literature on the emission of amorphous stoichiometric (Si_3N_4) and non-stoichiometric silicon nitride films. Non-stoichiometric films are denoted SiNx with x representing the ratio of N to Si atoms present in the film, hence, stoichiometric silicon nitride has $x = 4/3$. For the rest of this work silicon nitride films with $x < 4/3$ are referred to as Si-rich, whilst films with $x > 4/3$ are referred to as N-rich.

It is not the aim of this work to study the detailed atomic composition of the deposited films, however some insight is needed in order to understand the mechanisms that originate the intrinsic PL. SiNx films PL has been attributed mainly to 3 different mechanisms:

3.0.1.1 Si nano-crystals

During the deposition - depending on the conditions - clusters of Si atoms can be crystallised, forming nano-crystals of various sizes ranging from 1 to 10 nm. This has mainly been observed for Si-rich films [61][62]. These clusters show quantum confinement behaviour, which is the same phenomenon that quantum dots exhibit. This leads to the emission of photoluminescence, with the wavelength depending on the size of the cluster.

This phenomenon has been studied in-depth with the potential purpose of using it as an illumination technology.

Si nano-crystals can be detected by the use of high-resolution transmission electron microscopy (HRTEM), since the surrounding material has an amorphous structure.

3.0.1.2 Band Tail Photoluminescence

Amorphous materials have a high-density of localised states at the edges of the conduction and valance bands known as band tails (figure 3.1 a)). This band tail state can be explained by a phenomenon known as Mott-Anderson localisation, and leads to photoluminescence due to the recombination of electron-hole pairs separately trapped in band tail states [63]. This is the main mechanism of the amorphous Si PL [64] but it has also been shown to be present in other amorphous silicon compounds [65].

Boulitrop and Dunstan have shown that for amorphous Si, the relative energetic position of the optical band gap with respect to the excitation energy is proportional to the brightness of the PL [66]. The same observation was found in SiNx films by Kistner and co-authors [67]. This behaviour is characteristic of this mechanism.

3.0.1.3 Dangling bond defects

Defects and hydrogen (H) inclusion in amorphous silicon nitride films have been studied for a long time. It is not necessary to have crystalline structure in order to have defects. For an amorphous material, an alteration on the chemical order can be considered a defect. Si_3N_4 is made of a network of Si-N covalent bonds between tetrahedrally coordinated Si sites and three planarly coordinated N sites. For amorphous SiNx the structure is a random network of Si-N and Si-Si bonds. N-N bonds are unlikely to form because of their low energy, and this limits x to a maximum value $x = 4/3$.

Nevertheless, PECVD produces SiNx films that can contain up to 40% H. N-H bonds dominate over Si-H for N-rich films, allowing x to go up to $x = 2$ [68].

The most relevant defect in terms of PL in the visible region of the spectrum is the Si-dangling bond. Known as K-centre, this defect is an unpaired spin on a Si-atom backbonded to three N-atoms. It has an energy that lies within the optical band gap for all values of x (figure 3.1 a)), and a recombination for carriers from a K-centre results

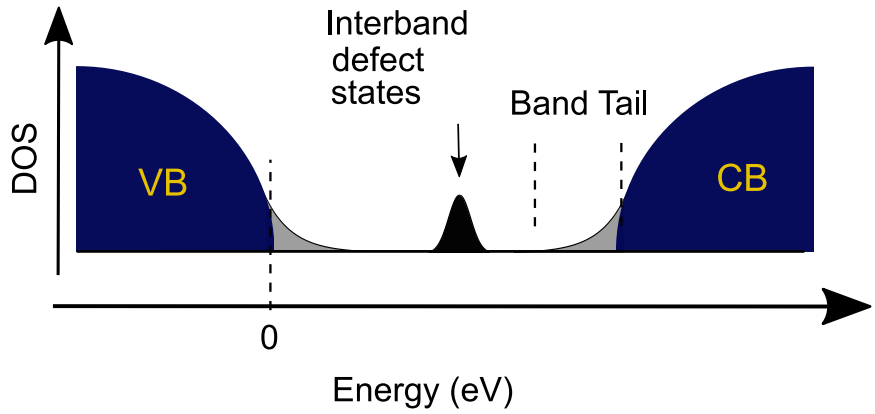

Figure 3.1: Density of states band diagram for an amorphous semiconductor. Between the valence band (VB) and the conductance band (CB) there are localized states distributed in an exponentially decaying profile that arise from the long-range potential fluctuations due to Mott localisation

in PL emission. These centres can exist in the neutral paramagnetic K^0 state and the charged diamagnetic K^+ and K^- states.

An important feature of these defects is that they can be photobleached. This means that under illumination (in the case of K-centres between 4 and 1.8 eV), the density of K^0 centres in N-rich films changes by switching to either of it's diamagnetic states [69]. This process leads to a notorious decline in the PL over time, reaching a lower threshold.

The three mechanisms presented are not mutually exclusive and their contribution to the PL emission depends heavily on the deposition conditions. As reported in many other studies [70][71][72], the spectral shape and relative brightness of silicon nitride films PL is linked to the stoichiometry of the material.

Unlike these studies, the goal here was to find the material composition that exhibited the least amount of PL. To do this, an experiment was conducted similar to those shown in [67] and [73], where films with different stoichiometries were deposited and their optical and PL properties analysed. The details of this experiment are shown in the next section.

3.1 Non-stoichiometric PECVD silicon nitride films

In PECVD, precursor gases are mixed in a vacuum chamber and then submitted to a radio frequency (RF) alternating electric field. In the first few seconds the alternating

field produces few ionic radicals that oscillate with the field, causing a chain reaction that creates more and more ions until a stable plasma is produced. When some of these radicals interact with the substrate, they bond to the surface, leading to the deposition of an amorphous film. The final composition of the film and the rate of deposition are determined by variables such as the alternating electric field power and frequency, the temperature of the substrate, and the concentration of the different precursor gases inside the chamber.

As a substrate, fused silica 10 x 10 cm squares (2mm thickness) were used, which were cleaned by submerging them in a beaker with acetone and putting them into an ultrasonic bath for two minutes. This process was then repeated with isopropyl alcohol (IPA) and de-ionised water (DIW), and finally with an N2 blow-dry before placing them inside the PECVD chamber.

As precursors to the films, silane (SiH_4) in a 5% argon (Ar) dilution (SiH_4) was used in combination with ammonia (NH3) and nitrogen (N_2) gas. For every deposition, the chamber pressure and substrate temperature were kept constant to 1 Tor and 300 C respectively. Whilst keeping a constant N_2 flow rate of 400 standard cubic centimeters per minute (sccm), the NH_3 and Ar + 5% SiH_4 flow rates were varied, keeping the sum constant to 400 sccm so the ammonia to silane ratio ($\mathbf{r}$ =NH_3:SiH_4) varied from 0.5 to 4. A summary of the deposited films is shown in table 3.1. Cycles of two different frequencies were used to produce the plasma. First, a 13.56 MHz (high-frequency) electric field was applied for 13 seconds, followed by a 340 kHz (low frequency) field that was applied for 7 seconds. This technique is known as dual frequency deposition and is used to balance internal mechanical stress of the films [74]. For all samples, the plasma striking cycle was repeated 82 times, leading to film thickness values between 280 and 400 nm. The changes in the gas ratio $\mathbf{r}$ lead to different deposition rates.

In order to have an accurate quantitative description of the N, Si, and H content of the films, measurements such as Fourier-transform infrared spectroscopy (FTIR) or X-ray photo-electron spectroscopy (XPS) are needed. However, having a detailed quantitative description of the atomic structure is beyond the scope of this project. The characterisation of the films was solely on their optical properties.

Sample	NH_3 (sccm)	Ar+SiH_4 (sccm)	SiH_4 (sccm)	**r**	**Sample**	NH_3 (sccm)	Ar+SiH_4 (sccm)	SiH_4 (sccm)	**r**
SN01	9.80	390.00	19.50	0.50	**SN09**	27.90	372.00	18.60	1.50
SN02	12.10	388.00	19.40	0.62	**SN10**	31.30	369.00	18.45	1.70
SN03	14.50	386.00	19.30	0.75	**SN11**	33.90	366.00	18.30	1.85
SN04	16.80	383.00	19.15	0.88	**SN12**	36.40	364.00	18.20	2.00
SN05	19.00	381.00	19.05	1.00	**SN13**	44.40	356.00	17.80	2.49
SN06	21.30	379.00	18.95	1.12	**SN14**	52.20	348.00	17.40	3.00
SN07	23.50	376.00	18.80	1.25	**SN15**	66.70	333.00	16.65	4.01
SN08	25.70	374.00	18.70	1.37	-	-	-	-	-

Table 3.1: Non-stoichiometric PECVD SiNx samples. The two precursor gases used in the chamber were ammonia NH_3 and a mixture of 95% argon Ar and 5% silane SiH_4. **r** is the ratio NH_3:SiH_4 flow rates.

3.1.1 Optical Properties

After film deposition, variable angle spectroscopic ellipsometry (VASE) was used along with transmission spectroscopy to find the thickness of the films as well as their optical constants.

Amorphous semiconductors like SiNx are well described by the Cody-Lorentz model in [75] where the imaginary part of the dielectric function ($\epsilon = \epsilon_1 + i\epsilon_2$) is piece-wise modeled as a single broad Lorentz oscillator for photon energies well above band gap, an exponential absorption profile for energies below band gap known as Urbach tail [76], and a quadratic function for energies near the band gap ($\epsilon_2 \propto (E - E_T)^2$) where E_T is the value of the optical band gap also known as "Tauc-gap" for Tauc's work on amorphous materials [77]. The real part of the dielectric function ϵ_1 is then calculated by Kramers-Kronig integration.

Optical constants of the films were extracted from the fitted dielectric function ϵ. Figure 3.2 a) shows the refractive index (n) of the films at a wavelength of 637 nm as a function of the ratio r =NH_3:SiH_4 during deposition. It shows that the films deposited with a higher flow of SiH_4 in the chamber present a higher refractive index. In other words, the films that contain more Si have a higher refractive index than those with an abundance of N. Similar results are shown in [73], where they explore the differences between films deposited using either high frequency plasma or low frequency plasma, compared to a mixed frequency approach, which was used here.

Figure 3.2 b) shows the extracted thickness of the films. As it was mentioned before, all films were deposited by repeating the 20 sec high-frequency/low-frequency cycle 82

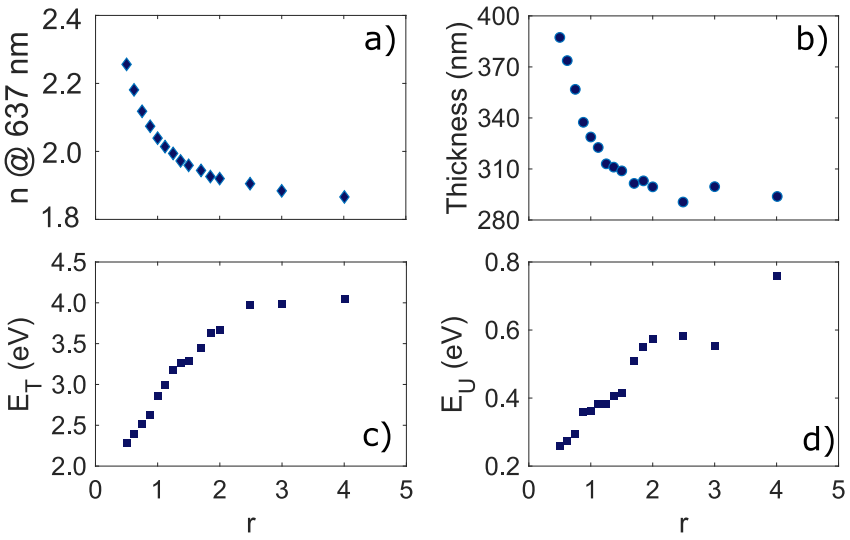

Figure 3.2: Optical Properties of silicon nitride films vs precursor gas ratio. a) Refractive index at 637 nm. b) Deposited film thickness after 82 cycles of mixed frequency PECVD deposition. c) Tauc gap energy extracted from the fitted Cody-Lorentz model of every film. d) Urbach energy extracted from the same mode.

times. This means that the deposition rates for the films goes from 4.2 nm/s for highest Si content to 5.6 nm/sec for the highest N content. A marked change in deposition rate is shown around $r = 1.25$.

Finally, figures 3.2 c) and d) show the values of extracted Tauc gap E_T and the Urbach energy E_u, respectively. The Urbach energy is related with the slope of the exponential band tails.

An alternative to FTIR and XPS for extracting the ratio of nitrogen to silicon atoms (x =N:Si) is the use of the following relationship derived from [78] that relates the relative content of Si and N atoms with the refractive index of the film:

$$x = \frac{4}{3}\frac{n_{\text{a-Si}} - n}{n - 2n_{\text{a-Si}_3\text{N}_4} + n_{\text{a-Si}}} \tag{3.1}$$

where n is the refractive index of the film, n_{a-Si} is the refractive index of amorphous silicon, and $n_{a-Si_3N_4}$ is the refractive index of amorphous stoichiometric silicon nitride, all at the same fixed wavelength. When the values of n at $637nm$ wavelength were used in equation 3.1 it was found that x monotonically increases from 1.24 to 1.84 for the samples prepared.

3.1.2 Photoluminescence

To measure the PL of the deposited films, a fluorescence confocal microscope, similar to the one described in chapter 2 was used. This setup used a 488 nm continuous-wave laser that was focused on the deposited films using a 0.9 NA microscope objective. PL radiated by the films was collected using the same microscope objective and separated from the excitation laser optical path with a dichroic mirror with a transmission edge at 550 nm. The PL was then collected by a single mode optical fibre and plugged into a spectrometer.

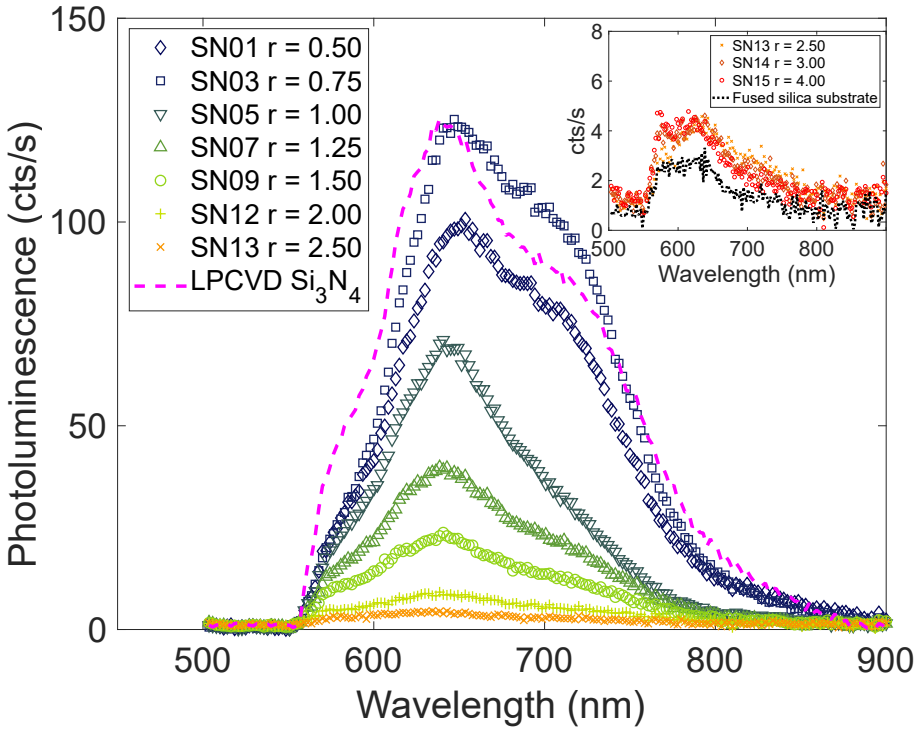

Figure 3.3: Photoluminescence of some of the SiNx films listed in table 3.1.The film was excited with a 488 nm CW laser focused on the sample with a power of 440 μW and thus a power density of $3.2x10^7 mW/cm^2$. The extinction of photoluminescence with the increase of nitrogen content in the films is noticeable. For reference, the PL of stoichiometric LPCVD is shown with a dashed magenta line. The inset shows a close up look of **r** values of 2.5 and above. The PL is almost as low as the fused silica substrate signal (indicated with a dotted line)

The obtained spectra is shown in figure 3.3 The units are given by the counts registered per second on the CCD sensor in the spectrometer. For all the samples, the PL emission is made up from two peaks with their relative brightness changing with **r**.

The central wavelength of these peaks blue-shifts very slightly with increasing nitrogen content in the material.

In addition to the PECVD deposited films, PL emission of a stoichiometric LPCVD silicon nitride film was measured under the same conditions as the other samples. The obtained spectrum is shown in figure 3.3 as a dashed black line for comparison.

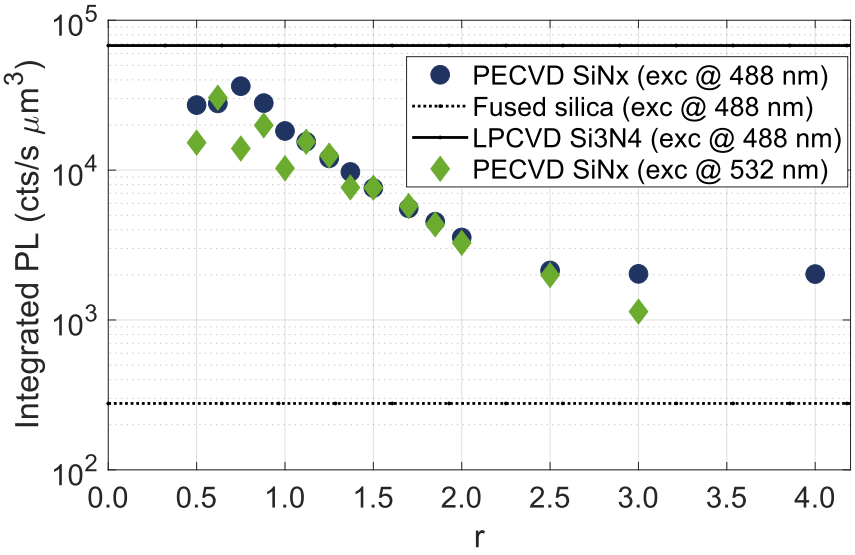

Figure 3.4: Relative PL emission obtained by integrating each spectrum over the emission range (500 nm to 900 nm) and normalising it by the excited volume for excitation wavelengths of 488 nm (blue circles) and 532 nm (green diamonds). It shows more than 30-fold reduction for $r > 2.5$ compared to LPCVD stoichiometric Si_3N_4 (solid black line). The collected background noise from the bare fused silica substrate was also integrated and added for reference (dashed line).

.

The relative PL brightness of each film can be quantified by integrating the spectra over the whole emission range (500 nm to 900 nm). and normalising it by the volume excited by the focused laser. This volume has been approximated by the cylinder defined by the area of the diffracted limited spot focusing on the sample (with diameter taken at 1/e of the maximum) and the film thickness that depends on the film r, as shown in figure 3.2 b). The integrated relative PL for the obtained spectra is shown in figure 3.4. Additionally, the relative PL obtained by exciting the material using a 532 nm laser is also presented. In both cases, the intensity reduces exponentially with increasing values of **r**. For an excitation of 488 nm, the PL reaches a minimum for values **r** >= 2.5

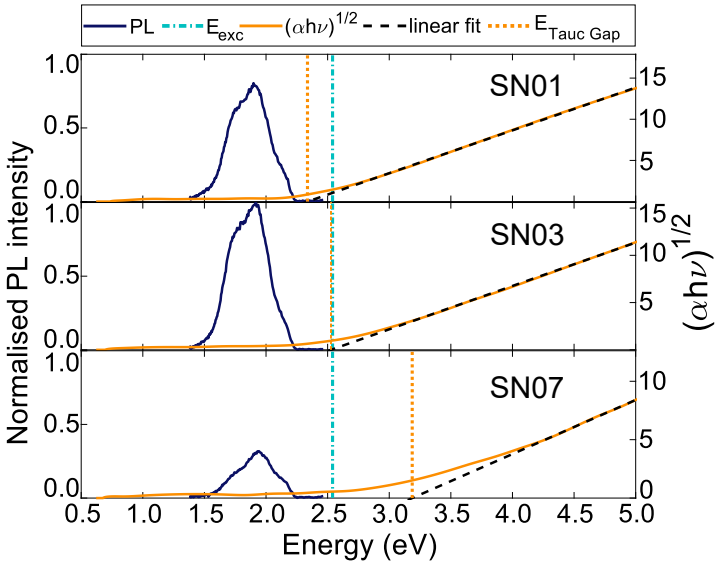

Figure 3.5: Normalised PL emission spectra for three different films. On the right axis a Tauc plot used to extract the value of the band-gap (also called Tauc-gap ($E_{Taucgap}$)) by plotting the square root of the absorption coefficient times the photon energy $(\alpha h\nu)^{1/2}$ and fitting a line to the linear section. It is shown how the emission is maximal when E_{exc} matches $E_{Taucgap}$

while a small decrease on PL is noticeable for values $\mathbf{r} < 0.75$ compared to the maximum obtained at $\mathbf{r} = 0.75$.

The behaviour observed has a resemblance to the band tail PL studied by Kistner and co-authors in [67]. The Tauc gap (E_g) of the sample with the brightest emission has a very similar value to the excitation laser energy (E_{exc}). Provided the monotonic behaviour of E_g with $\mathbf{r}$ (shown in figure 3.2c)), films deposited with values $\mathbf{r} < 0.75$ were excited above band gap while the rest of the films with $\mathbf{r} > 0.75$ were excited below band gap. This is better illustrated in figure 3.5 where the PL emission of three representative cases is plotted as a function of photon energy and normalised to the maximum value of the brightest films.

Superimposed, the so called "Tauc-plots" are displayed for the same three cases. A Tauc plot is used to determine the optical band gap or Tauc gap of a material. This is done by plotting the quantity $\sqrt{\alpha h\nu}$, to where α is the optical absorption and $h\nu$ the emission energy. The value of the Tauc gap can be found by following a linear regression and finding the intersection with the x-axis shown. Finally the excitation laser energy is highlighted to show that for excitation above and below the Tauc gap value the emission

is less bright than the case where excitation energy matches the Tauc gap.

Although the change in emission intensity follows a behaviour of the overall brightness of the PL is very similar to the one described by Kistner and co-authors [67] for N-rich SiNx films, the PL central wavelength of the samples here does not shift as much as a function of $\mathbf{r}$, suggesting there is another mechanism involved in the PL observed. Analysing films with a higher Si content than SN01 would provide a better evidence of the PL levels for excitation above band gap. Unfortunately, depositing films with such characteristics was not possible with the PECVD system available. Alternatively, measuring the behaviour of the PL for lower excitation wavelengths (higher energy) could show if the brightness is in fact, related with the relative difference between E_{exc} and E_g

In addition to the brightness reduction with the increasing content of nitrogen, the PL of the deposited films manifest some photo-bleaching effect. During the measurements, it was noticeable that the total amount of emitted light decreased with time at a rate yet to be characterised. Each spectra measurement was taken over the course of one hour. During this time the excitation laser photo-bleaches the material, therefore the spectra shown in figure 3.3 represents the emission of the material once it has been bleached and does not correspond to the emission that quickly decays under illumination. It is worth noting that through the examination of the PL of these films no spatial variation was observed. In other words, no evidence of localised emission was observed. However, other groups have reported the observation of individual defects in N-rich silicon nitride [79].

To prove that the PL observed is in fact related with defects like the K-centre, the samples could be annealed in a N_2 [H_2] gas ambient to reduce [increase] the H content of the films. This would lead to creation [passivation] of dangling bonds and therefore an increment [reduction] in the PL brightness. However, this is beyond the scope of this project.

Finally, it is worth mentioning that although it wasn't possible to take HRTEM images of the deposited films, and therefore the presence of Si nano-crystals in the samples were ignored, it is not believed that the PL comes from quantum confinement effects. The films are mainly N-rich making Si nano-crystals formation less likely. Also, if PL was coming from quantum confinement that would mean that the size of the nano-crystals remain almost constant, since the PL doesn't shift much with $\mathbf{r}$. If the

relationship that links PL frequency central peak and nano-crystal diametre in [62] is applied to these results, it would mean that Si nano-crystals would only change from 4 nm for SN01 to 3.7 nm for SN15.

In summary, fluorescence and ellipsometry measurements are not enough to completely describe the underlying mechanism that produces the films PL. Without any other measurements is not possible to determine if the reduction on the PL is due to the change in the band-gap, the change in the amount of dangling bonds or a combination of both. A detailed investigation would require doing FTIR and XPS measurements or any other measurement that provides information about the compostion of the films. In any case, the complete physical description of the origin of the PL in these specific films is not the main goal of this work. The main objective of finding a film composition with low intrinsic PL has been achieved. It has been shown that by the use of N-rich SiNx films **the intrinsic PL emission can be reduced by a factor** > 30. For the rest of this document, whenever SiNx is referred to, it will be referring to N-rich films deposited under the same conditions as sample SN14 (**r** = 3.0). From equation 3.1 this means $SiN_{1.82}$.

The next question that required an answer was whether this reduction was enough to be able to detect single photon emission of spin defects in nanoparticles encapsulated in this material.

3.2 NV^- centres in nanodiamonds encapsulated in N-rich SiNx

Once it was shown that SiNx PL can reduce by more than an order of magnitude by increasing its nitrogen content, it was helpful to show that the PL of the N-rich SiNx was low enough to be used as an encapsulating matrix for solid-state spin systems in the single photon regime. As explained in chapter 2, through this research, NV^- centres in nanoparticles of diamond (or nanodiamonds (NDs)) were used as the solid state spin defect to be integrated. Nanodiamonds were encapsulated with N-rich SiNx and collected light coming from NV^- centres within them. To be able to measure the effects of N-rich SiNx encapsulation both optical and electron spin properties of the same NV^- centres were characterised before and after encapsulation.

3.2.1 Sample preparation

Preparation began with the same fused silica substrate as in the previous section, and solvent cleaned in the same way. To be able to identify NV^- centres before and after capping, fiduciary markers were needed. A 200 nm thick film polymethyl methacrylate (PMMA) was spun-coated on the fused silica and baked for 120 seconds at 180 C followed by a few nanometers thick coating of a conductive polymer (Electra92 from All Resist). Using electron beam lithography (EBL) a grid of serif crosses along with alphanumeric coordinates were patterned onto the PMMA. The conductive polymer prevented charge accumulation on the dielectric substrate. After patterning, the conductive polymer was rinsed using DI water and the exposed pattern on PMMA was developed in a 1:3 solution of methyl isobutyl ketone (MIBK) in IPA for 1 min .

Using thermal evaporation, a thin film of Cr/Au was deposited (15 nm Cr under 85 nm of Au). Cr promotes a better adhesion to the substrate allowing the sample to be submitted to another acetone ultrasonic bath for lifting the mask off. A microscope image of the metallic markers is shown in the inset of figure 3.6.

A drop of a nanodiamonds colloidal suspension was spin-coated on the sample with the metallic markers and taken to the lab for optical characterisation. After the first measurements, a 100 nm thick film of N-rich SiNx (SN14 recipe) was deposited, capping the nanodiamonds and markers. A more extensive description of the nanodiamonds used throughout this work is given in chapter 4.

3.2.2 Confocal scans

Using the lab-built confocal microscope described in chapter 2, a raster scan of the sample was taken. The image obtained is shown in figure 3.6. The scanning range of the stage driven by piezoelecric actuators is only 20 μm, however added stepper motors in each axis allows for large scans by stitching 20 x 20 μm scans. The bright features marked with cyan squares are the auxiliary metallic serif crosses. From among all the other bright spots, four NV^- centres labeled A to D were identified. Intensity auto-correlation measurements were done to verify the single emitter nature of the four identified single NV^- centres.

Figure 3.7 shows a confocal scan of the same sample after silicon nitride deposition. It shows all four NV^- centres survived encapsulation and nanodiamonds did not move

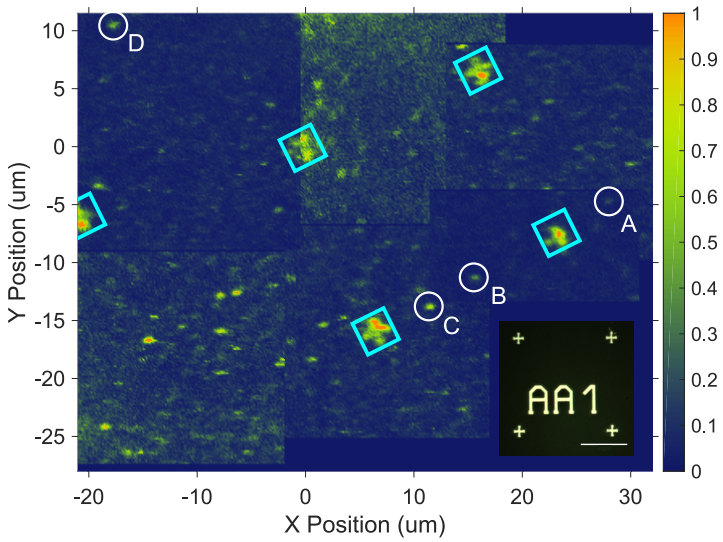

Figure 3.6: Confocal scan of nanodiamonds on fused silica substrate. Images are normalised with 10% saturation. Metallic crosses on the sample are identified with a cyan square. NV^- centres studied in this work are labeled A-D. Inset: Optical microscope image of metallic markers on the sample prior to the nanodiamond deposition. The scale bar is 10 μm.

significantly. The ability to go back to the same emitters after capping is enabled by the use of the metallic crosses (marked again with cyan squares), and coordinate labels (not shown on the scan).

To increase the amount of collected signal from the capped NV^- centres, the single mode collection fibre (SM600) was swapped with an SMF-28 fibre with a mode field diameter (MFD) of 9.2 μm, deteriorating the spatial resolution of the scans but increasing the amount of detected light.

The increase of the background noise compared to the scan before capping is due to the remaining N-rich SiNx PL. It is important to notice that scans are taken by displacing the sample with respect to the optical axis, hence the sample is illuminated "one pixel at a time". By doing this, the signal obtained for the confocal image comes from the emission and scattering produced within the first milliseconds after excitation. Once the SiNx has been exposed to the excitation laser, it photo-bleaches as discussed in the previous section, meaning that areas that have not been exposed before will show a brighter background than those that have been scanned before.

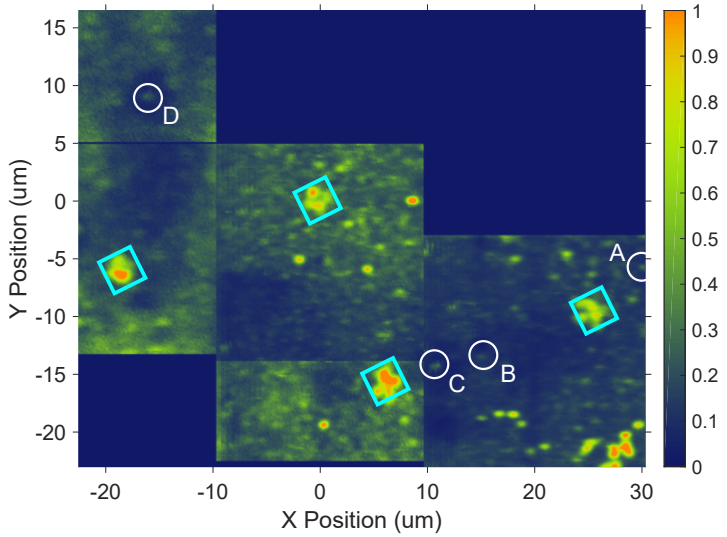

Figure 3.7: Confocal scan of nanodiamonds encapsulated in N-rich SiNx. Images are normalised with 10% saturation. Metallic crosses on the sample are identified with a cyan square. Studied NV^- centres A-D are identified and labeled.

3.2.3 Single photon emission from buried NV^- centres

As discussed in chapter 2, intensity auto-correlation $g^{(2)}$ measurements are a rigorous way to identify single photon emission. The way the 4 NV^- centres were chosen to analyse from the sample was by performing Hanbury-Brown-Twiss measurements on several bright spots observed in the confocal scan and picking the ones that showed single-photon behaviour. The NV^- centre emission is collected into a fibre splitter dividing the signal equally (50:50) between two single photon avalanche diode (SPAD) detectors. The top row of figure 3.8 shows the auto-correlation histogram of the detection events normalized by making $g^{(2)}(\infty) = 1$ and fitted with the three-level emitter model described in equation 2.4 of chapter 2. For the four chosen NV^- centres a $g^{(2)}(\tau = 0) < 0.5$ is shown, indicating emission from single quantum emitters.The error associated with the obtained values is obtained from the confidence bounds of the model fitting. It is important to mention that these measurements haven't been corrected for background optical noise or electronic noise (dark counts) in order to get a good comparison with the after-encapsulation case.

After capping with N-rich SiNx the story is a bit different. The auto-correlation measurements were repeated on the same four NV^- centres (shown in the bottom row of figure 3.8) after encapsulation. There are two factor that can be contributing to the

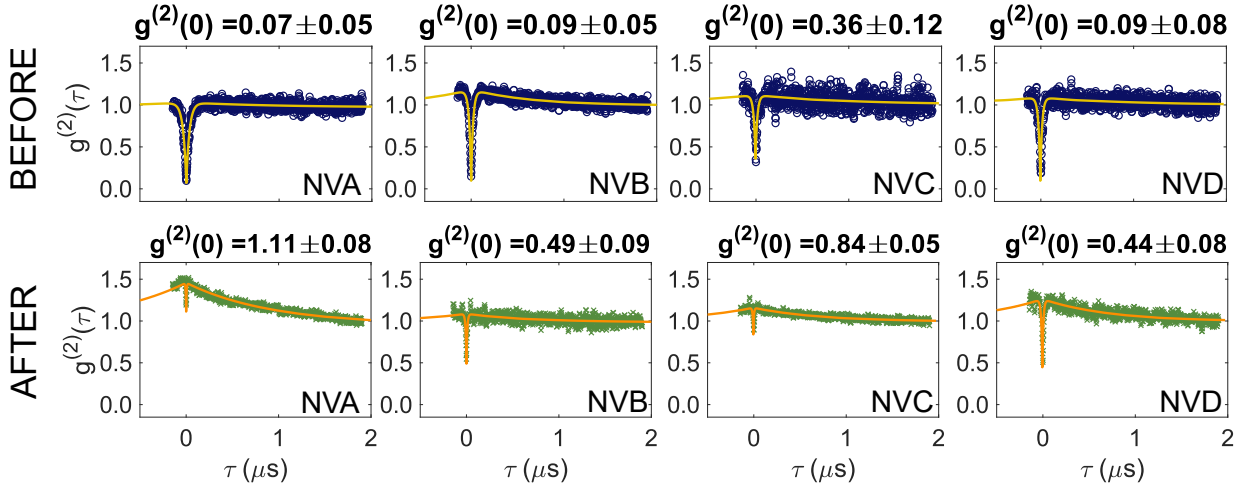

Figure 3.8: Second order auto-correlation measurements of NV^- centres A-D before (top row) and after capping (bottom row). Measurement in the top row show $g^{(2)}(\tau = 0) < 0.5$ characteristic of single photon emission from individual NV^- centres

increase on the $g^{(2)}(\tau = 0)$ value. First, the remaining PL of the nitrogen-rich silicon nitride films still has a small effect on the single photon statistics from the collected signal. Second, once the ND have been capped, the NV^- centre fluorescence escaping the material is less compared to the uncapped case since some of this light is coupled into the slab mode of the SiNx film. In other words, the light extraction efficiency decreases once the ND are capped leading to a reduced signal-to-noise (SNR) ratio. In order to obtain the minimum amount of background PL, it was important to photo-bleach the material around the NV^- centres by exposing the film at high powers before taking any measurements. By mistake, the HBT measurement for NVA was taken with high power, exceeding several times the saturation power and giving rise to a fitted value of $g^{(2)}(\tau = 0) > 1.0$. For the other three encapsulated NV^- centres, anti-bunching behaviour is conserved ($g^{(2)}(\tau = 0) < 1.0$) and in case of NV^- centres B and D $g^{(2)}(\tau = 0)$ stays close to 0.5.

One important remark to make is that $g^{(2)}$ measurements ran for several minutes to collect enough statistics of many detection events. This represented a challenge since the three piezo-actuators that the sample was mounted onto had a considerable shift over those time scales. In order to compensate for this, while recording the $g^{(2)}$ data a stabilisation routine was run in parallel that consisted of doing a few μm scans in each of the spatial axes (X,Y,Z) in order to find the centre of the NV^- emission and re-centre the sample to maximize the counts. Performing these axial scans in the middle of the

auto-correlation measurements added noise to the data.

It is clear that more work towards suppressing the background optical noise is needed, however it has been shown as a proof-of-concept that nitrogen-rich silicon nitride has the potential to meet the second of the requirements listed at the beginning of this chapter.

In addition to measuring single-photon emission, the fluorescence lifetime of an NV^- centre was measured before and after encapsulation. By replacing the continuous wave excitation laser with a pulsed excitation laser with repetition rate of 10 MHz, it is possible to measure the time it takes for NV^- centre excited state to decay into the ground state. Figure 3.9 a) shows the fluorescence lifetime of NV^- centre D before and after encapsulation. A bi-exponential model was fitted to separate the fast contributions, like background noise from Rayleigh scattering of the pump laser from the slower NV^- centre emission. After capping, the fluorescence lifetime is slightly reduced. This can be explained by the presence of a new dielectric interface (SiNx - air) and the the fact the emitter is now surrounded by a higher refractive index, increasing the spontaneous emission rate compared to the emission into air. This phenomenon is explained in more detail in section 4.2.2 where the change in emission rate under different dielectric boundaries is simulated.

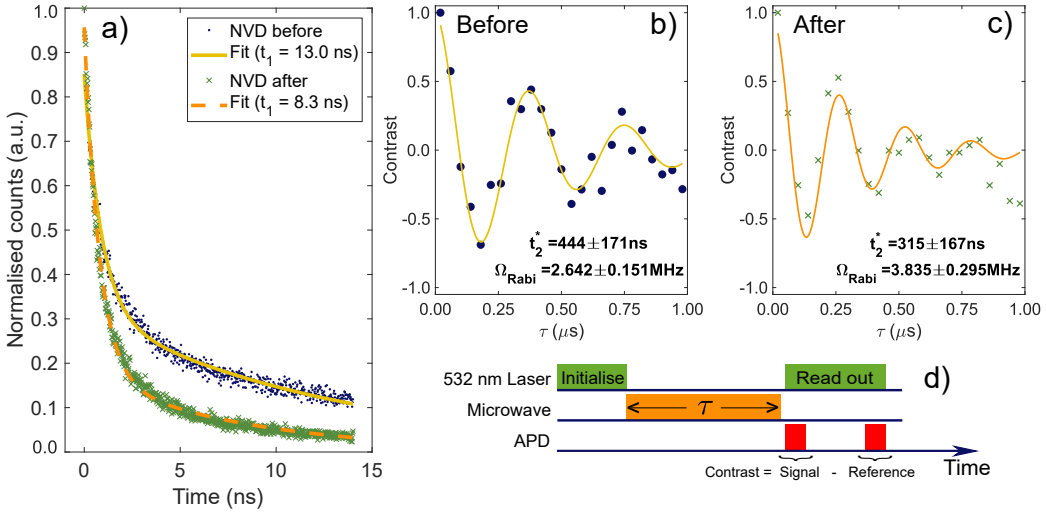

Figure 3.9: a) Fluorescence life time of NV^- centre D before and after encapsulation. A reduction in lifetime is observed due to the higher refractive index environment. Rabi nutation measurements for NVD before b) and after c) encapsulation. The fitted Rabi decay indicates that the NV^- centre electron spin maintains coherence in the N-rich SiNx environment. d) Rabi nutation measurements pulse sequence.

3.2.4 Coherence decay of electron spin state

To prove that the encapsulation doesn't have a major impact on the coherence time of the NV^- centre electron spin state, Rabi nutation measurements were performed with the pulse sequence shown in figure 3.9 d). First, a laser pulse is used to polarise the electron spin in its $m_s = 0$ state. Then, a microwave pulse with frequency tuned to the spin transition (in this case from $m_s = 0$ to $m_s = -1$) and duration τ is applied to resonantly drive the spin state. The degeneracy of the states $m_s = -1$ and $m_s = +1$ is broken with the application of an external magnetic field. The spin state can be read-out by monitoring the fluorescence produced by the excitation of a 3 μs laser pulse and recording the contrast (Δ) between the number of emitted photons during the first 300 ns of the read-out excitation pulse with the last 300 ns of it. By fitting a decaying sinusoidal function of the form $\Delta(\tau) = A\exp\left\{-\frac{\tau}{t_2^*}\right\}\sin\left(\Omega_{Rabi}\tau - \phi\right) + d$ the coherence time t_2^* and Rabi frequency Ω_{Rabi} can be extracted. A value of $t_2^* = 444 \pm 171$ ns is extracted from fitted data. While, the measured t_2^* for the NV^- centres in these NDs is too short for realising any entanglement distribution protocol, this value is by no means the limit of the coherence times that can be achievable with NDs. There is plenty of room for improvement on the quality of the NDs used as values of 400 μs for t_2 have been reported [11]. However, the results presented here are a proof-of-concept to evaluate the detriment the electron spin coherence time suffers after encapsulation.

From figure 3.9 c) a small change in the Rabi frequency (Ω_{Rabi}) is observed. The change in Ω_{Rabi} is most likely to be caused by the change in the position of the NVD with respect to the loop antenna after being removed from the microscope for the deposition of the SiNx film and put back on the PCB. A different position with respect to the antenna means the NV^- centre was receiving a different power from the MW field and hence changing the frequency. More important, no significant change (within error bars) in the coherence time of the electron spin in NVD occurs after capping. While this small change on the is a good indicative that encapsulation is not affecting dramatically the magnetic enviroment that the NV^- centre sees, to get a better insight into the physical phenomena happening on the boundary between the nanodiamond and the SiNx and the effect on the NV^- centres, it is proposed that the studies presented here are extended to many more NV^- centres. With that goal in mind, better ways of depositing the nanodiamonds were explored. The approach used is described in the next chapter.

CHAPTER 4

SPATIAL CONTROL OF NV CENTRES FOR SCALABLE QUANTUM PHOTONICS

The nanodiamond deposition method presented in this chapter was a joint effort between myself and another PhD student, Cecile Skoryna Kline. The rest of the work presented here is my own.

In the experiments shown in chapter 3, the specific position on the nanodiamonds (NDs) on the sample after deposition was not particularly relevant to the results. However, the random spatial distribution obtained by spin-coating certainly had an impact on the time it took to find and characterise the NV^- centres. This therefore limited the amount of data collected. To get a better idea of the effect that SiNx encapsulation has on the properties of NV^- centres, the analysis of tens of defects would be required.

In general, collecting data from multiple stochastically distributed quantum emitters using confocal microscopy requires large area scans and a thorough investigation of every single bright spot, consuming a lot of time. For instance, for the setup used throughout this project, scanning with diffraction limited resolution a $20\mu mx20\mu m$ area with a pixel integration time of 8 ms takes around 5 minutes. This means that it would take at least 200 hours to scan 1 mm^2 simply to collect the data, let alone the analysis time required for such large data sets. The chosen pixel integration time was found to be the minimum

required to obtain a signal-to-noise ratio (SNR) well above 1 given the detectors used.

In addition to the scanning time, identifying the individual emitters amongst all the bright features shown in a confocal scan is extremely time consuming. As it was explained in chapter 2, the golden standard for identifying single emitters is to look at the fluorescence intensity auto-correlation. The time it takes to obtain a clear single photon emitter signature from auto-correlation measurements can vary from a few minutes to hours depending on the emitters' brightness and SNR. In the context of this work, brightness is defined as the amount of photons collected and detected per unit time. Due to the time required for these kind of measurements, having data from tens of single emitters can take hundreds of hours. While this might be doable as an academic experiment, it is difficult to imagine a process with these timescales being part of the construction of devices for commercial applications.

From the photonics point of view, the picture is much worse. The coupling between a quantum emitter and a photonic structure designed to modify its emission is crucially dependent on the position of the emitters. This means that the deposition method taken on the experiments shown in chapter 3 where the nanodiamonds (NDs) were deposited in random positions is a non-optimal approach.

Random dispersion of nanoparticles does not lend itself to scalable production. Fabricating structures around randomly scattered quantum emitters on a plain substrate requires the localisation of the emitters, which is very time consuming. Not only that, fabrication around randomly positioned emitters implies that every new spatial distribution emitter would require a different layout of the photonic devices and a unique photonic integrated circuit design for each iteration, making it unrealistic from a scaling perspective.

If the order is exchanged and the emitters are created or added randomly on a chip with pre-fabricated devices, the story is no different. Relying on the probabilistic landing of nanoparticles on pre-fabricated photonic devices is unfeasible, since the likelihood of ending with one particle containing a defect on N devices decreases exponentially with N. This probabilistic nature essentially would limit the scale of the system in a similar magnitude as the limitation of state-of-the-art quantum photonics. The only difference is that the nanoparticle approach would be swapping the probabilistic nature to the fabrication of the devices, rather than the operation of them. This defeats the original purpose of this project. Hence, some degree of control is needed on the position

of quantum emitters; not for the fabrication of devices but also for the fast and massive characterisation of spin defects.

It is important to point out that the challenge of working with randomly distributed emitters is not exclusive to the approach explored in this project. For example, naturally occurring solid-state spin defects like colour centres in diamond are randomly distributed in the crystalline matrix of the host material, while self-assembled indium-gallium arsenide quantum dots (InGaAs QDs) are formed stochastically on the substrate [80] in the absence of any seeding.

It is clear that in order to scale up to applications that rely on more than one emitter on chip, control over the emitters positions is required. There have been many attempts to achieve this involving both top-down and bottom-up approaches. For example, for defects involving impurities in a material, the most common top-down approach for achieving spatial control over the defects is ion-implantation. For instance, ion implantation has been the most utilised technique for deterministic positioning of colour centre in diamond. Creation of NV, [81], SiV [82], GeV[83], and SnV centres[84] on bulk diamond have been demonstrated using ion implantation achieving position control with varying accuracies. Alternatively, laser writing of NV centres [85] and spin defects in hexagonal boron nitride (hBN) monolayers [86] has been demonstrated, however the accuracy of position is limited, in the best of cases, by diffraction limit.

Since the approach presented here tries to move away from using the defect-host materials to create photonic systems, spatial control over the spin defects position would rely on the deterministic placement of the nanoparticles. The advantages and disadvantages of using NDs in terms of the effects this has on the NV^- centres were discussed in chapter 2. In terms of positioning, using nanoparticles can be more cost-effective, and in some cases result on a better spatial control than ion-implantation. However, the main disadvantage in terms of positioning is the probabilistic occurrence of single spin-defects in single nanoparticles.

In this chapter, spatial control on the deposition of NDs is demonstrated. Section one shows the method used and discusses a strategy for maximising the likelihood of placing exactly one NV^- centre is discussed. Section 2 explores the effect that the orientation of NV^- centres with respect to the substrate plane has on the measured brightness and emission rate leading to the proposition of an alternative technique to identify the absence or existence of single NV^- centres avoiding the use of autocorrelation

measurements.

4.1 Deterministic positioning of NDs

There are various approaches in the literature to attain spatial control over deposited nanoparticles. In particular for NDs, there have been many demonstrations of position control. The techniques used can be split into two broad categories:

- *Pick-and-place methods* aim to control the position of individual nanodiamonds one at a time. By the use of a tapered optical fibre [87], an atomic force microscope (AFM) tip [88] or a sharp tungsten tip [89] individual NDs can be pushed to the desired positions on a chip. A good example of this technique can be seen in [41] by Wolters and colleagues. They showed the positioning of a single ND with a single NV^- centre at the centre of a photonic crystal cavity. While these techniques have been proven to be successful in showing enhancement of the emission rate of NV^- centres, it is difficult to imagine these type of techniques could scale up to many devices because of the time required to place NDs individually. Another interesting demonstration of individual handling of NDs can be seen in [90] where optical forces are used to move and trap NDs to place them in plasmonic nanoantennas.

- *Lithographic methods* can be used to generate large scale patterns of deposited nanodiamonds in one step. The lithographic deposition, also often called directed self-assembly, is achieved by the use of a template made with either photo-lithography or electron beam lithography that serves as a stencil for the NDs. A layer of NDs in solution is applied to the mask allowing some of the NDs to go through the apertures in the template and deposit on the substrate. After removing the mask, patterns formed by the nanodiamonds are revealed. The resulting patterns have been used as seeds for diamond CVD growth [91] or simply with the purpose of characterising the fluorescent properties of the NDs [92]. Another option is to use electron beam induced deposition (EBID) to create a carbon seed where NDs bind strongly upon contact [93].

Whilst most of the successful demonstrations of deterministic positioning of NV^- centres have been done using pick-and-place techniques, the goal of this project is to keep the scalability of each step a key priority. The lithographic methods are much more

compatible with the vision and motivation of this project, hence, the subsequent sections detail the steps taken for a lithographic deposition.

4.1.1 Nanodiamond colloidal suspension

The NDs used in this project (supplied by NaBond Technologies Co.) were milled from synthetic high pressure high temperature (HPHT) bulk diamond with a low concentration of nitrogen (N) impurities ($N < 50ppm$). This concentration of impurities lies within the definitions of type Ib and IIa diamond as explained by Knowles and co-workers [37]. They have shown that in this intermediate regime of purity, the concentration of N atoms is low enough for the electron spin state of NV^- centres to have coherence times $> 60\mu s$, but still high enough that probability of having an NV^- centre in a single ND (γ_{ND}) is > 2%.

Prior to deposition, the first step is to have the NDs suspended in a liquid medium to be able to deposit them on the samples. A nanodiamond colloidal suspension was created using ethanol (C_2H_5OH) as the medium of suspension. The suspension was created as follows: A combination of 20 mg of ND powder with 100 ml of ethanol was mixed together. The mixture was put in an ultrasonic bath for 5 minutes to help the dispersion and break macroscopic ($> 100\mu m$) agglomerates. Next, syringe filters were used to filter out large particles ($> 2\mu m$) and agglomerates. Three suspensions (S00, S01 and S02) were made by filtering the original suspension with a 1.2 μm pore syringe filter. S01 and S02 were additionally filtered using a 0.45 μm pore filter and finally S02 was filtered with a 0.2 μm pore filter. It is worth pointing out that suspension S01 was the suspension used on the experiments shown in chapter 3.

The distribution of particle sizes in the suspensions was characterised using dynamic light scattering (DLS). Dynamic light scattering (DLS) is technique used to determine the size of particles suspended in a liquid. In this technique, a laser is focused on a small recipient containing the suspension. The back-scattered light from the suspension is measured with a detector placed a few degrees off of the optical axis. The particles suspended in the liquid medium exhibit Brownian motion and pass intermittently through the beams waist increasing the scattering every time a particle passes through the focal point. The average speed and displacement the particles experience is proportional to their size. This means that the larger the particle, the slower it moves. The optical scattered (back-scattering) signal produced by particles flowing through the focal

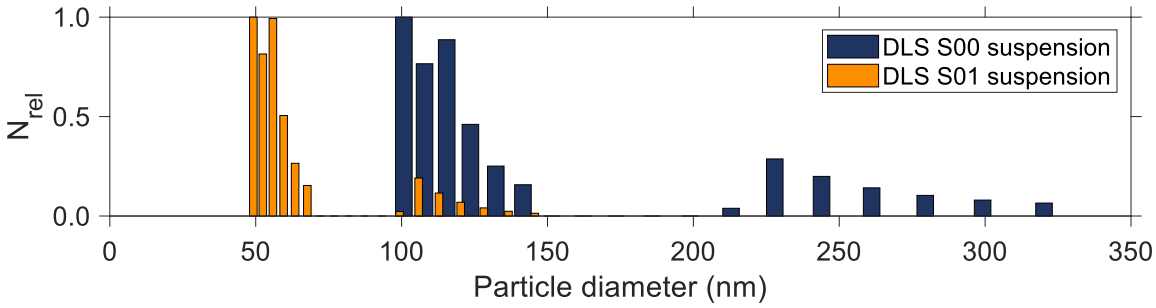

Figure 4.1: Size distribution of particles in colloidal suspensions S00 and S01 measured by dynamic light scattering (DLS). The relative number of particles sorted by size is shown for suspensions S00 in blue and S01 in orange showing the effect of the filtering suspension S01 went through.

point over time is recorded. By extracting the correlation of the recorded optical signal with a delayed copy of itself (auto-correlation) the diffusion speed can be obtained, and consequently the size of the particles.

Figure 4.1 shows the normalised distribution of ND sizes for suspensions S00 and S01 obtained by DLS. Unfortunately, for suspension S02 the concentration of particles became too low to be detected by this technique. The measurements show two distinctive size groups for each of the suspensions. While this could be due to the formation of pairs of particles and threes of particles, it is more likely that the smaller size groups is an artifact of the fitting of the autocorrelation data. For suspension S00 the dominant population of particles have an average size of 113 nm while the filtered suspension S01 shows particles with an average size of 55 nm.

The ND size is an important factor for the integration with photonic structures. From the photonics point of view, the smaller the ND containing an NV^- centre, the smaller the perturbation to the refractive index, and therefore the better the performance of the photonic devices. However, extremely small NDs have two major problems: First, the likelihood of having an NV^- centre in the ND decreases with the volume. Second, bringing the surface too close to the NV^- centre can have a negative impact on the optical dephasing of the electronic transition, on the electron spin coherence time, and even on the radiative efficiency by charge traps in the surface producing “blinking” [94]. This means that a trade-off is required with an optimal ND mean size dependent on the application.

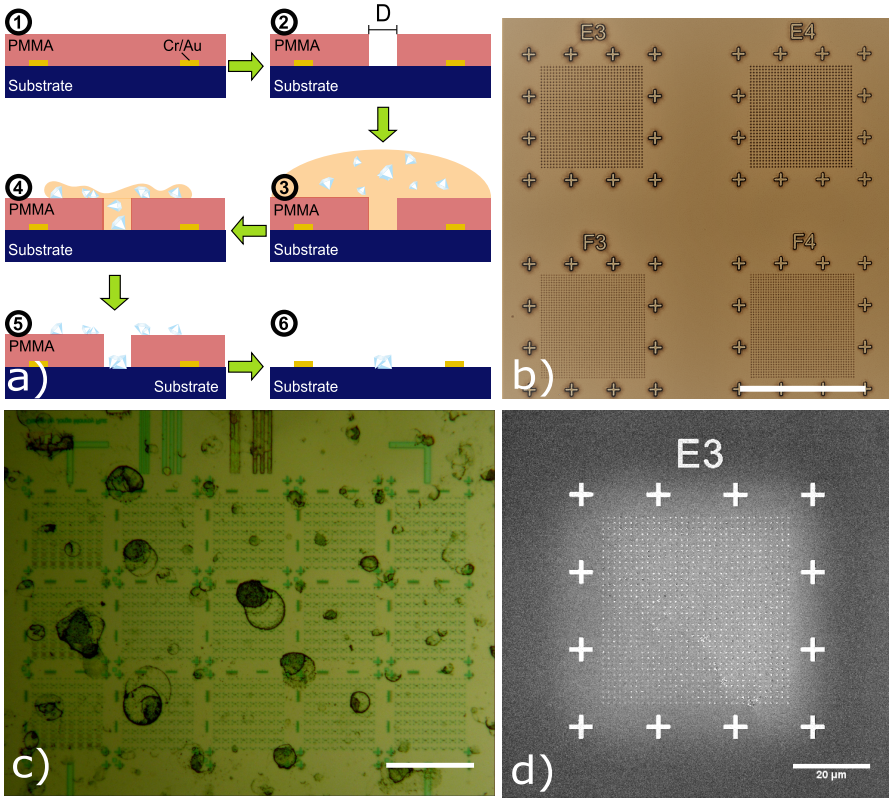

Figure 4.2: Lithographic deposition of NDs. a) Schematic illustration of the Lithographic deposition process. b) Optical microscope image of the polymethyl methacrylate (PMMA) template with patterned apertures (step 2). The metallic markers can be seen under the PMMA layer (scale bar is 60μm). c) Optical microscope image of the scattered NDs before lift-off (step 5). The formation of micro-droplets of suspension before complete evaporation leads to *coffee ring* effect stains on the PMMA [95] (scale bar is 500 μm). d) Scanning electron microscopy image of an array of NDs on SiO_2 for apertures with D = 400 nm

4.1.2 Lithographic deposition of NDs

The deposition method chosen for this project was followed from the work by Heffernan and co-authors in [92]. The steps are listed below:

1. Two 10 x 10 mm pieces of SiO_2 (1μm) on Si wafer were cleaned with the solvent cleaning procedure detailed in chapter 3. Auxiliary metallic alignment markers and labels were patterned onto the samples by the use of electron beam lithography (EBL) and thermal evaporation. Square areas of 60 x 60 μm were labeled with letters A to H and framed with crosses. After lift-off, the samples were solvent

cleaned again and subjected to an oxygen plasma cleaning process for 2 minutes. One of the pieces was coated with a 300 nm thick layer of PECVD N-rich SiNx to determine whether there was a difference between the NDs adhesion to the SiNx and SiO_2 surfaces. Once cleaned, a thin layer of polymethyl methacrylate (PMMA) with thickness t = 200 nm was deposited by spin-coating on the samples to be used as EBL resist.

2. After baking the PMMA for 60 seconds at 150 °C on a hot plate, arrays of apertures with different diameters **D** were patterned using EBL. The diameter values used are summarised in table 4.1. A dose calibration (detailed in the next section) was carried out before the patterning of the sample to ensure that the diameters of the apertures were accurate. An optical image of the obtained template can be observed in figure 4.2 b).

3. After developing the mask, 10 μl of the colloidal suspension S01 were dropped onto the samples

4. The samples were left at room temperature for the ethanol to evaporate for 30 minutes.

5. After 30 min the ethanol was mostly evaporated leaving regions of the samples covered with NDs. The formation of micro-droplets of suspension before complete evaporation leads to “coffee ring” effect stains on the PMMA (figure 4.2 c)

6. After this, the samples were carefully dipped in acetone for 3 minutes to remove PMMA mask. The removal of the PMMA mask was the most critical step. The samples were dipped vertically and as slow as possible to avoid agitation that lead to re-deposition of the particles on the substrate. An example of the final result is shown in figure 4.2 d) where the array of ND can be seen.

4.1.3 PMMA hole calibration for ND deposition

For the deposition of NDs, the diameter of the apertures created were calibrated patterning circles with different diameters and different doses determined by the product of the base dose and a **dose factor**. To measure the diameter of the aperture created after development, a bi-layer of Cr/Au was deposited. After lift-off the deposited metallic disks created by the apertures were analysed by SEM. Figure 4.3 a) to c) shows SEM images of the metallic disks created with the same design diameter but with different dose factors.

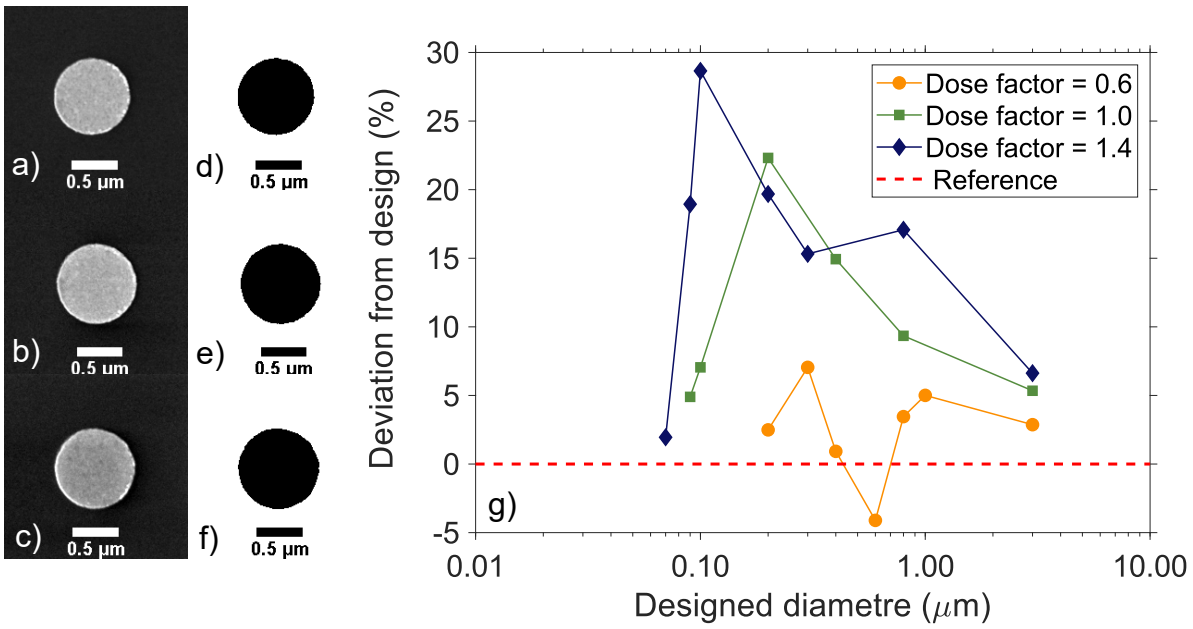

Figure 4.3: ND deposition hole diameter calibration. a)-c) SEM images of deposited Cr/Au disks for dose factors 0.6, 1.0 and 1.4 respectively. d) - f) Thresholded images of panels a) - c). g) Relative deviation from the design for the apertures created with different dose factors.

Panels d)-f) show a thresholded version of the SEM images that allow the extraction of the real fabricated diameter and compare it to the designed diameter. Panel g) shows a plot of the relative deviation from the designed aperture diameter for different dose factors. Although the design included aperture ranges from 70 nm to 3 μm for all the dose factors, the smaller diameter apertures did not clear after development for the low dose factors. The minimum clear aperture for dose factors 0.6, 1.0 and 1.4 were 200, 90 and 70 nm respectively.

Array	Substrate	**D** (μm)	Array	Substrate	**D**(μm)
A	SiNx	3.0	G	SiNx	0.2
B	SiNx	1.0	H	SiNx	0.1
C	SiNx	0.8	I	SiO_2	0.4
D	SiNx	0.6	J	SiO_2	0.3
E	SiNx	0.4	K	SiO_2	0.2
F	SiNx	0.3	L	SiO_2	0.1

Table 4.1: Template aperture arrays. Arrays of apertures of diameter **D** labeled A-L were patterned onto the PMMA template mask for two different substrates.

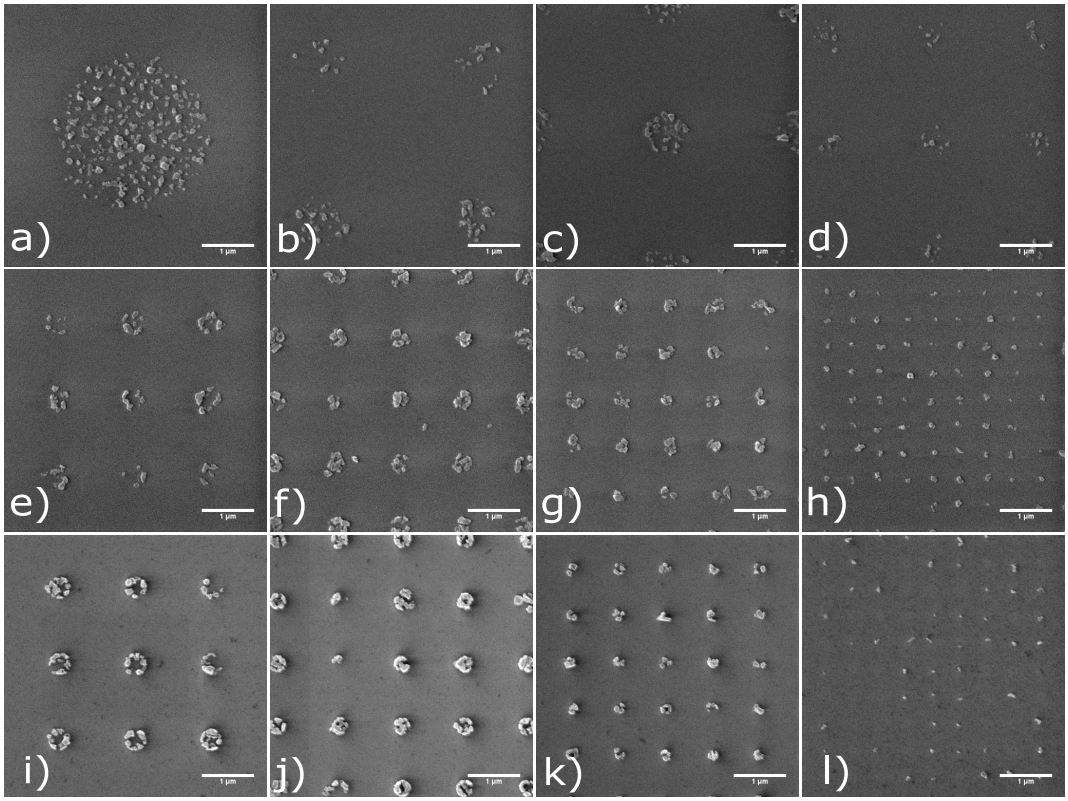

Figure 4.4: ND arrays obtained by lithographic deposition. Panels a) to l) correspond to SEM images of the arrays A-L detailed in table 4.1. All the images are 5 x 5 μm. The scale bar in all images is 1μm.

4.1.4 NDs arrays

Panels a) to l) in figure 4.4 show scanning electron microscopy (SEM) images of the deposited arrays A-L with diameters detailed in table 4.1. The separation between apertures was chosen to scale with the diameter of the apertures so the images show a clearer arrangement of the nanodiamonds. All the panels in the figure show the same field of view on the microscope (5 x 5 μm) to give a better depiction and comparison of the size of the sites achieved. The deposition yield was highly dependant on the dynamics of the suspension in the evaporation process. The images shown in figure 4.4 are from arrays that lied under the *coffee ring* stains on the PMMA template. These arrays exhibited a deposition yield > 90% for D > 200nm while the yield for arrays H and L (D = 100nm) the yield was > 50%. The rest of the array on the samples that did not ended under the stains of the dried suspension had bad deposition yields.To avoid this in the future an ultrasonic nebuliser could be used to guarantee an even mist coat of NDs on the sample [11].

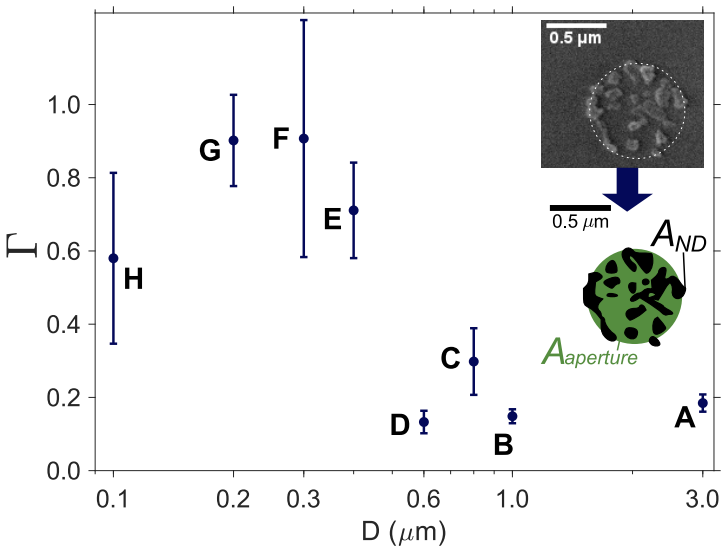

Figure 4.5: Average deposition filling factor (Γ) as a function of the template aperture diameter **D**. The error bars correspond to the standard deviation Inset shows the image processing used. SEM images of individual sites are converted to binary images. The area covered with NDs (A_{ND} shown in black) is divided by the area of the template aperture ($A_{aperture}$ shown in green) to get the value Γ.

Using the SEM images of the SiNx samples, the filling fraction of each site (Γ(**D**)) was estimated. This was done by dividing the area covered with NDs A_{ND} by the area of the template aperture used for that site $A_{aperture} = \pi \mathbf{D}^2/4$. A_{ND} is extracted by thresholding individual images of each site. Thresholding is a common digital image processing technique used to generate binary images for domain detection. A threshold value on the pixel intensity is chosen for a grayscale 8-bit image. Any pixels under the threshold are turned into zeros while those above the threshold turn into ones. When thresholding is applied to images with good contrast, a binary image that shows two different domains is obtained.

Figure 4.5 shows the extracted average filling fraction (Γ) as a function of the diameter of the template apertures. Sets of 20 sites were analysed for each diameter. Error bar values are defined by the standard deviation. The inset shows the thresholding procedure for each site analysed. The grayscale image is turned into a binary domain image where the areas covered with NDs A_{ND} (shown in black) and the background (white) can be quantified. For reference, the area of the corresponding template aperture is shown as a green circle.

The best Γ value is observed for **D** values of 300 and 200 nm. The filling fraction is related with the concentration of the ND colloidal suspension. In principle, a highly concentrated suspension should lead to a Γ close to 1 for all the diameters (provided NDs are smaller than the openings). However, with a highly concentrated suspension it avoiding re-deposition after lift-off would be more challenging.

It is worth noting that although the average value does not go above 1, for some sites the NDs would cover more area than the template opening ($\Gamma > 1$). This could mean that in some cases, NDs stack on top of each other inside the template apertures and get rearranged during lift-off.

4.1.5 NDs size distribution analysis using SEM images

Thresholding analysis also allows the extraction of the approximate size of the particles. Although this method is not completely accurate, it provides a second look to the NDs size distribution. The controlled position of the nanoparticles is not necessarily important for this analysis, although it was found that the use of these images made the thresholding easier compared to SEM images of randomly scattered NDs.

Following the same approach as the one used in the previous section, a binary image was obtained using a threshold after some contrast enhancing and speckle noise removal. Figure 4.6 a) and b) show an examples of an images of a ND sites in array A before and after thresholding respectively. The number of pixels in each domain is transformed to an area value, and from the area value a diameter value is extracted, assuming spherical particles. Images of 20 ND sites in array A were analysed, producing over 1000 diameter values. The same analysis was done with ND sites of array B (figure 4.6 c and d). The histogram of the normalised particle diameter distribution is shown in panel e) of the same figure. A broad distribution is observed with a mode value around 50 nm which matches the average size obtained with DLS. The width of the distribution should be taken carefully. The inaccuracies on the method arise from the fact that the images are a 2D projection of a 3D arrangement of particles, and is not possible to distinguish between multiple particles in contact and one big particle. Any overlap between NDs is going to account for one “particle” with a size much larger than the real size of each of the particles overlapping. The peak at the smallest values arises from errors during thresholding. From comparing panels c) and d) it is clear that the smallest “particles” in panel d) indicated with a red circle, are spurious particles that correspond of a few pixels

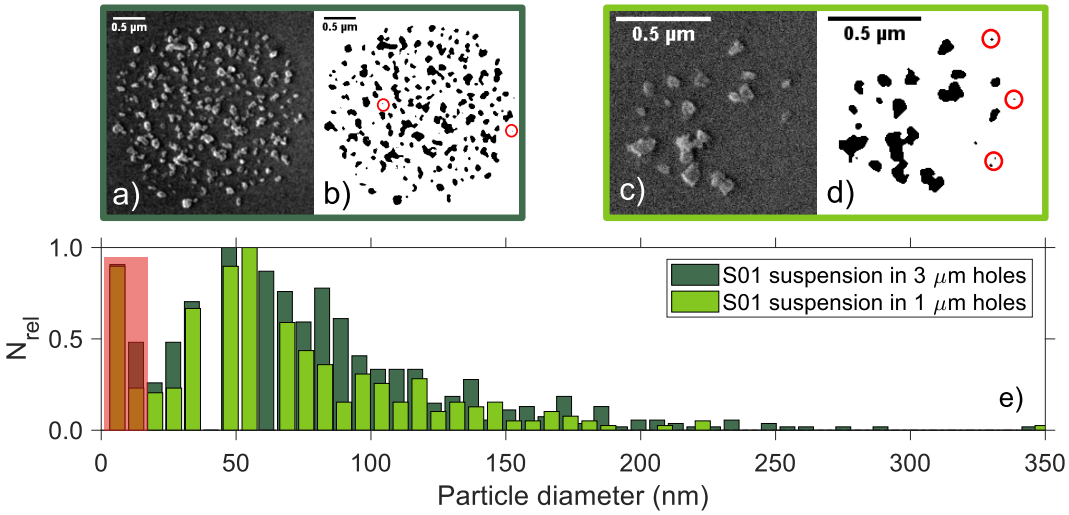

Figure 4.6: Size distribution of NDs obtained through SEM image analysis. Panel a) shows an example of an ND site created with a 3 μm aperture. The image is thresholded (panel b) and the area of each domain (black areas) is extracted. The scale bars correspond to 0.5 μm. By approximating the NDs to spherical particles, a distribution of diameters can be extracted from the images. Panel c) and d) show an example of the same image analysis procedure but with a site created by a 1 μm aperture. e) Histogram of extracted diameter values of 20 images for both 3 μm and 1 μm apertures. The columns highlighted in red have been identified as spurious pixels from thresholding errors. Examples of these cases are circled in red in panels b) and d).

of uncorrected speckle noise that were left above the threshold value and counted with the particle counting routine.

4.1.6 Optimised deposition for single NV^- centres

For the scalable fabrication of devices containing an NV^- centre, it would be attractive to find a way to guarantee the presence of at least one NV^- centre in every ND site without compromising the localisation accuracy of the NV^- centre. A quick approximation to the probability of having an NV^- centre in a ND site can derived using the filling factor Γ and the average size of the NDs d. Assuming that the NDs are spherical particles with $d = 0.05\mu$m, the number of ND in each site can be approximated by:

$$N = \Gamma\left(\frac{\mathbf{D}}{d}\right)^2 \tag{4.1}$$

where **D** is the aperture diameter. Provided the estimated number of particles in each

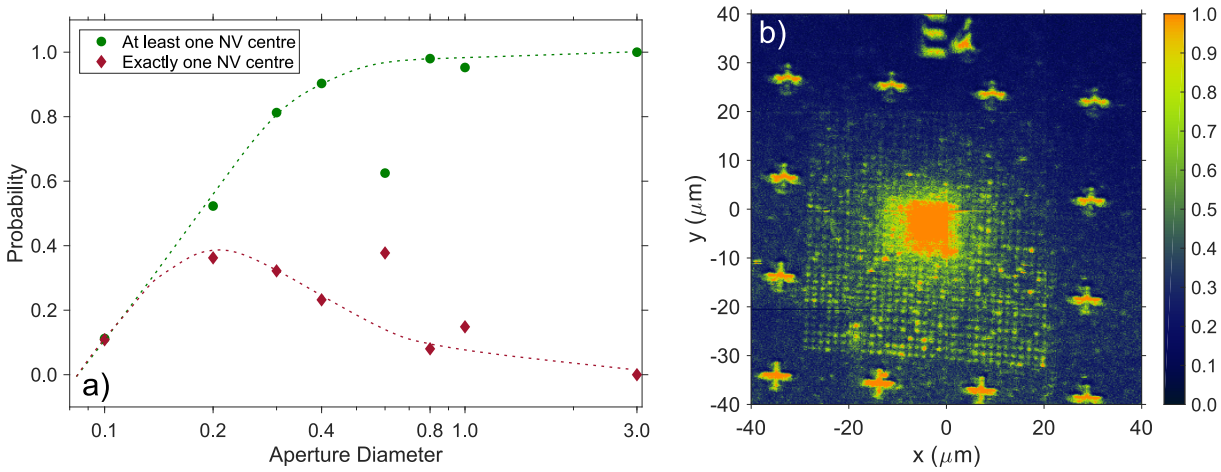

Figure 4.7: a) Probability of NV^- centre occupation on each site as a function of the aperture diameter on the template during deposition. These values are computed using γ_{ND} =5%. b) Confocal scan of an ND array on SiO_2. Large confocal scan (80 x 80 μm) of E4 array with ND sites produced by apertures with a diameter of 400 nm. The notorious bright square in the centre is substrate photoluminescence produced by the electron irradiation that the sample received when taking the SEM images.

site, the probability of finding **at least** one NV^- centre in a site can be written as $\mathbf{P} = 1-(1-\gamma_{ND})^N$ where γ_{ND} is the probability of finding an NV^- centre, in an individual ND. Alternatively, the probability of getting **exactly** one NV^- centre in a site can be written as $N\gamma_{ND}(1-\gamma_{ND})^{N-1}$. A plot of these two probabilities is shown in figure 4.7 a) for a γ_{ND} =5%. Based on this plot, is clear that sites created with apertures between 200 and 300 nm have the highest probability of having one and only one NV^- centre as it is required for many applications. A confocal scan of array E3 is shown in figure 4.7. It is perceptible that most of the sites exhibit a fluorescence above the noise level.

This approximation does not consider the broad distribution in particle sizes or the close packing limitations when Γ is large. The validity of this approximation can be tested by identifying the amount of single emitters in each site for different arrays. This would usually be done by performing intensity autocorrelation measurements ($g^{(2)}(\tau)$ measurements) on each site. However, as it was discussed at the beginning of this chapter, the time this would take made it unfeasible. A faster way to identifying single emitters within an array was needed. That lead us to explore alternative strategies detailed in the next section.

4.2 NV^- centre orientation and emission rate analysis for single emitter identification

In principle, identifying the emission coming from a single NV^- centre should be as easy as observing the magnitude of its brightness. It makes logical sense that emission coming from two or more centres should be brighter that the light coming from a single NV^- centre. The problem is that the brightness is proportional to the product of the emission rate (κ) and the collection efficiency (η), neither of which are identical for all the defects. The collection efficiency varies defect to defect, depending on the orientation of the NV^- centres. This means that two badly oriented NV^- centres could show lower brightness that one NV^- centre oriented in the optimal direction.

On the other hand, NV^- centres in nanodiamonds can have slightly different emission rates depending on the internal strain and electronic distribution. This means that there is an inherent distribution of values for the emission rate of NV^- centres in the used nanodiamonds (κ_{ND}). On top of that, the emission rate gets modified by the dielectric environment, meaning that the position and the orientation of the NV^- centre with respect to dielectric boundaries modifies the distribution of emission rate values.

Knowing the orientation of the NV^- centre and the emission rate distribution can be very valuable for engineering photonic devices around the NV^- centre. In this section, some preliminary work done on this front is shown.

While it would be possible to identify single emitters by performing intensity autocorrelation measurements ($g^{(2)}$ measurements), it would be attractive if there was a way to discern individual from multiple emitters using the acquired knowledge of the orientation and the emission rate, especially if the time taken to determine those parameters can be shorter than the long time that $g^{(2)}$ measurements take. Ideas for this alternative analysis are discussed at the end of the section.

4.2.1 Measuring the orientation of an NV^- centre

The orientation of an NV^- centre refers to the 3D direction of the axis joining the nitrogen substitution site and the vacant site in the lattice, also known as N-V axis, with respect to a defined reference frame on the sample containing the NV^- centre. One way of measuring the orientation of the NV^- centre is by observing changes in the brightness for different polarisation orientations of the linearly polarised excitation laser

(α_{exc}) with the polarisation vector co-planar with the sample plane. As mentioned in chapter 2, the emission of NV^- centres is associated with two orthogonal dipoles that lie on a plane that is perpendicular to the N-V axis. The absorption of the excitation laser is maximal when the polarisation vector matches one of these transition dipoles. An N-V axis perpendicular to the sample plane has its two transition dipoles parallel to the sample plane (figure 4.8 a), resulting in an even excitation of the NV centre regardless of the value of α_{exc}, hence no modulation in the brightness is observed.

On the other hand, for an NV centre with an NV axis parallel to the sample plane, one of the transition dipoles are contained in a plane perpendicular to the sample (figure 4.8 b). This implies that the maximum absorption is reached when the polarisation of the excitation laser matches the plane containing the dipoles, but it decreases to its minimum when the polarisation is parallel to the N-V axis. The difference between the maximum and the minimum of the measured brightness, i.e. the polarisation contrast, is a direct measure of the polar angle θ formed between the N-V axis and the optical axis (z-axis).

Enabled by the controlled deposition of ND arrays, repeated scans with different excitation laser polarisation directions can provide orientation information simultaneously for every ND site in the scan . Figure 4.8 c) and d) shows confocal scans of a section of array E from table 4.1 with horizontal ($\alpha_{exc} = 180°$) polarisation and vertical ($\alpha_{exc} = 90°$) polarisation respectively. An example of the modulation observed for the site marked with a white circle is shown in panel e). The polarisation contrast observed is 34%, indicating a large polar angle θ. For each sample and setup the polarisation contrast is limited by the background noise and the spatial profile of the laser. Tightly focused beams have longitudinal components that would deteriorate the contrast.

The technique discussed here has been used extensively for determining the orientation of NV^- centres in bulk diamond. In bulk, NV^- centres can only be oriented in 4 directions relative to the plane the diamond was cut. For example, Alegre and co-authors used this technique over a diamond sample cut along the {111} plane, allowing them to distinguish the four different possible orientations, and based on those verify spin polarisation selection rules [96]. Similarly, this technique was used to quantify the changes on the orientation of NV^- centres for a sample that was subjected to long periods of annealing at high temperatures [97].

For NDs, things are more challenging. Although technically NV^- centres in NDs

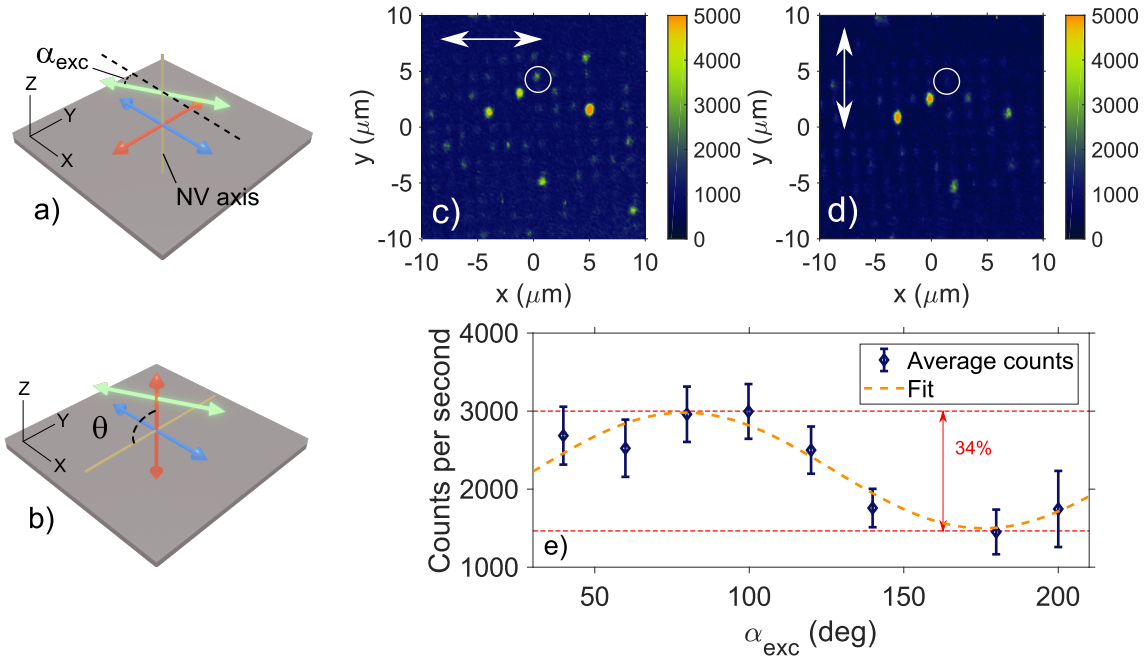

Figure 4.8: Polarisation dependent brightness. Panels a) and b) illustrate two extreme cases. For an NV axis perpendicular to the sample plane. Panels c) and d) are close up confocal scans on the array of ND sites shown in figure 4.7. The scans were taken with horizontal and vertical excitation laser polarisation, respectively. It is noticeable that some ND sites change brightness under different excitation laser polarisation orientations while some others do not. Panel e) shows the brightness (counts per second) of a specific site (marked with a circle) for different excitation laser polarisation angles on the sample plane. The modulation in brightness has a contrast of 34%.

would have the same 4 allowed orientations than in bulk diamond, NDs land on random orientations on whichever substrate is used, leading to arbitrary orientations for the NV^- centres. Using the polarisation rotation of a linearly polarised excitation laser, it is difficult to distinguish between similar orientations. This has been clearly exposed in [98]. In that study, Dolan *et. al.* compare the technique discussed here with the use of structured beams and optically detected magnetic resonance (ODMR) to determine the orientation of NV^- centres in NDs, claiming a good advantage when using structured beams.

4.2.2 Emission rate of NV^- centres in nanodiamonds

The spontaneous decay rate of an NV^- centre optical transition in bulk diamond is defined by variables that are internal to the diamond structure. However, when the NV^- centre is near the surface, as it would be in a thin membrane or in NDs, the emission

rate is modified by the "presence" of the material boundaries.

The spontaneous emission rate of an electrical dipole in the vacuum (γ_0) changes in the presence of material interfaces. The change comes from the electric field experienced by the electric dipole $\vec{\mathbf{p}}$, which, in turn, is its own "retarded" field generated by the dipole in previous moments and which has been reflected in the interfaces between different media. In the context of quantum electro dynamics (QED) this change is known as Purcell effect and the factor of change is known as the Purcell factor.

The modified emission rate (γ) can be calculated using the Green dyadic function $\overleftrightarrow{\mathbf{G}}$ with the expression

$$\frac{\gamma}{\gamma_0} = \frac{6\pi c}{\omega_0}\left[\vec{\mathbf{n}_\mathbf{p}} \cdot \mathrm{Im}\left\{\overleftrightarrow{\mathbf{G}}(\vec{\mathbf{r}_0}, \vec{\mathbf{r}_0}; \omega_0) \cdot \vec{\mathbf{n}_\mathbf{p}}\right\}\right] \tag{4.2}$$

where ω_0 is the frequency of the field, c is the speed of light in vacuum, $\vec{\mathbf{n}_\mathbf{p}}$ is the unitary vector in the direction of the dipole $\vec{\mathbf{p}}$ located at the position $\vec{\mathbf{r}_0} = (x_0, y_0, z_0)$. For the simple case of an electric dipole above a glass surface, the relative change in emission rate $\frac{\gamma}{\gamma_0}$ is given by the following equation (4.3) that was derived from equation 10.26 of [99].

$$\begin{aligned}\frac{\gamma}{\gamma_0} = 1 + \frac{{p_x}^2 + {p_y}^2}{|\mathbf{p}|^2}\frac{3}{4}\int_0^\infty \mathrm{Re}\left\{\frac{s}{s_z}\left[r_s - s_z^2 r_p\right]\exp\{2ik_1 z_0 s_z\}\right\} ds \\ + \frac{p_z^2}{|\mathbf{p}|^2}\frac{3}{2}\int_0^\infty \mathrm{Re}\left\{\frac{s^3}{s_z} r_p \exp\{2ik_1 z_0 s_z\}\right\} ds.\end{aligned} \tag{4.3}$$

In this expression, the dipole is located at a distance z_0 from the surface with a polarisation vector $\vec{\mathbf{p}}$ with components p_x, p_y and p_z. The equation is split in two terms that correspond to the in-plane and out-of-plane components of the dipole orientation. Each term is a summation over all the plane waves reflected from the surface with propagation k. The summation is over the variable s defined as $s = k_\rho/k_1$ with k_ρ the radial component of the k-vector of the plane wave normalised by k_1 defined by $k_1 = \sqrt{\epsilon_1\epsilon_0\mu_1\mu_0}\omega$ with ϵ_1 (ϵ_0) the electric permittivity of the dielectric (vacuum), μ_1 (μ_0) the magnetic permeability of the dielectric (vacuum) and ω the frequency of the field. Finally, the quantities r_p and r_s are the Fresnel coefficients of reflection for p-polarised and s-polarised light, respectively.

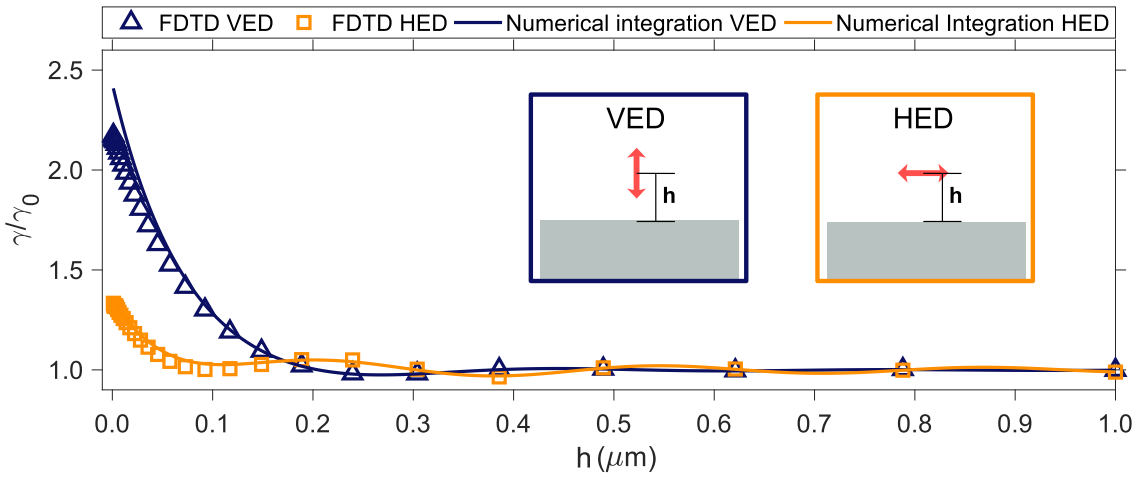

Figure 4.9: Spontaneous emission rate enhancement of an electric dipole near a dielectric surface. The change in the emission rate depends on the orientation of the dipole and the separation (h) from the surface. Solid lines are the numerical solution to equation 4.3 for a vertical electric dipole (VED) and an horizontal electric dipole (HED). Shown with triangles and squares are the 3D FDTD simulations of the same physical system for a VED and a HED, respectively.

Using numerical integration on the integral terms, the emission rate change of an electric dipole emitting at the NV^- centre zero phonon line (λ =637 nm) as a function of the distance to a SiO_2 surface was computed. Solid lines in figure 4.9 show the results for an electric dipole oriented horizontally (HED - parallel to the surface) and for a vertical dipole (VED - perpendicular to the surface). The chosen integration trajectories in the complex plane were the same trajectories as the ones described in [100].

A model of this same physical system was simulated using 3D FDTD simulations. The emission rate change of a VED and a HED at different heights from the SiO_2 surface is shown in figure 4.9 marked with triangles and squares, respectively.

For NV^- centres in NDs, the change in emission rate would be caused by the diamond-substrate interface as well as the diamond-air interface. Confident that FDTD simulations matched the analytical expressions for the previous case, the change of the emission rate for an electric dipole inside a ND site was simulated. The ND site was modeled as a diamond disk with 300 nm diameter and 100 nm height. This disk represents sites obtained by the lithographic deposition. The diameter was chosen to match the sites in arrays F as these showed the best filling fraction and the best chance of getting exactly one NV^- centre. Results are shown in figure 4.10 a). The first thing to notice is that,

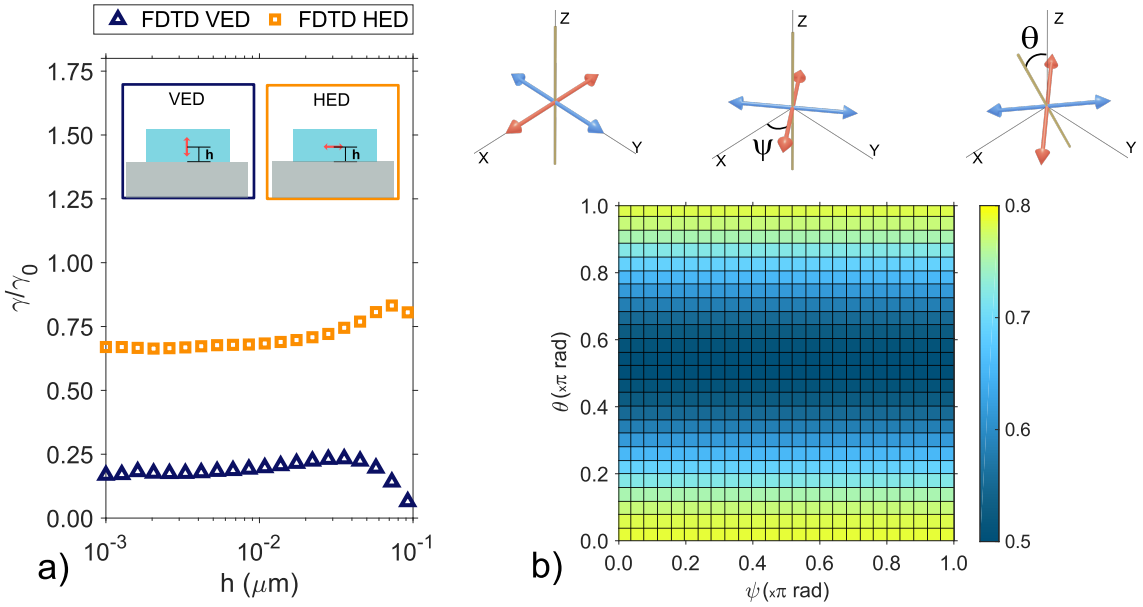

Figure 4.10: Spontaneous emission rate reduction of an electric dipole inside a diamond disk. 3D FDTD simulations of of a VED and a HED inside a diamond disk were performed. The emission enhancement as a function of the distance between the substrate and the dipole are plotted with triangles and squares for a VED and a HED, respectively. b) Emission rate change for an NV^- centre for different orientations inside a diamond disk.

since the dipole is in a medium with a higher refractive index than the substrate, the emission rate gets suppressed instead of enhanced ($\frac{\gamma}{\gamma_0} < 1$). The height h was only varied for values inside the diamond disk. It is noticeable that the difference between a VED and a HED is roughly a factor of 3 and remains almost constant with changes in height.

Furthermore, for a more realistic description, the two orthogonal dipoles of an NV^- centre were simulated for a centre with arbitrary orientations. The simulated orientations were obtained by three consecutive rotations to the NV^- centre. Starting with the N-V axis aligned with the Z-axis, a rotation along z-axis by an angle ψ, followed by a rotation along the x-axis by an angle θ, followed by a rotation of along z-axis by an angle ϕ would lead to an arbitrary orientation in space. However, the last rotation along the z-axis can be avoided given the cylindrical symmetry of the model. Figure 4.10 b) shows a map of the change in joint emission rate of both dipoles for different orientations defined by angles ψ and θ. It shows that only the polar angle θ affects the degree of change in the emission rate, and that the maximum difference is between a perpendicular NV^- centre and parallel NV^- centre by a factor of 1.6.

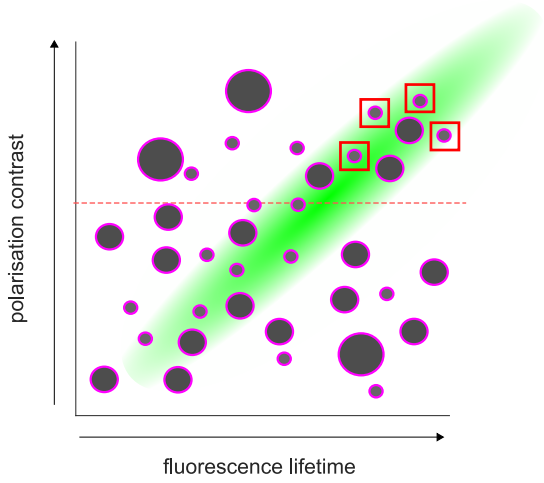

Figure 4.11: Hypothetical scatter plot of polarisation contrast and fluorescence life time of ND sites. The maximum brightness measured for each site is encoded in the diameter of each dot. A correlation between the polarisation contrast and the fluorescence lifetime is expected for single emitters (marked in green). The dashed red line marks the imposed threshold for single emitters N-V axis is aligned with the sample plane. The ND sites that fulfill the requirements are likely to have individual NV^- centres and are marked in a red square

The difference between the largest and smallest emission rates can change depending on the characteristics of the diamond disk and the position of the emitter inside the diamond. For simplicity, the simulations shown here assumed that the emitter was in the centre of the diamond disk in the X-Y plane, however Monte Carlo simulations of all the possible orientations and positions inside diamond disks of different sizes could give a better understanding to the distribution of emission rates that one can expect across arrays of NDs.

Nevertheless, assuming that different positions within the NDs preserve the trend in the polar angle dependence, there is an interesting correlation that emerges from the orientation effects in collection and emission rate. It is worth noting that for an NV^- centre with its N-V axis parallel to the substrate plane ($\theta = 90°$), the polarisation contrast is maximal while the emission rate would be minimal, hence the measured lifetime would also be maximal. Conversely, if the NV^- centre is perpendicular to the substrate plane, the polarisation contrast is minimal and the emission rate is maximal, leading to shorter lifetimes.

By repeatedly scanning a ND array with a pulsed laser and with different polarisa-

tion angles, it should be possible to extract the polarisation contrast and fluorescence lifetime of every ND site and to assign each site a point in the polarisation contrast vs fluorescence lifetime space as depicted in figure 4.11. Our hypothesis is that individual NV^- centres should show up in the region defined by the correlation previously described (marked in green). Sites with multiple emitters should show most of the times a low polarisation contrast, given the fact that it is unlikely to have two or more emitters with the same orientation within the same site. In the pathological case when this happens the measurement of the brightness of the ND site should provide a way to distinguish between individual and multiple emitters, provided that each of these emitters present the same collection efficiency. In the same diagram, the brightness is encoded with the radius of each dot and the threshold between "low" and "high" contrast is shown with a dashed line. By combining all three criteria (high polarisation contrast, long lifetime and low brightness compared with ND sites in the same region), *some* single NV^- centres can be identified with a confidence that dependant on the threshold value. This threshold would initially be arbitrary but refined upon verification of this method and statistical analysis of data collected using this approach.

This method should reduce the time taken to identify *some* single NV^- centres compared to performing $g^{(2)}$ measurements on each site. Unfortunately, this method does not identify *all* the single NV^- centres, since it would be difficult to discern centres oriented perpendicular to the substrate plane that exhibit low polarisation contrast from multiple emitters showing equally low polarisation contrast. Verifying that this method provides identification of single NV^- centres is part of the scope and the future work of this project.

CHAPTER 5

TOWARDS ENHANCED PHOTON EMISSION OF AN NV^- CENTRE USING CIRCULAR BRAGG GRATING RESONATORS

Throughout this thesis, a photonics platform compatible with NV^- centre encapsulation has been found, and spatial control over nanodiamonds (NDs) containing NV^- centres has been demonstrated. Now, by combining these two results it is possible to fabricate photonic devices around positioned NV^- centres.

As exposed in chapter 2, optical resonators or optical cavities are fundamental for the enhanced emission of indistinguishable photons coming from NV centre ZPL. The design of these cavities is dependent on the specific application. Cavities that funnel emission into photonic integrated circuits are very useful components for applications such as quantum sensing and quantum information (QI) processing using solid state spin systems. In contrast, cavities that out-couple light into either free space or optical fibres are more suitable for long distance quantum communications.

Whilst the long-term goal of this project is to create spin-photon interfaces that enable entanglement between multiple NV^- centres on the same chip, for this thesis the aim was to take the first steps towards creating photonic devices based on the nanoparticle integration approach. For this first demonstration, using cavities that coupled light out of the sample was a more suitable approach, since the equipment required for testing

these kind of cavities was already available (see appendix **??**). Furthermore, polarisation insensitive cavities were desirable due to the lack of control on the orientation of the NV^- centres. Provided these requirements, an ideal solution was found in the use of Circular Bragg Grating (CBG) resonators.

A circular Bragg grating (CBG), also called bulls eye gratings, consists of concentric periodic rings etched into a material layer forming a circular dielectric grating around a central disk. Depending on the period chosen for the grating and the radius of the central disk, these structure can be used to simply promote the momentum transfer required to couple slab guided modes into radiative space [101], or to create a resonator with a mode "trapped" in the central disk enabling, for example, surface-emitting semiconductor lasers [102].

The first use of CBGs involving single quantum emitters was demonstrated in 2011 by Davanço and co-workers [103]. They used a suspended GaAs membrane containing quantum dots sefl-assembled (QDs) at half of the membranes thickness. The CBG is partially etched around a single QD enhancing the emission rate and the collection efficiency. The partial edge brakes the symmetry of the system and by carefully controlling the etch depth, maximal directionality in the extraction direction is achieved. A follow up of this work was published in 2015 by Sapienza *et. al.* [104] where a PL imaging technique is presented to determine the position of self-assembled QDs and fabricate CBG resonators around them. The average position uncertainty obtained (< 30nm) allowed them to achieve a collection efficiency of 48% and Purcell factor values of 4.

A similar approach was demonstrated for an NV^- centre in a thin (< 1 μm) diamond membrane on glass a few years after [24]. In this work, the authors demonstrate the use of a CBG to achieve an increase in the amount of collected photons. However, they do not comment on the enhancement of the emission rate of the NV^- centre.

A change in the paradigm came in 2019 with the inclusion of a metallic back-reflector underneath the CBG grating to recover light emitted downwards. This was demonstrated almost simultaneously by Wang *et. al.* [105] and Liu *et. al.*[106]. In both publications the authors use a Au layer under a GaAs CBG resonator to extract entangled photon pairs by cascaded biexciton-exciton processes. They found that the addition of the back-reflector provided the collection efficiency necessary to demonstrate remarkable figures on pair collection, photon indistinguishability, and entanglement fidelity.

Since the introduction CBG resonators with a back-reflector, many studies have been published using this geometry to extract light from single quantum emitters. In particular, the community working with 2D materials has taken advantage of these devices [107] [108].

Since the nanoparticle approach that is subject of study in this thesis does not need to use bulk diamond, the design of the devices could be based on any set of layers. In this sense, the design of the CBG resonator used here was based on the ideas of [105] and [106] where an Au thin film was included under the resonator to redirect the emission to the collection direction. The inclusion of this mirror needs a dielectric spacer to be able to create constructive interference between the light emitted directly upwards with the one that originally was emitted downwards and got reflected by the mirror. Opposed to the approach of Davanço *et. al.* [103] and [24] where the CBG resonators are made by partially etching the circular grating onto membranes of the material containing the field, the approach taken allows us to have fully etched gratings since the guiding material layer is supported by the SiO_2 spacer. Having fully etched gratings in principle increases the Q of the resonator, however the contrast between the SiNx and the SiO_2 is smaller than that of suspended diamond or GaAs, decreasing the value of Q.

5.1 Design of a CBG resonator for the enhancement of the NV^- centre zero phonon line emission.

The CBG resonators optimised design parameters were obtained by a series of iterations of finite-difference time-domain (FDTD) simulations. The simulated Purcell enhancement of a broadband electrical dipole source parallel to the device plane was recorded on each iteration. The resonant wavelength of the resonator can be observed as a peak in the Purcell factor (F_p) as a function of wavelength, while the width of this peak is related to the quality factor Q of the resonator. In the simulations, the dipole source was place inside a SiNx film. The parameters of the device were optimised to match its resonance to the zero phonon line (ZPL) of the NV^- centre emission.

As a starting point, the grating period Λ was chosen to satisfy the second-order Bragg condition where $\Lambda_0 = \lambda_{zpl}/n_{TE}$, with λ_{zpl} being the ZPL wavelength ($\lambda_{zpl} = 0.637\mu$m) and n_{TE} the effective refractive index of the TE slab mode of a SiNx film of thickness t_{SiNx}. For example, with a film thickness of 300 nm, the resulting period value is $\Lambda_0 = 383n$m.

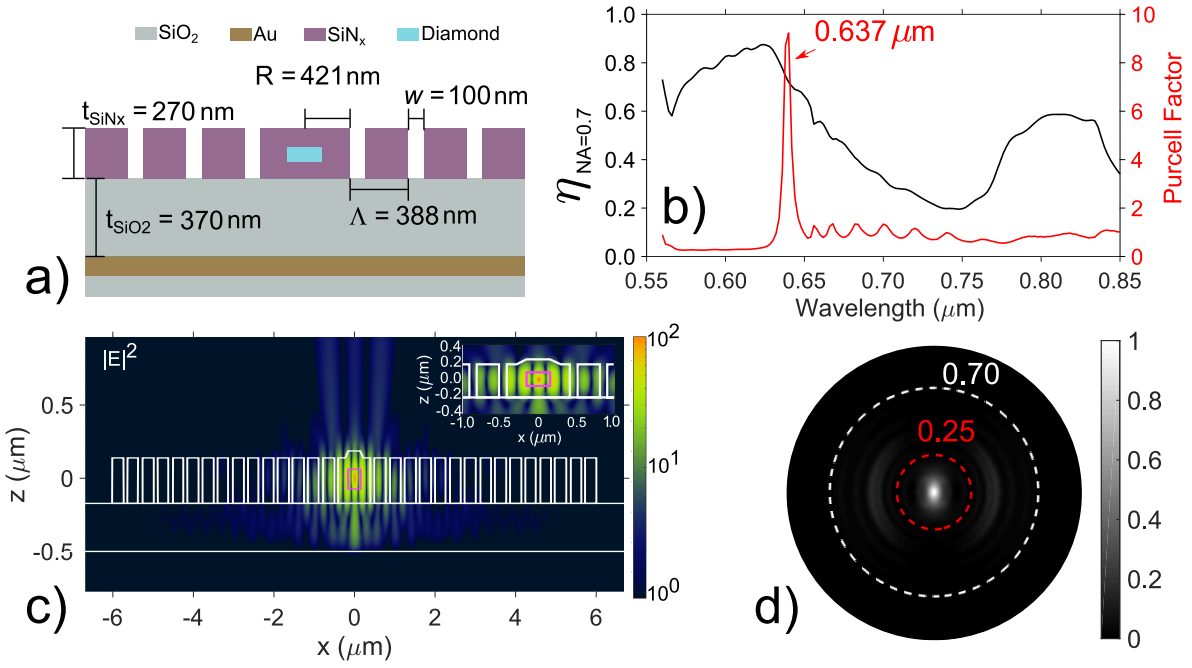

Figure 5.1: Circular Bragg grating (CBG) resonator. a) Schematic with the parameters of the optimised simulated structure with radius R, grating period Λ, a separation between rings w and t_{SiO2} and t_{SiNx} the optimal SiO_2 and SiNx film thickness values. b) Simulated Purcell factor F_P (right axis) and collection efficiency with a lens with $NA = 0.7$ (left axis) $\eta_{NA=0.7}$ showing a resonance at λ_{ZPL}. c) Electric field intensity ($|E|^2$) profile for a radial cut on the CBG. The inset give a closer look to the central disk. d) Normalised far field projection of $|E|^2$ emitted in the $+z$ direction. The white (red) dashed line shows the limit of the collected light with a microscope objective with NA of 0.7 (0.25).

The radius of the central disk R determines the shape of the resonators' mode. Following a similar approach to the designs in [105] and [24] a $\frac{5\lambda}{2}$ mode is obtained with an R value close to $R_0 = \Lambda$. The choice of the mode depends on the desired application. Higher order modes like the $\frac{9\lambda}{2}$ mode shown in [103] and the $\frac{11\lambda}{2}$ mode demonstrated in [108] can exhibit higher quality factors, but the far-field mode profile becomes less regular making it challenging to couple to other optical elements like optical fibre for detection or to excite the mode efficiently through resonance fluorescence. On the other hand, while a $\frac{3\lambda}{2}$ mode can have a better mode matching to a single mode fibre, it presented challenges as the central disk would have had a size comparable to the aperture used to deposit the nanodiamonds leading to tighter restrictions on the positioning accuracy. Finally, the design of the CBG resonator includes a Au thin film mirror under the SiNx CBG separated by a SiO_2 spacer. This mirror is used to redirect light emitted towards

the substrate upwards. The thickness of the spacer t_{SiO2} is chosen such that there is constructive interference between the light reflected and the light originally emitted in an upwards direction.

As in section 4.2, the simulations considered a 300 nm wide (diameter) and 100 nm tall diamond disk at the center of the CBG resonator and encapsulated within the film. The height of the disk is an estimation of the height of the ND site considering some NDs might be piled up. A SiNx disk of the same dimensions was added to the model at the top of the central disk to mock the mound formed by the encapsulated NDs.

A multi-parameter optimisation was used to find the best design parameters. A particle swarm routine, included in the FDTD software, was used to find parameters that maximised the Purcell factor at the ZPL wavelength while keeping a collection efficiency $\eta_{NA=0.7}$ above the value obtained from the bare ND sitting on the SiO_2 + Au substrate. The values to optimised were the central disk radius R, the period of the grating Λ, and the thickness of the SiNx film t_{SiNx}. The optimised design parameters are shown in figure 5.1 a). The spacing between rings in the grating w = 100nm was not changed during the optimisation. This value was fixed to stay above the limits of the fabrication procedures. A grating period of $\Lambda = 388$ nm and a $R = 421$ nm were found to produce a resonance centred at λ_{zpl}. The optimised SiNx film and SiO_2 spacer are $t_{SiNx} = 270$ nm and $t_{SiO2} = 340$ nm, respectively.

Figure 5.1 b) shows the Purcell factor for the optimised design (right axis). The resonance showed is centred at λ_{zpl} with a full width half maximum (FWHM) of 5 nm, which means that the resonator has a relatively low Q factor of approximately 130. The same panel shows the collection efficiency $\eta_{NA=0.7}$. This represents the fraction of the total emitted power that gets directed upwards and collected by a microscope objective with a numerical aperture (NA) of 0.7.

The intensity of the simulated electric field at the resonance frequency can be seen in figure 5.1 c). It shows that most of the propagation is directed in the $+z$ direction. Overlaid with the electric field is the outline of the CBG structure (white line) including the diamond disk encapsulated in the central disk of the resonator (pink line). The inset shows a detailed close up of the mode profile in the central disk. It can be seen that the resonant mode indeed corresponds to a 5-lobe mode ($\frac{5\lambda}{2}$) as intended. The normalised far field projection of $|E|^2$ emitted in the $+z$ direction at the resonance frequency can be observed in panel d). The white (red) dashed line shows the limit of the collected light

with a microscope objective with NA of 0.7 (0.25).

5.2 Fabrication

Once the optimal design was found, sets of CBG resonators were fabricated on a 10 x 10 mm chip. Fifteen sets of arrays of sixty four devices arranged in a grid of eight columns labeled 00 to 07, and eight rows labeled A to H. This way, each individual resonator has a unique identifier. For instance device D1206 corresponds to the device in row D and column 06 of array 12. Throughout these sets, the central disk radius of the devices was varied for each column being devices in row D the ones with the original design with a central disk radius of 421 nm. The fabrication of these devices required the use of electron beam lithography in three steps. This means that overlay of 3 different layers was needed. A step-by-step explanation of the fabrication process is depicted in figure 5.2 and explained below:

1. A piece of SiO_2-on-Si wafer was cleaved and solvent cleaned following the procedure explained in chapter 3. The SiO_2 on the top of the wafer has a thickness of 1 μm.

2. Using thermal evaporation, a 100 nm thick Au film was deposited to form the back reflector. The FDTD simulations showed that 100 nm was enough to get the maximum reflection.

3. Using PECVD, a 340 nm thick film of SiO_2 was deposited. PECVD allows deposition of amorphous material at relative low temperatures preventing the damage of other layer like the Au film.

4. A set of metallic markers and labels were deposited using electron beam lithography and thermal evaporator. These markers will become crucial to the rest of the fabrication process since the overlaying of lithography processes needs some reference/alignment marker.

5. The deposition of the SiNx film is divided in two. Half of the thickness of the film (135 nm) is deposited by PECVD using the recipe described and analysed in chapter 3.

6. Following the positioning procedure detailed in chapter 4, nanodiamond (NDs) sites were created at the centre square areas defined by the crosses deposited in step 4.

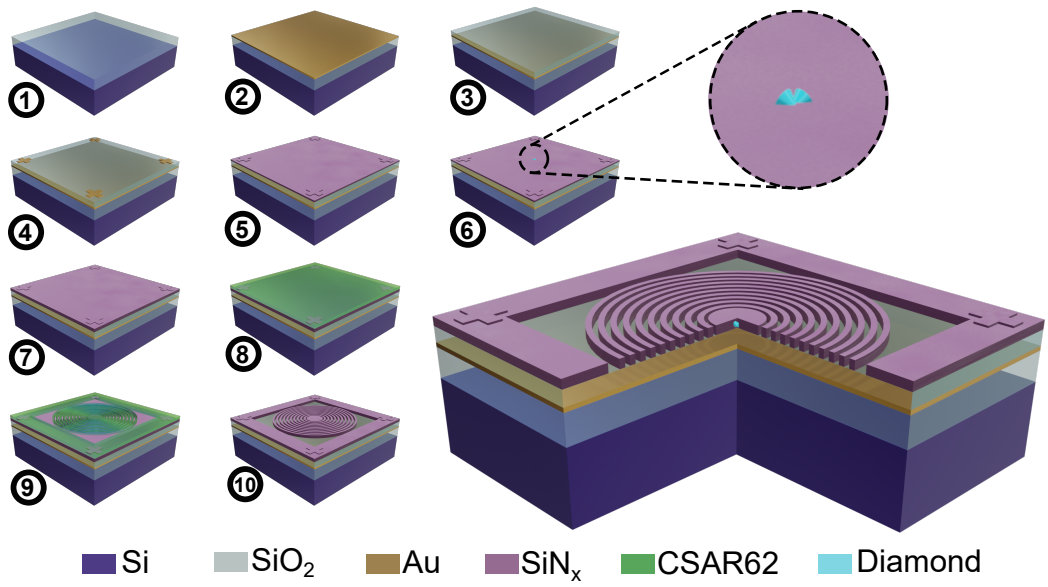

Figure 5.2: CBG resonators fabrication process. 1.Solvent cleaned substrate. 2.- A Au mirror is deposited 3.- PECVD SiO_2 spacer is added 4.- Metallic alignment markers are added 5.-A 135 nm thick (half of the final thickness) SiNx film is deposited using PECVD. 6.- Following the procedure detailed in chapter 4, nanodiamonds (NDs) are positioned 7.- The rest of the SiNx is deposited producing resulting in a 270 nm thick film with encapsulated NDs inside the film. 8.- High contrast EBL resist spin-coating 9.- EBL of the CBG resonators 10.- Reactive ion etching is used to transfer the CBG pattern to the SiNx film

As explained previously, to have the best chance of having exactly one NV^- centre, the diameter used for the deposition was D =300 nm. The deposition success was tested for each site by optical means.

7. The rest of the SiNx was deposited (135 nm) resulting in a 270 nm thick film with encapsulated NDs inside the film.

8. A 400 nm thick layer of EBL resist (CSAR62) was spin-coat. It is a high selectivity resist

9. Using EBL the resonators were patterned on the resist. The CBG resonators need to be aligned with the NDs. The overlay is again aligned using the auxiliary markers created on step 4. Details of the dose calibration for the CBG structures are discussed on the next section

10. By the use of reactive ion etching (RIE), CBG pattern is etched on the SiNx film.

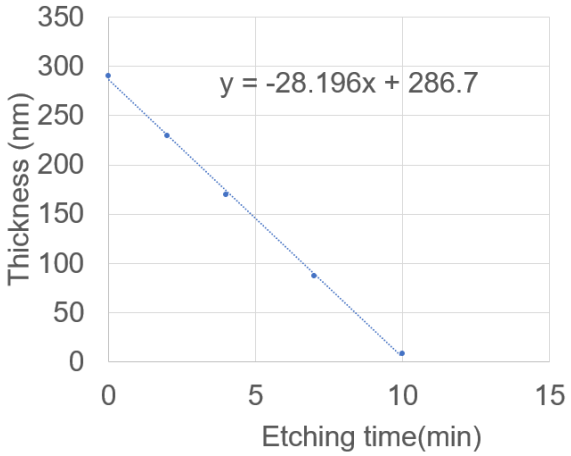

Figure 5.3: Etching rate calibration for N-rich SiNx. The linear fit shows an etch rate of approx 28 nm per minute.

Most of these fabrication steps required careful calibration. The details of the calibration of EBL dosage and the dry plasma etching recipe and the etch rate calibration are explained in the next section.

5.2.1 Calibration of the etch rate of SiNx using reactive ion etching

The transfer of the pattern from the CSAR62 mask to the SiNx film was done using Reactive Ion etching with a plasma using CHF3 (40sccm) and SF6(9sccm) at a pressure of 5 mTorr, an RF power of 50 W, and a temperature of 30 °C. To be able to control the amount of material etched on the CBG structures, the etch rate of the process used had to be characterised. Starting with a SiNx film of a thicknes of 286 nm deposited on a Si substrate, the film was exposed to RIE in steps of 2 minutes measuring the thickness of the film after each step until the film had been completely etched. The data, shown in figure 5.3 shows a good linear trend. A linear fit of the data points shows that the etch rate is 28.2 nm per minute (figure 5.3)

5.2.2 Calibration of the electron beam lithography feature size using CSAR62

For the patterning of structures in SiNx a high-selectivity resist (CSAR62 from Allresist GmbH) was used. High-selectivity is a relative term used to describe when two materials

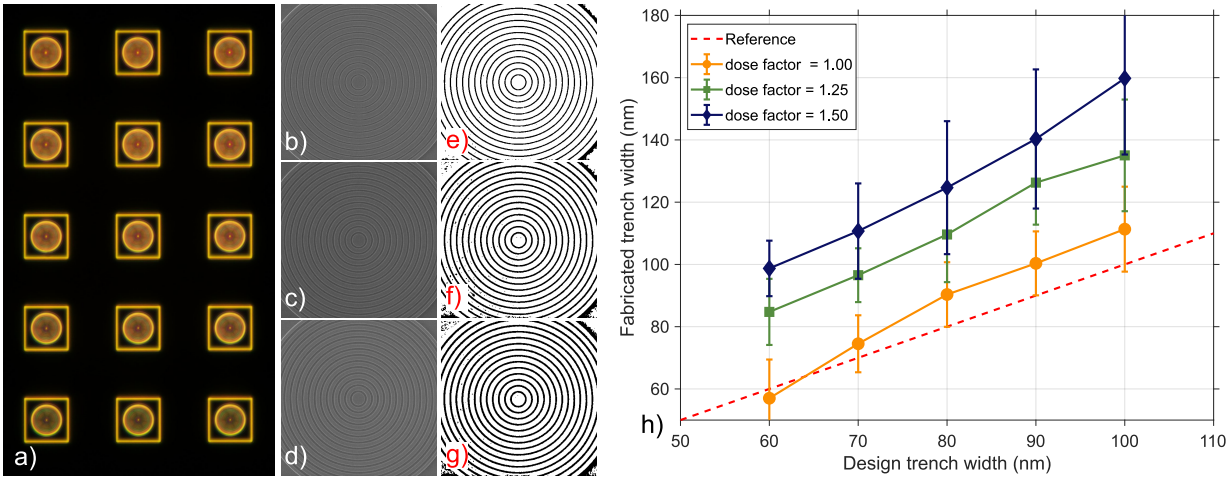

Figure 5.4: Trench width calibration. a) Dark field microscope image of one of the set of devices fabricated with for calibration. b)-d) SEM images of three different devices. e)-g) Binary images that allow the extraction of the average trench width values. h) Plot of the actual fabricated trench width vs the design for different dose factors.

(in this case the EBL resist and SiNx) etch at significantly different rates. The use of a high-selectivity resist allowed for a full etching of the SiNx film whilst keeping a relatively thin resist thickness and therefore allowing a higher resolution.

The resist was deposited by spin-coating 30μl of CSAR62 at 4000 rpm for 60 seconds to get a 400 nm mask. The mask was then baked at 150°C for 60 seconds. The base dose used was 160 $\mu C/cm^2$. After exposure, the pattern was developed by dipping the sample in the developer(All-resist) for 70 seconds followed by rinsing in the stopper(All-resist) solution for 10 seconds. The composition of these chemicals is unknown but are supplied from the same company as the resist and are designed for CSAR62. After etching, the resist is removed by the own brand remover.

For the fabrication of the CBG resonators, a calibration of the obtained line thickness needed to be made. A piece of wafer with the stack shown by figure 5.2 was used for this calibration test, although the silicon nitride used was near-stoichiometric silicon nitride instead of nitrogen-rich silicon nitride. Circular Bragg grating resonators with different designed trench widths were patterned onto the CSAR62 mask using different dose factors.

Dry etching was used to transfer the pattern to the silicon nitride film. After removing the mask the fabricated grating were analysed by optical and electron microscopy. Figure

5.4 a) shows a dark field microscopy image of the fabricated devices. The actual fabricated width for the trenches between the concentric rings was extracted by analysing SEM images of the devices. Figure 5.4 b)-d) shows the SEM images, and panels e)-g) show the processed images that allowed the extraction of the trenches width. Panel h) shows the results found. The red dashed line is for reference and represents the ideal case of transfering the design perfectly without any broadening. The average measured width values are plotted for different trench width values given to the EBL system and dose factors. A linear homogeneous broadening of the trenches is observed. This calibration provided the guide to determine the design trench width and dose factors needed to compensate for the broadening and obtain fabricated devices with features close to the optimised design.

5.2.3 Device inspection

After the ND deposition in step 6, the sample was inspected using dark field optical microscopy to assess the success of the deposition. Figure 5.5 a) shows one of the images taken through this inspection process. The scattering coming from the centre of the image confirms the presence of NDs. Unfortunately, not all the sites were populated. A success yield of 35% was achieved for this sample. As explained in chapter 4, the deposition has a good yield only for the apertures under the ring left upon the evaporation of the solvent (coffee ring effect). Achieving a better yield over larger areas is part of the goals for the work ahead on this project.

Panels b) and c) of 5.5 show bright field images of the fabricated devices. Panel b) shows one of the arrays containing 64 devices. The device array spans an area of 400 μm. Panel c) is a close up look to one of the devices. Limited by diffraction, optical microscopy can not resolve the grating structure. Although, the scattering observed resembles the scattering produced in a LP record expected from a circular grating.

To be able to resolve the grating, scanning electron microscopy (SEM) is needed. Figure 5.5 d) shows SEM images of the NDs deposited for device A405, a different device that the one showed in panel c). The NDs are extended with an irregular shape and not in a circular shape as expected. From panels e) it is clear that the NDs were accurately deposited at the centre of the area where the resonator was going to be patterned. The mound formed by the capped NDs can be observed in the central disk. Panel f) shows that the grating obtained has a good fidelity and shows good azimuthal uniformity.

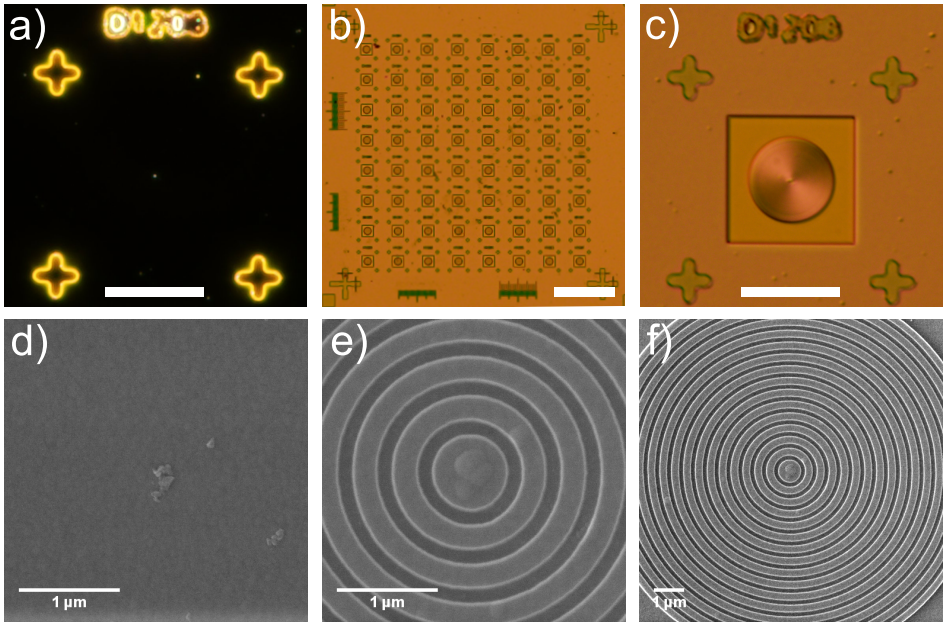

Figure 5.5: Inspection of fabricated devices. a) Dark field image of the deposited ND for device D1206 before encapsulation and patterning (scale bar = 15μm). b) Optical microscope image of the array of devices (scale bar = 100μm). c) D1206 Finished device (scale bar = 15μm). d) SEM image of the NDs deposited at the centre of device A405 prior capping and etching. e) SEM image of the finished device (A405) using the same field of view than panel d. The mound formed by the encapsulated NDs can be observed. f) Larger view of device A405 showing good uniformity in the grating.

It is important to point out that, as it was shown in figure 4.7 in chapter 4, SEM creates a high density of photoluminescent defects in the irradiated area making it impossible to detect single NV^- centres in the region that was irradiated for imaging. This means that devices inspected using SEM, become unusable for future use. For this reason only a few devices were examined using this technique.

Once the devices were fabricated it was necessary to check whether the devices were in fact resonators with their resonances at the designed wavelength. The two techniques used to asses the resonators' performance are described in the next section.

5.3 Determination of the resonance of fabricated devices via reflectance measurements

Before attempting to detect any NV^- centre emission couple to the resonators, testing the actual spectral response of the resonators was necessary. In order to do so, the spectral reflectance of the structures was measured using the setup shown in figure 5.6. A tunable laser was focused on the sample with the use of a microscope objective with a NA = 0.25, forming a 12 μm diameter spot on the CBG resonator. The reflected light was collected back with the same microscope objective and separated from the laser path using a quarter wave plate and a polarising beam splitter. The central wavelength of the laser was varied in 1 nm steps. With each step, the reflected power normalised by the power incident on the sample was recorded. The obtained curve is called spectral reflectance often simply called reflectance (R). The reflectance produced by the CBG resonators was compared with the reflectance of the unpatterned sample stack of SiNx, SiO_2 and Au films to separate the features produced by the stack to those produced by the CBG resonator.

The light source used was a supercontinuum source (NKT Photonics SuperK) coupled to an acousto-optic tunable filter (AOTF) (NKT Photonics SuperK Select). This system is capable of delivering tunable laser emission with a linewidth of around 1 nm. The output of the filter is coupled to a polarisation maintaining fibre (PMF). The light is collimated and passed through a half wave plate (not in the diagram) and set to vertical polarisation. Then, the laser is directed to a polarising beam splitter (PBS) where it gets reflected, passed through a quarter wave plate (QWP) that turns the vertical polarisation into circular polarisation, to a microscope objective with numerical aperture NA = 0.25 that focuses the light on the sample. To guarantee that the laser is being focused on the resonators, a white light imaging system was added. The reflected signal gets collected by the same objective and is converted to horizontal polarisation by the QWP due to the phase acquired in the reflection. The signal gets separated from the excitation path by being transmitted in the PBS. Two lenses in a 4f configuration are used to creates a conjugate map of the back focal plane (BFP). The first lens creates an image of the sample in the confocal plane (CP), whilst the second lens creates an image of the k-vector distribution. For the measurement of the reflectance, a power meter is placed after the second lens (L2) to register the reflected power as a function of the wavelength the laser is tuned to. For the spatial mapping that allowed for the discrimination of the CBG

supported modes, a CCD camera is placed at the conjugate plane (BFP')

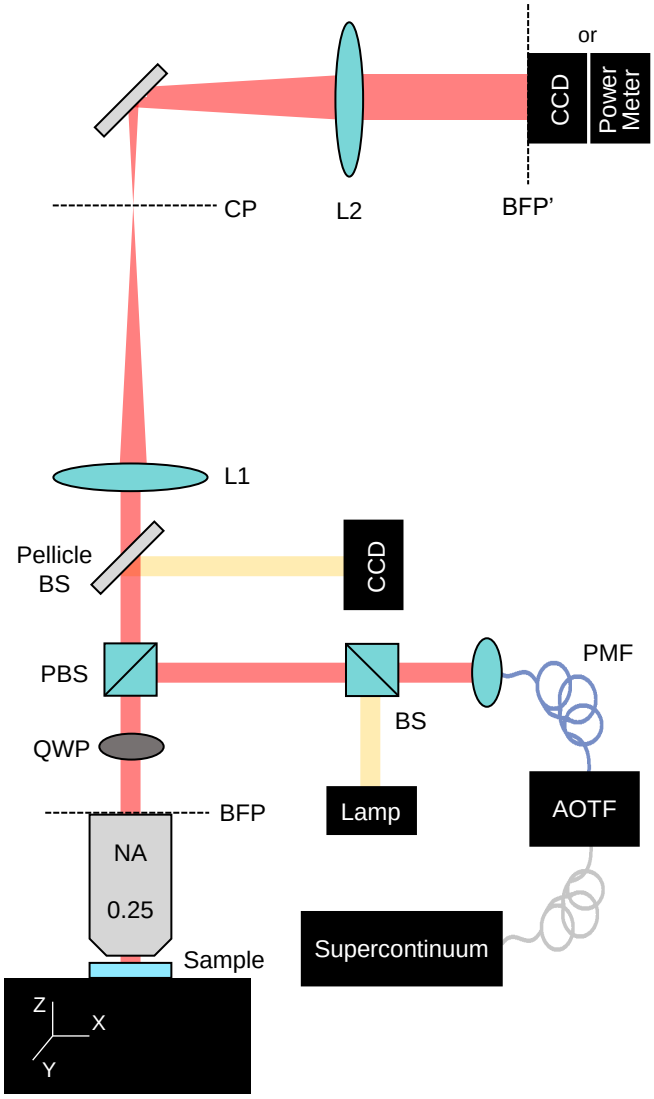

Figure 5.6: Reflectance and Fourier plane microscope.AOTF: acousto-optic tunneable filter, PMF: polarisation mantaining fibre, BS: beamsplitter, PBS: polarising beam splitter, QWP: quarter wave plate, BFP: back focal plane, $L_{1,2}$: conjugate lenses, CP: confocal plane. BFP': conjugate bakc focal plane, CCD: ccd camera.

An example of one of these measurements is shown in figure 5.7 a) The central wavelength of the laser was swept from 580 nm to 700 nm in 1 nm steps recording the

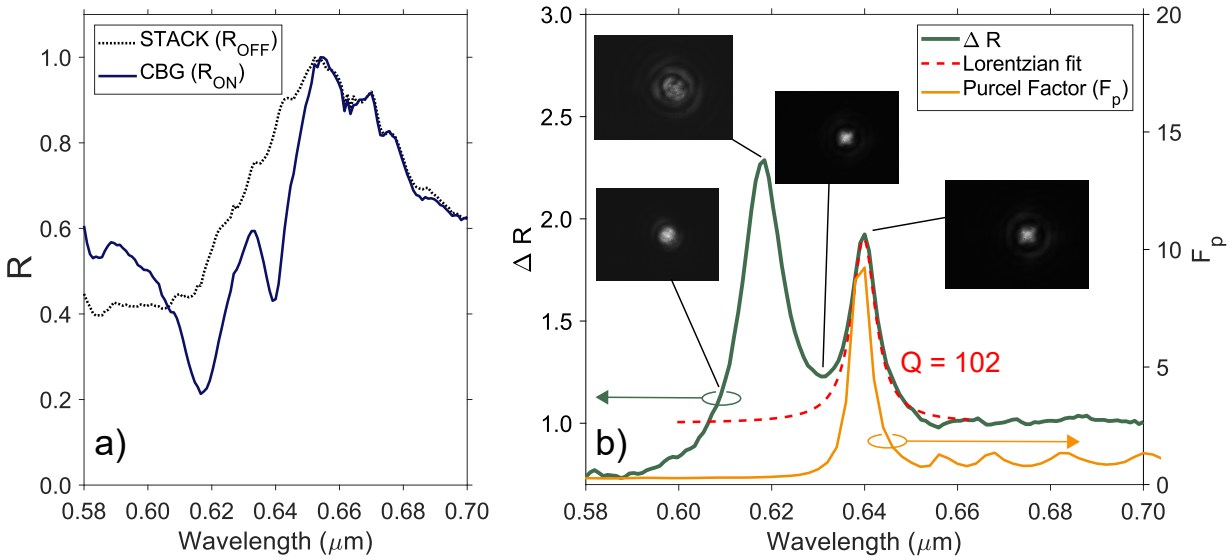

Figure 5.7: Spectral reflectance of a CBG resonator. a) Reflectance of the unpatterned stack (dashed line) and the CBG resonator (solid line). b) Relative change in the reflectance Δ due to the CBG resonator (solid blue line). For comparison, the simulated Purcell factor F_p is shown (right axis, solid yellow line) . A Lorentzian curve is fitted to extract the Q factor of the resonator showing a value of Q =102. Inset images correspond to the intensity profile in the k-space of the reflected beam allowing the discrimination between grating grating guided mode and the central disk

reflected power at each wavelength for the laser focused off the structure to measure the reflectance of the bare stack (R_{OFF}), and on the CBG resonator (R_{ON}). It can be observed that the reflectance of the CBG resonator has two distinctive dips. The other ripples observed in both curves can be explained by interference introduced by the pellicle beam splitter used for imaging. Panel b) in the figure shows the relative change in reflectance (solid blue line) defined as $\Delta R = R_{OFF}/R_{ON}$ (left axis). Plotting of this quantity allows the clear identification of the two peaks produced by the structure. From the FDTD simulations, it is evident that the peak with the longest wavelength correspond to the resonant mode of the central disk. For reference the Purcell factor is plotted (right axis). By fitting a Lorentzian curve to the measured resonance, the Q factor of the resonator can be estimated by $Q = \nu_0/\Delta\nu$ with ν_0 the central frequency of the resonance and $\Delta\nu$ the width at FWHM. For the device plotted here a value of Q =102 was found.

The other peak (around 612 nm) arises from the existence of guided resonances in high-contrast gratings with sub-wavelength periods also called grating modes [109]. Gratings with periods smaller than or comparable to the wavelength of light incident

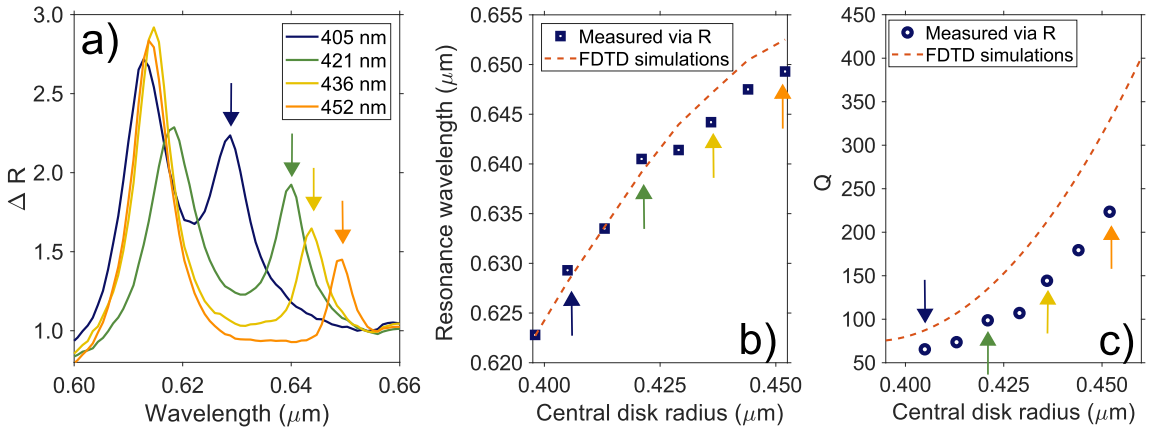

Figure 5.8: Resonance tuning. a) Measured reflectance change ΔR for devices in different rows corresponding to different central disk radii. b) Peak wavelength of the resonance as a function of the diameter of the central disk of the devices. The red dashed line indicates the expected resonance according to FDTD simulations. c) Extracted values of the Q factor of the devices and the expected values according to simulations.

upon them, support in-plane guided modes that get completely confined in the slab of the grating [110]. In summary, grating guided resonances are modes that are confined to the grating slab but that can couple efficiently to radiation modes. An in-depth study of these resonances is out of the scope of this work, however it is worth noting that the wavelength of these resonances depends exclusively on the characteristics of the grating, such as period, duty cycle and depth.

The inset images in figure 5.7 b) are images taken at the conjugate back focal plane at different wavelengths. They display the distribution in the k-space of the reflected light (Fourier plane). These images show that for wavelengths away from any of the resonances, the k-space profile is that of a Gaussian beam. For the grating guided resonance, it is clear that the k-vector distribution gets enlarged and attenuated corresponding to the coupling of the grating mode. However, the k-vector profile for the resonator shows a Gaussian component surrounded by an annular component. These observations are compatible with the simulations of the far-field projections in figure 5.1 d) where the limits of an NA of 0.25 show a partial clipping of the mode. This spatial mapping technique allowed for the discrimination between the two kinds of modes.

Reflectance measurements were carried out for devices in different rows to measure the role of the radius of the central disk r in the resonance central wavelength and Q factor. Figure 5.8 a) shows the change in reflectance ΔR for devices with r values. The

resonances found follow a positive correlation trend r. One thing to notice is that the grating mode does not change wavelength for the devices measured. This behaviour was expected, since the grating features remain constant for the tested devices.

The comparison between simulated and fabricated devices is shown in figure 5.8 b) and c). Panel b) shows the measured resonance central wavelength for devices with different central disk radii along with the trend found through FDTD simulations for comparison. The values measured show a good agreement with the simulations. Similarly, panel c) compares Q factor extracted from the ΔR measurements with the simulations. Although there is an offset between the measured values and the expected values from the simulations, the values follow the same trend. The difference between the simulated and obtained Q factor is mainly due to fabrication imperfections. Rough and angled side walls on the grating rings compromise the Q factor of the resonator. To a lesser extent, the presence of the grating mode can have an effect on the Lorentzian curve fitting used to extract the Q factor.

An alternative way of testing the optical response of CBG resonators is to measure the enhanced PL of an ensemble of emitters in the material of the structure. This method is broadly used in the QD community where the use of high density QD samples is an option [103] [104] [105]. For the case of the NDs used throughout this project, the density of NV^- centres wasn't high enough to use this approach. NDs with a high density of defects are commercially available however, collective material PL could be also accessed also by the use of near stoichiometric SiNx. This is the reason why test structures made for the dosage calibration of the EBL were fabricated using near stoichiometric SiNx, specifically $SiN_{1.62}$ deposited with the recipe labeled SN07 in table 3.1 was used as it exhibited moderate PL. In this sample, four sets of devices with different dose factors were patterned. Each set consisted of variations of trench width between rings w and central disk radius r.

Devices within one of the dose sets were optically tested. CBG resonators designed with a grating period Λ =388 nm, a central disk radius of r =444 nm and trench width values (w) varying from 60 to 100 nm were tested using two methods. First, this sample was put under the tunable laser setup to measure the reflectance of the devices following the same procedure used to characterise the resonators fabricated with N-rich SiNx. Figure 5.9 a) shows the measured change in reflectance ΔR for devices with different w values. The values shown are the average measured w of the actual fabricated devices

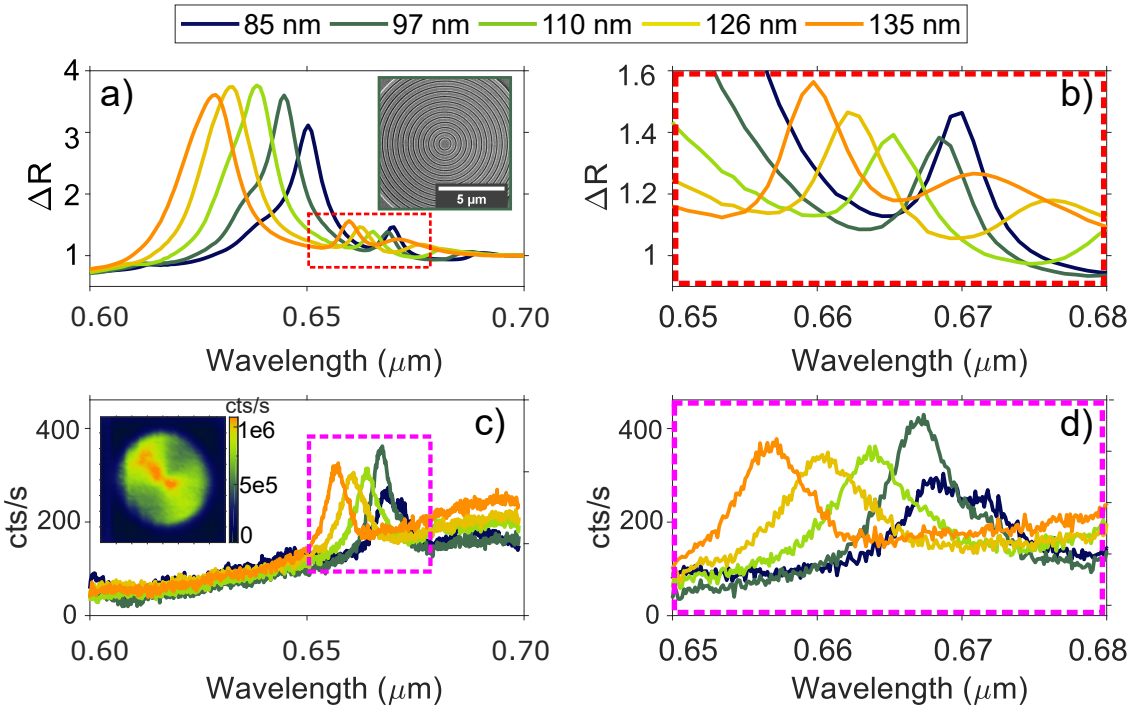

Figure 5.9: Photoluminescence enhancement. a) Measured reflectance change for devices in the calibration sample. This devices have all the same central disk radius and period but different width values for the spacing between rings. It is noticeable that the grating guided resonances shift with the change of duty cycle. The inset is an SEM image of one of the devices under study. b) Zoomed in view of the reflectivity measurements shown in panel a) for the window highlighted with the dashed red rectangle. c) Photoluminescence spectrum of the SiNx material from the CBG resonators after excitation. The photoluminescence couples with the r panel a . c) and d) SEM and photoluminesence confocal scan of one of the device in the calibration sample.

calculated using image analysis of SEM pictures like the one shown in the inset for the device with w =97 nm. In this plot, grating resonances and central disk resonant modes are visible. By imaging the k-space, the grating resonances were distinguished from the resonant modes of the central disk. Both types of resonances shift to larger wavelengths with the increase of w. Panel b) shows a closer look at the central disk resonances for the CBG resonators under examination. It is interesting to note that changing the trench width by keeping the period constant (i.e. changing the duty cycle) not only affects the modes that resonate in the central disk but also changes the grating mode.

The second method used consisted of measuring the PL coming from the centre of the resonators using the confocal microscope described in appendix **??** and used in chapters 3 and 4. To find the centre a confocal scan was done. The scan of one of the

devices (w =97 nm) is shown in the inset of panel c). The PL coming from the resonator is more than ten times brighter than the background noise coming from the exposed SiO_2 reaching a maximum at the centre of the structure. With the laser (532 nm) focused on the centre of the structure, the PL produced by the excited volume in the central disk was collected and analysed using a spectrometer. The spectra is plotted in figure 5.9 c) showing PL enhancement for wavelengths matching the resonances found using reflectance measurements. Panel d) shows a closer look at the peaks. The small discrepancy between the resonance central wavelength measured via reflectance and the one measured through the PL is still under investigation, although the current hypothesis is that this is due to errors in the calibration of the spectrometer used.

5.4 Measuring individual NV^- centres in CBG resonators

The results presented in the previous section demonstrated that the fabricated devices exhibit the expected optical response. The next step was to measure the enhancement of a single NV^- centre coupled to a CBG resonator. To be able to have a good comparison on the effect of the resonator to the NV^- centre emission, examination of NV^- centres without any photonic structure around them was required.

In addition to the fabrication of devices described in section 5.2, arrays of NDs similar to the ones used in chapter 4 were deposited in step 6 of the process and encapsulated like the rest of the ND s in the device. An image taken using dark field microscopy before encapsulation is shown in figure 5.10 panel a). This shows that the number of filled sites (deposition yield) is around 80%. Panel b shows a confocal image of a section of the array (marked with a white dashed line in panel a) using an excitation power of 150 μW. The first thing to notice is that these sites are on average ten times brighter than the ND sites of arrays shown in figure 4.8 where the NDs were uncapped and deposited on bare SiNx substrate, which were then scanned using similar excitation laser powers. This shows that the Au mirror underneath is really helping to recover the emitted photons even when, for the encapsulated NDs, some of the light should be coupling to the slab waveguide mode of the film. The background noise also increased compared to the samples on bare SiNx from dark counts level (around 500 cts/s) to 5000 cts per second, showing there is an extra source of noise. This background noise comes from the interface between the Au film and the SiO_2 spacer. A careful investigation is

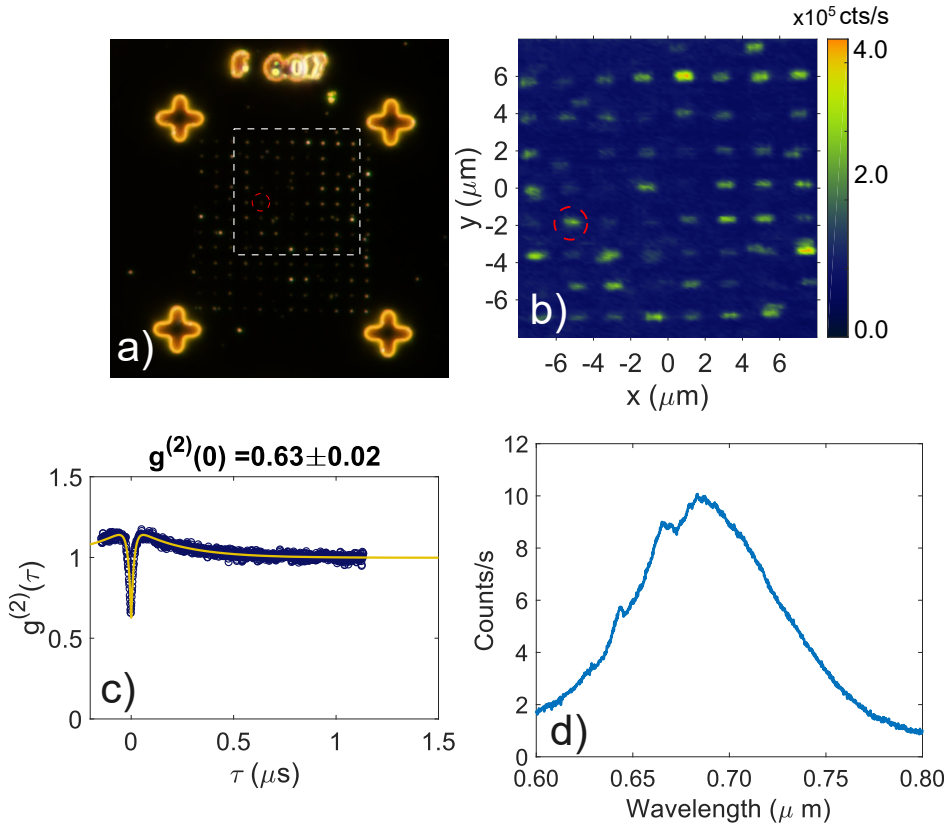

Figure 5.10: ND arrays deposited with no CBG resonator. a) Dark field microscopy image of an array of ND deposited on the substrate stack before encapsulation. b) Confocal scan of a section of the array (marked with a white dashed line) pictured in panel a after encapsulation with SiNx. The elongated shape of the ND sites is an artifact of the image reconstruction method. c) Auto-correlation measurement of the NV^- centre showing a $g^{(2)}(\tau = 0) = 0.63 \pm 0.02$. d) Spectrum of an NV^- centre in a ND encapsulated with SiNx. A clear ZPL peak is observed at $\lambda_{ZPL} = 643.5$nm.The three measurements presented were taken at an excitation power of 150 μW

needed to reduce this source of noise. An auto-correlation measurement was taken on this emitter showing a value of $g^{(2)}(\tau = 0) = 0.63 \pm 0.02$ (figure 5.11c)) most likely because the background noise. The spectrum of this emitter (marked with a red circle) was taken. It shows the typical spectrum of an NV^- centre. It also shows a λ_{ZPL} =643.5 nm which is considerably de-tuned from the usual ZPL value in bulk diamond. The origin of this significant shift is still under investigation. Results presented in [111] show similar shifts observed for NV^- centres in NDs placed on different substrates.

The next step was to look for individual NV^- centres in the fabricated CBG resonators. As many devices were scanned, the fraction of fabricated devices that showed PL from

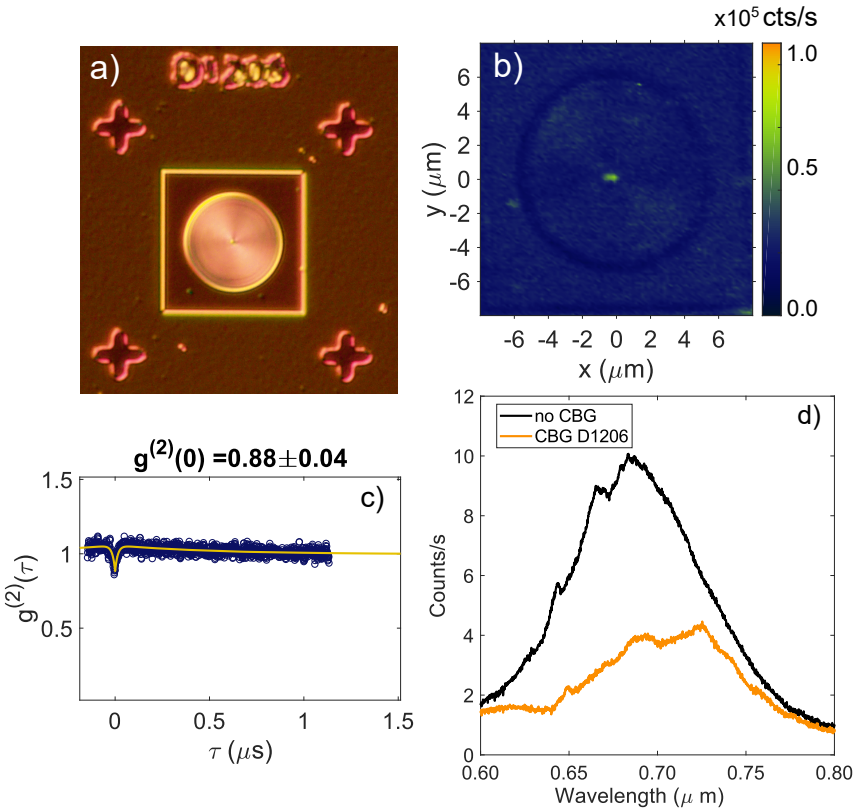

Figure 5.11: Confocal scan and spectrum of an NV^- centre in a CBG resonator. a) Microscope image of the device under study (D1206). b) Confocal scan of device D1206 where the emission of an NV^- centre is coupled to a CBG resonator.c) Auto-correlation measurement of the NV^- centre showing a value of $g^{(2)}(\tau = 0) = 0.88 \pm 0.04$. d) Spectrum measurement of an NV^- centre in a CBG resonator (yellow). The spectrum of a different NV^- centre encapsulated in the SiNx before the etching of the grating structure around it is shown (black) for reference around it. The three measurements presented were taken at an excitation power of 150 μW

an NV^- centre was unexpectedly low. Many of the devices scanned showed bright PL coming from the centre of the resonator but they photo-bleached under examination. One of the only photo-stable features that showed clear signatures of being an NV^- centre was found in device D1206 (figure 5.11 a)). A confocal scan of that device is shown in panel b). The scan was taken just below saturation power (P = 150 μW). The photon count rate of 3e4 counts per second was measured with a background noise of 5000 counts per second, giving a SNR of 6. It is worth noting that the background noise coming from the SiNx resonator is comparable with the noise coming from the exposed SiO_2 spacer in contrast with the confocal scan showed in the inset of figure 5.9 where the PL coming from the near stoichiometric $SiN_{1.62}$ is orders of magnitude higher than

the exposed SiO_2. This confirmed that the origin of this background noise was coming from the interface between the PECVD SiO_2 film and the Au film. The auto-correlation measurement (panel c)) for this emitter shows $g^{(2)}(\tau = 0) = 0.88 \pm 0.04$.

The spectrum coming from the NV^- centre in the device is presented in figure 5.11 d). While the spectrum exhibits the general shape of NV^- centre emission, it does not show a clear enhancement of the NV fluorescence. On the contrary, it shows a significant generalised attenuation of the PL (roughly a factor of 1.8), although this could be a combined effect of the scattering of the structure and a poor collection efficiency due to the orientation of the NV^- centre.

The performance of the devices was thoroughly studied in previous sections and the results show that the resonators are well fabricated and can enhance PL coming from the centre of the central disk. Therefore, there must be another reason why The fluorescence of the NV^- centre is not being enhanced. Upon closer analysis of the confocal scan, it was found that there was a displacement from the centre of the resonator on this and many other devices. Figure 5.12 a) shows the same confocal scan of the device D1206 but with a reticule overlaid. The reticule was based on the noticeable limits of the CBG resonator. In this image it is clear that the NV emission comes from the edges of the central disk. Displacement from the centre of the disk is critical for the enhancement of the PL. Figure 5.12 b) Shows FDTD simulations of the Purcell factor at 637 nm for an electrical dipole (aligned with the x-axis) at different positions in the central disk. The limits of the central disk are highlighted with a white circle. As expected, it is clear that the enhancement is critically dependent on the position, and that the displacement observed for the NV centre explains the lack of spectral shaping.

Another factor contributing to the poor collection was the mismatch between the the 3-lobe far-field mode shown in figure 5.1d) and the mode of a single mode fibre (SMF). With this in mind the confocal setup was modified to replace the single-mode fibre with a pinhole of aperture to eliminate the filtering the relatively small NV of the SMF was adding. After the light is filtered by the pinhole a set of lenses couple the signal to a multi-mode fibre (MMF) as shown in the schematic in figure 5.13 a). The auto-correlation measurement of the emitter in device D1206 was repeated and is shown in panel b). The inclusion of the pinhole in the setup has improved the SNR moving the value of $g^{(2)}(\tau = 0)$ to 0.70 ± 0.03. The new configuration also improved the lateral resolution. The confocal scan of the same device (D1206) is shown in panel c). The resolution allows

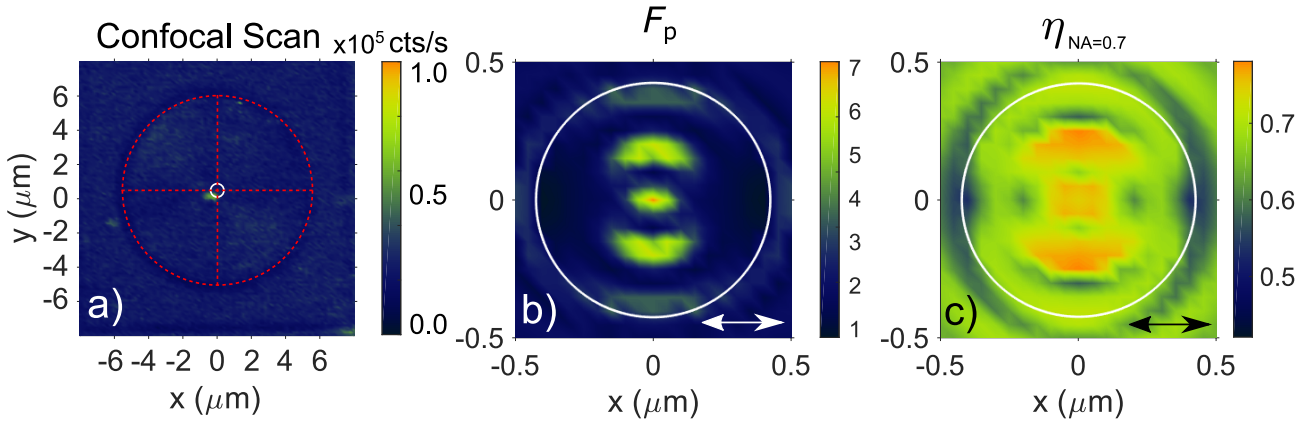

Figure 5.12: Position dependent coupling. a) The confocal scan of device D1206 is overlayed with a cross-hair (red dashed line) created from the noticeable resonators total circumference. A white circle marks the limits of the central disk. It shows an evident displacement from the centre. b) Simulated Purcell factor for a dipole oriented with the x-axis localised at different points within the resonators central disk marked with a white circle. c) Simulated Collection efficiency for a dipole at different positions within the central disk. The collection efficiency is calculated for a collection lens with NA = 0.7 and a dipole parallel to the structure plane and aligned with the x-axis.

to resolve the rings of the structure but more importantly shows very clear evidence that the emitter is not positioned at the centre of the resonator. More evidence and a quantification of the displacement could be done with SEM microscopy however this would make the device useless after characterisation since, as explained before, SEM imaging introduces plenty of defects on the materials that affects the SNR of the NV emission. Atomic force microscopy could be a good alternative for this and is part of the planned future work of this project.

The displacement observed could have been produced by a poor overlay between lithography processes, although, this hypothesis needs to be explored carefully since there is evidence that some devices (like the one shown in figure 5.5 d-f), exhibit an accurate overlay since the NDs are clearly positioned under the centre of the central disk.

Another possible contribution to the poor coupling into the resonators mode could be the orientation of the emitter. While CBG resonators are insensitive to rotations around the z-axis due to the circular symmetry, variations on the polar angle (formed between the N-V axis and the z-axis) can affect the coupling to the cavities. To confirm that this is the case, polarisation measurements could be performed as detailed in chapter 4.

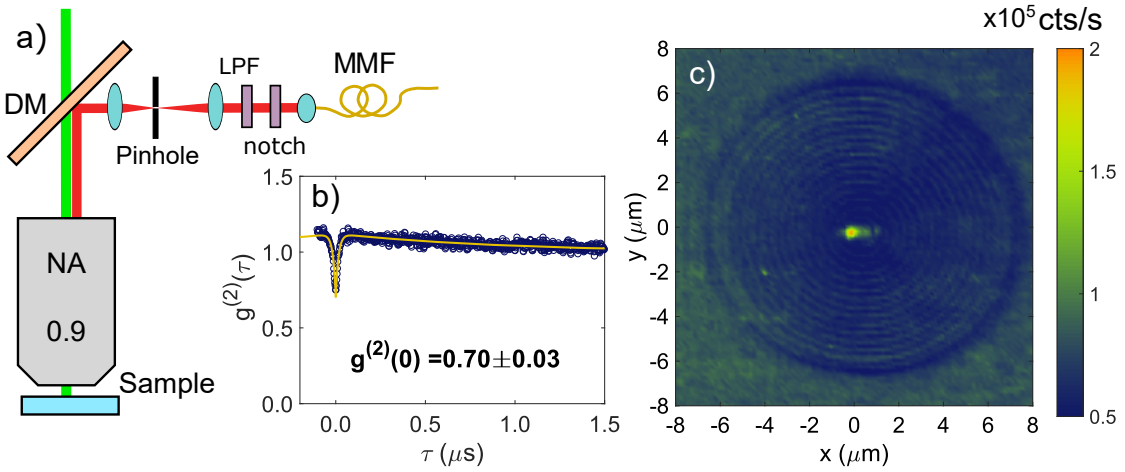

Figure 5.13: a) Schematic showing the changes made to the fluorescence confocal microscope setup to increase the SNR. DM: dichroic mirror, MMF: Multi-mode fibre. LPF: long-pass filter. b) Auto-correlation measurement of the NV using the modified configuration showing a $g^{(2)}(\tau = 0) = 0.70 \mp 0.03$. c) Confocal scan of device D1206 under the modified setup. An improvement on the resolution makes evident that the emitter is not centered in the central disk.

Additional simulations are needed to understand how more realistic NV^- centres with an arbitrary orientation couple to the resonators and what changes in the design are needed to maximise the coupling efficiency. Some interesting work in this direction has been explored by Zheng and co workers in [112].

Furthermore, special attention needs to be given to the low number of devices that were found to have single NV^- centres. The main factor contributing to this is the deposition yield. From the results of chapter 4, it was observed that the yield deposition over large areas was strongly affected by the formation of micro droplets on the deposition template surface. This means that the ND deposition yield was not equal across all the devices.

It is clear from these results that there are many factors in both the design and fabrication process that require further work. However, the work outlined in this chapter has proven that CBG resonators can be fabricated that perform very closely to what was expected of them from the simulations. These promising results, along with the improvements planned for the future work of this project, show great potential for the final design of these devices.

CHAPTER 6

CONCLUSIONS AND FUTURE WORK

The overarching purpose of this thesis was to demonstrate the first steps towards building scalable and efficient spin-photon interfaces, primarily around an integrated photonics platform.

In chapter 2, the need for a different approach for building devices that interface solid state spin defects with photonic cavities was justified. The different options and approaches that are currently being used by the community were reviewed, and this in turn motivated the need for an approach that is scalable. It was suggested that the integration of nanoparticles hosting spin defects with foundry fabricated devices photonics was a valid approach that was worth exploring. For their excellent spin properties at room temperature, it was established that NV^- centres in nanodiamonds (NDs) were the best spin defect to test this approach, hence a quick review of the theory behind the physical system and the techniques used to characterise its spin and optical properties were presented.

In chapter 3 it was shown that N-rich SiNx is a good material to implement this integration since it exhibits at least 30 times less photoluminescence (PL) under laser excitation than its stoichiometric counterpart used in common foundries. The work done in this chapter provided an insight into the origin of the PL and hinted the path that needs to be taken to suppress the PL even more. It was also demonstrated that the reduction was sufficient to detect and manipulate single spins of NV^- centre encapsulated within

this material.While plenty of studies have been published on the PL of SiNx films with different material compositions, there are not many studies that explicitly aim to reduce the PL for integration with quantum emitters making it challenging to compare the results obtained here. However, it is clear there is interest in the community to be able to have integrated photonics in the visible for low light applications where the intrinsic PL would be detrimental. This is shown by foundries like IMEC offering a low intrinsic PL photonics platforms.

Chapter 4 presented one of the techniques available to achieve spatial control over the defects and laid out why this this one was chosen from the point of view of scalability. It was clear that the lithographic deposition method used has valuable benefits in terms of controlling the probability of having exactly one NV^- centre per site. This does however come with some drawbacks, such as the lack of control of the orientation of the particles. Techniques to determine the orientation of NV^- centres and ideas to use this information to identify single defects were explored.There is room for improvement for this deposition technique. As mentioned previously, using an ultrasonic nebuliser to have an even coating of the ND suspension as used in [11] can increase substantially the deposition yield. The use of a two step lithography process like the one shown in [91] would also improve the quality of the deposition reducing the number of NDs that re-deposit after the mask lift-off.

Finally, in chapter 5 the results of the previous chapters were compiled to fabricate circular Bragg grating resonators around the emitters. The optical performance of the resonators was demonstrated to have a very good agreement with the simulation simulated performance. Whilst enhancement of the emission of individual NV^- centres was not observed, it is evident that the unsatisfactory results are due to technical issues that need to be fixed, rather than there being a fundamental flaw in the design. While a this work hasn't showed a fully functional device where the enhance collection efficiency is demonstrated, is interesting to note that by the sole use of the Au backreflector, the amount of photons per second detected from NV^- centres on this substrate already show an order of magnitude increase compared to the ones shown in chapter 3. This means that a sucessfull fabrication of the CBG resonators proposed here could easily exceed the collection efficiency enhancement reporte in the only other work published on NV^- centres in CBG resonators [24] that shows a 15-fold enhancement of the collected light.

When reviewing whether the purpose of this project was achieved, it is important to

review the scalability and efficiency of the devices made. Upon fixing specific technical issues and attaining orientation control of the spin defects, the scalability of this approach is clear. Lithographic deposition of nanoparticles, encapsulation and patterning are processes that could be implemented in silicon nitride foundries. The work required to build one or thousands of these devices would be the same for all the steps of the fabrication process.

When discussing the efficiency of the devices the definition of efficiency must be clarified, as there are multiple ways as to whether these interfaces can be considered efficient.

If the efficiency solely refers to the fraction of emitted photons that are collected, i.e. collection efficiency, then FDTD simulations have shown that structures like the CBG resonators are capable of achieving efficient interfaces (> 80% at the ZPL wavelength for an ideally oriented NV^- centre) meaning that these device could exhibit a better extraction efficiency than the devices used in state-of-the-art entanglement distribution experiments [5] where collection efficiencies of 10% are reported

On the other hand, if efficiency refers to the rate at which entanglement between two of this systems can be achieve, then the approach exposed here has some important challenges that need to be addressed since this success rate depends on the indistinguishability of the emitted photons. It is specially challenging if the spins used are from NV^- centres since the optical dephasing created by charges in the different interfaces between different materials would affect dramatically the indistinguishability of the emitted photons. Fortunately, there are plenty of routes to overcome these challenges; surface charge passivation and ultra-small volume cavities are promising routes for addressing these issues.

Furthermore, as this approach is not exclusively tied to the use of NV^- centres, opting for defects without a permanent electric dipole moment, like tin-vancancy (SnV) centres in diamond, would improve the resilience to charge fluctuations. In fact, any solid state spin defect that has been studied for quantum information purposes can be used in this approach provided that nanoparticles of the host material can be made. Silicon Nitride would work for many other defects given that it has a large transparency window making it particularly attractive to switch to defects with emission in the infrared, where the absences of material PL would improve the results.

6.1 Challenges and future work

Throughout this thesis numerous opportunities to improve the realisation of the devices have been identified. A selective list of improvements and future work is presented below.

- Even when suppression of the inherent PL of SiNx was found in chapter 3, it was clear from some measurements that the PL was not negligible and future work is needed to improve this if SiNx is to be used. From the results of chapter 3 it is believed that the origin of the remaining PL is the inter-band defects. It is worth exploring whether deposition at lower temperatures or post-deposition annealing in H_2 gas ambient would passivate the inter-band defects, and thereby suppressing the remaining PL observed.

- There is a need for the improvement on the deposition methods presented in chapter 4. Improvements that guarantee near-unity deposition yield over large areas are needed. The way in which the ND suspension was deposited caused an stochastic formation of droplets leading to an uneven filling yield of the filled apertures. Approaches like the one showed in reference [113] where capillary forces are used to achieve 100% yield assembly over centimeter-scale areas can represent a big improvement for the device fabrication yield.

- The fast discrimination of single emitters using only the correlation between brightness, polarisation contrast and fluorescence lifetime is a technique that could add value to the project. Further work is needed to determine the validity and confidence boundaries of this idea but the amount of time it could potentially save is worth it.

- In terms of the fabrication of the devices, there are a number of improvements to be made. Firstly, the most immediate fabrication issues to resolve is the failed overlay of the processes on the devices which led to the offset of the NDs. Future work will require explore mechanisms to ensure an overlays with higher accuracy. Additionally, some work is needed in characterising the sidewall angle and roughness of the structures etched on the SiNx film. Fine tuning of the etching recipes could lead to better quality etches and an increment in the Q factors observed.

- The design of the CBG resonators shown in chapter 5 has been relatively simple, in the sense that all the simulations have assumed an in-plane orientation of just

one dipole. This approach is enough for emitters like InGaAs quantum dots where the emission come from a single dipole that is always in-plane. For emitters like the NV^- centre, the design of the structures can be optimised for a more realistic model to produce a far-field profile that matches better a single-mode optical fibres. A study based on this ideas was published by Zheng and co-authors [112] where a period modulation (chirp) was introduced in the design to optimise the extraction from a more realistic NV^- centre.

- Once devices show the desired performance at room temperature, the aim is to test them at cryogenic temperatures to measure line widths of extracted photons in the zero phonon line.

- While the use of CBG resonators had better prospects to show the success of the approach studied here, designing photonic cavities that release photons into waveguides has been one of the main goals of this project. This would allow for heralded entanglement to be performed between a number of spin defects effectively limited by the constraints of lithographic processes representing a massive improvement to what has been achieved with solid state spin systems to date. With that objective, initial steps have been taken to include NDs with IMEC-Biopix photonic circuits.

There is a long but promising road ahead for this project. While this thesis has shown the initial steps to obtain efficient (with both connotations) spin-photon interfaces, ideas to overcome the challenges are vast and the prospective future applications are diverse and compelling.

BIBLIOGRAPHY

[1] N Gisin and R Thew. "Quantum communication". *Nature photonics* 1.3 (2007), pp. 165–171.

[2] CL Degen, F Reinhard, and P Cappellaro. "Quantum sensing". *Reviews of modern physics* 89.3 (2017), p. 035002.

[3] PW Shor. "Algorithms for quantum computation: discrete logarithms and factoring". *Proceedings 35th annual symposium on foundations of computer science*. Ieee. 1994, pp. 124–134.

[4] LK Grover. "A fast quantum mechanical algorithm for database search". *Proceedings of the twenty-eighth annual ACM symposium on Theory of computing*. 1996, pp. 212–219.

[5] M Pompili et al. "Realization of a multi-node quantum network of remote solid-state qubits". 2.April (2021), pp. 259–264. arXiv: 2102.04471.

[6] B Hensen et al. "Loophole-free Bell inequality violation using electron spins separated by 1.3 kilometres". *Nature* 526.7575 (2015), pp. 682–686.

[7] MW Doherty, NB Manson, P Delaney, F Jelezko, J Wrachtrup, and LC Hollenberg. "The nitrogen-vacancy colour centre in diamond". *Physics Reports* 528.1 (2013), pp. 1–45. arXiv: 1302.3288.

[8] A Gali, M Fyta, and E Kaxiras. "Ab initio supercell calculations on nitrogen-vacancy center in diamond: Electronic structure and hyperfine tensors". *Physical Review B* 77.15 (2008), p. 155206.

[9] G Balasubramanian et al. "Nanoscale imaging magnetometry with diamond spins under ambient conditions". *Nature* 455.7213 (2008), pp. 648–651.

[10] C Stephen et al. "Deep three-dimensional solid-state qubit arrays with long-lived spin coherence". *Physical Review Applied* 12.6 (2019), p. 064005.

[11] B Wood et al. “Long spin coherence times of nitrogen vacancy centers in milled nanodiamonds”. *Physical Review B* 105.20 (2022), p. 205401.

[12] H Bernien et al. “Heralded entanglement between solid-state qubits separated by three metres”. *Nature* 497.7447 (2013), pp. 86–90.

[13] TD Ladd, F Jelezko, R Laflamme, Y Nakamura, C Monroe, and JL O’Brien. “Quantum computers”. *Nature* 464.7285 (2010), pp. 45–53.

[14] F Grazioso, BR Patton, P Delaney, ML Markham, DJ Twitchen, and JM Smith. “Measurement of the full stress tensor in a crystal using photoluminescence from point defects: The example of nitrogen vacancy centers in diamond”. *Applied Physics Letters* 103.10 (2013).

[15] E Togan et al. “Quantum entanglement between an optical photon and a solid-state spin qubit”. *Nature* 466.7307 (2010), pp. 730–734.

[16] CW Chou, H De Riedmatten, D Felinto, SV Polyakov, SJ Van Enk, and HJ Kimble. “Measurement-induced entanglement for excitation stored in remote atomic ensembles”. *Nature* 438.7069 (2005), pp. 828–832.

[17] SD Barrett and P Kok. “Efficient high-fidelity quantum computation using matter qubits and linear optics”. *Physical Review A* 71.6 (2005), p. 060310.

[18] D Riedel et al. “Deterministic enhancement of coherent photon generation from a nitrogen-vacancy center in ultrapure diamond”. *Physical Review X* 7.3 (2017), p. 031040.

[19] X Ding et al. “On-demand single photons with high extraction efficiency and near-unity indistinguishability from a resonantly driven quantum dot in a micropillar”. *Physical review letters* 116.2 (2016), p. 020401.

[20] J Iles-Smith, DP McCutcheon, A Nazir, and J Mørk. “Phonon scattering inhibits simultaneous near-unity efficiency and indistinguishability in semiconductor single-photon sources”. *Nature Photonics* 11.8 (2017), pp. 521–526.

[21] JA Smith, C Clear, KC Balram, DP McCutcheon, and JG Rarity. “Nitrogen-Vacancy Center Coupled to an Ultrasmall-Mode-Volume Cavity: A High-Efficiency Source of Indistinguishable Photons at 200 K”. *Physical Review Applied* 15.3 (2021), p. 1.

[22] J Hadden et al. “Strongly enhanced photon collection from diamond defect centers under microfabricated integrated solid immersion lenses”. *Applied Physics Letters* 97.24 (2010), p. 241901.

[23] TM Babinec et al. “A diamond nanowire single-photon source”. *Nature nanotechnology* 5.3 (2010), pp. 195–199.

[24] L Li et al. “Efficient photon collection from a nitrogen vacancy center in a circular bullseye grating”. *Nano Letters* 15.3 (2015), pp. 1493–1497.

[25] A Faraon, PE Barclay, C Santori, KMC Fu, and RG Beausoleil. “Resonant enhancement of the zero-phonon emission from a colour centre in a diamond cavity”. *Nature Photonics* 5.5 (2011), pp. 301–305.

[26] BJM Hausmann et al. “Coupling of NV centers to photonic crystal nanobeams in diamond”. *Nano letters* 13.12 (2013), pp. 5791–5796.

[27] L Li et al. “Coherent spin control of a nanocavity-enhanced qubit in diamond”. *Nature communications* 6.1 (2015), pp. 1–7.

[28] D Englund et al. “Deterministic coupling of a single nitrogen vacancy center to a photonic crystal cavity”. *Nano letters* 10.10 (2010), pp. 3922–3926.

[29] A Faraon, C Santori, Z Huang, VM Acosta, and RG Beausoleil. “Coupling of nitrogen-vacancy centers to photonic crystal cavities in monocrystalline diamond”. *Physical Review Letters* 109.3 (2012), pp. 2–6. arXiv: 1202.0806.

[30] F Neugart et al. “Dynamics of diamond nanoparticles in solution and cells”. *Nano letters* 7.12 (2007), pp. 3588–3591.

[31] A Laraoui, JS Hodges, and CA Meriles. “Nitrogen-vacancy-assisted magnetometry of paramagnetic centers in an individual diamond nanocrystal”. *Nano letters* 12.7 (2012), pp. 3477–3482.

[32] A Albrecht, A Retzker, and MB Plenio. “Testing quantum gravity by nanodiamond interferometry with nitrogen-vacancy centers”. *Physical Review A* 90.3 (2014), p. 033834.

[33] S Bose et al. “Spin entanglement witness for quantum gravity”. *Physical review letters* 119.24 (2017), p. 240401.

[34] B Naydenov et al. “Dynamical decoupling of a single-electron spin at room temperature”. *Physical Review B* 83.8 (2011), p. 081201.

[35] J Tisler et al. “Fluorescence and spin properties of defects in single digit nanodiamonds”. *ACS nano* 3.7 (2009), pp. 1959–1965.

[36] ME Trusheim et al. “Scalable fabrication of high purity diamond nanocrystals with long-spin-coherence nitrogen vacancy centers”. *Nano letters* 14.1 (2014), pp. 32–36.

[37] HS Knowles, DM Kara, and M Atatüre. “Observing bulk diamond spin coherence in high-purity nanodiamonds”. *Nature Materials* 13.1 (2014), pp. 21–25.

[38] R Albrecht, A Bommer, C Deutsch, J Reichel, and C Becher. “Coupling of a Single Nitrogen-Vacancy Center in Diamond to a Fiber-Based Microcavity”. *Physical Review Letters* 110.24 (2013), p. 243602. arXiv: 1303.7418.

[39] F Ortiz-Huerta et al. “Fabrication of hybrid Fabry-Pérot microcavity using two-photon lithography for single-photon sources”. *Optics Express* 26.25 (2018), pp. 33245–33252.

[40] P Dolan et al. “Robust, tunable, and high purity triggered single photon source at room temperature using a nitrogen-vacancy defect in diamond in an open microcavity”. *Optics express* 26.6 (2018), pp. 7056–7065.

[41] J Wolters et al. “Enhancement of the zero phonon line emission from a single nitrogen vacancy center in a nanodiamond via coupling to a photonic crystal cavity”. *Applied Physics Letters* 97.14 (2010), pp. 2008–2011.

[42] C Santori, P Barclay, KC Fu, R Beausoleil, S Spillane, and M Fisch. “Nanophotonics for quantum optics using nitrogen-vacancy centers in diamond”. *Nanotechnology* 21.27 (2010), p. 274008.

[43] C Kurtsiefer, S Mayer, P Zarda, and H Weinfurter. “Stable solid-state source of single photons”. *Physical Review Letters* 85.2 (2000), pp. 290–293.

[44] RH Brown and RQ Twiss. “Correlation between photons in two coherent beams of light”. *Nature* 177.4497 (1956), pp. 27–29.

[45] J Smith, J Monroy-Ruz, JG Rarity, and KC Balram. “Single photon emission and single spin coherence of a nitrogen vacancy center encapsulated in silicon nitride”. *Applied Physics Letters* 116.13 (2020). arXiv: 1909.09383.

[46] JT Choy et al. “Integrated TiO_2 resonators for visible photonics”. *Optics Letters* 37.4 (2012), p. 539. arXiv: 1111.3545.

[47] A Butcher et al. “High- Q Nanophotonic Resonators on Diamond Membranes using Templated Atomic Layer Deposition of TiO2”. *Nano Letters* 20.6 (2020), pp. 4603–4609. arXiv: 2004.03532.

[48] K Chung, TJ Karle, C Wang, M Lončar, and S Tomljenovic-Hanic. “Hybrid nanodiamond and titanium dioxide nanobeam cavity design”. *Optical Materials Express* 7.3 (2017), p. 785.

[49] B Dong et al. “Aluminum nitride on insulator (AlNOI) platform for mid-infrared photonics”. *Optics Letters* 44.1 (2019), p. 73.

[50] C Xiong, WHP Pernice, X Sun, C Schuck, KY Fong, and HX Tang. “Aluminum nitride as a new material for chip-scale optomechanics and nonlinear optics”. *New Journal of Physics* 14 (2012). arXiv: 1210.0975.

[51] WH Pernice, C Xiong, C Schuck, and HX Tang. “High-Q aluminum nitride photonic crystal nanobeam cavities”. *Applied Physics Letters* 100.9 (2012).

[52] WJ Liu, SJ Wu, CM Chen, YC Lai, and CH Chuang. “Microstructural evolution and formation of highly c-axis-oriented aluminum nitride films by reactively magnetron sputtering deposition”. *Journal of Crystal Growth* 276.3-4 (2005), pp. 525–533.

[53] Y Fujii, S Yoshida, S Misawa, S Maekawa, and T Sakudo. “Nonlinear optical susceptibilities of AlN film”. *Applied Physics Letters* 31.12 (1977), pp. 815–816.

[54] TJ Lu et al. “Aluminum nitride integrated photonics platform for the ultraviolet to visible spectrum”. *Optics Express* 26.9 (2018), p. 11147. arXiv: 1704.07292.

[55] N Gruhler et al. “Diamond on aluminum nitride as a platform for integrated photonic circuits”. *Physica Status Solidi (A) Applications and Materials Science* 213.8 (2016), pp. 2075–2080.

[56] TJ Lu et al. “Bright High-Purity Quantum Emitters in Aluminum Nitride Integrated Photonics”. *ACS Photonics* 7.10 (2020), pp. 2650–2657. arXiv: 2006.16276.

[57] A Sharma, M Goswami, and BR Singh. “Optimization and Stress Analysis of Local Oxidation of Silicon (LOCOS) Process for Isolation”. *2013 International Conference on Communication Systems and Network Technologies*. IEEE, 2013, pp. 736–740.

[58] CG Roeloffzen et al. “Low-loss si3n4 triplex optical waveguides: Technology and applications overview”. *IEEE Journal of Selected Topics in Quantum Electronics* 24.4 (2018).

[59] A Dhakal, P Wuytens, A Raza, N Le Thomas, and R Baets. “Silicon Nitride Background in Nanophotonic Waveguide Enhanced Raman Spectroscopy”. *Materials* 10.2 (2017), p. 140.

[60] SL Mouradian et al. “Scalable integration of long-lived quantum memories into a photonic circuit”. *Physical Review X* 5.3 (2015). arXiv: 1409.7965.

[61] NM Park, TS Kim, and SJ Park. “Band gap engineering of amorphous silicon quantum dots for light-emitting diodes”. *Applied Physics Letters* 78.17 (2001), pp. 2575–2577.

[62] TY Kim et al. “Quantum confinement effect of silicon nanocrystals in situ grown in silicon nitride films”. *Applied Physics Letters* 85.22 (2004), pp. 5355–5357.

[63] N Mott, JM Marshall, SR Elliott, and EA Davis. “Journal of Physics C : Solid State Physics Related content States in the gap in non-crystalline semiconductors States in the gap in non-crystalline semiconductors”. *J. Phys. C: Solid State Phys* (1980).

[64] DJ Dunstan and F Boulitrop. “Photoluminescence in hydrogenated amorphous silicon”. *Physical Review B* 30.10 (1984), pp. 5945–5957.

[65] M Anutgan, T Anutgan, I Atilgan, and B Katircioglu. “Photoluminescence analyses of hydrogenated amorphous silicon nitride thin films”. *Journal of Luminescence* 131.7 (2011), pp. 1305–1311.

[66] F Boulitrop and D Dunstant. “Phonon interactions in the tail states of a-Si:H”. *Physical Review B* 28.10 (1983).

[67] J Kistner, X Chen, Y Weng, HP Strunk, MB Schubert, and JH Werner. “Photoluminescence from silicon nitride—no quantum effect”. *Journal of Applied Physics* 110.2 (2011), p. 023520.

[68] J Robertson. “Defects and hydrogen in amorphous silicon nitride”. *Philosophical Magazine B: Physics of Condensed Matter; Statistical Mechanics, Electronic, Optical and Magnetic Properties* 69.2 (1994), pp. 307–326.

[69] J Kanicki and WL Warren. “Defects in amorphous hydrogenated silicon nitride films”. *Journal of Non-Crystalline Solids* 164-166.PART 2 (1993), pp. 1055–1060.

[70] GN Parsons, JH Souk, and J Batey. “Low hydrogen content stoichiometric silicon nitride films deposited by plasma-enhanced chemical vapor deposition”. *Journal of Applied Physics* 70.3 (1991), pp. 1553–1560.

[71] F Giorgis, C Vinegoni, and L Pavesi. “Optical absorption and photoluminescence properties of films deposited by plasma-enhanced CVD”. *Physical Review B - Condensed Matter and Materials Physics* 61.7 (2000), pp. 4693–4698.

[72] YQ Wang, YG Wang, L Cao, and ZX Cao. “High-efficiency visible photoluminescence from amorphous silicon nanoparticles embedded in silicon nitride”. *Applied Physics Letters* 83.17 (2003), pp. 3474–3476.

[73] A Gorin, A Jaouad, E Grondin, V Aimez, and P Charette. “Fabrication of silicon nitride waveguides for visible-light using PECVD: a study of the effect of plasma frequency on optical properties”. *Optics Express* 16.18 (2008), p. 13509.

[74] EP Van de Ven, IW Connick, and AS Harrus. “Advantages of dual frequency PECVD for deposition of ILD and passivation films”. *Seventh International IEEE Conference on VLSI Multilevel Interconnection*. IEEE. 1990, pp. 194–201.

[75] AS Ferlauto et al. “Analytical model for the optical functions of amorphous semiconductors from the near-infrared to ultraviolet: Applications in thin film photovoltaics”. *Journal of Applied Physics* 92.5 (2002), pp. 2424–2436.

[76] S John, C Soukoulis, MH Cohen, and EN Economou. “Theory of electron band tails and the urbach optical-absorption edge”. *Physical Review Letters* 57.14 (1986), pp. 1777–1780.

[77] J Tauc, R Grigorovici, and A Vancu. “Optical properties and electronic structure of amorphous germanium”. *physica status solidi (b)* 15.2 (1966), pp. 627–637.

[78] E Bustarret, M Bensouda, MC Habrard, JC Bruyère, S Poulin, and SC Gujrathi. “Configurational statistics in a - Si x N y H z alloys: A quantitative bonding analysis”. *Physical Review B* 38.12 (1988), pp. 8171–8184.

[79] A Senichev et al. “Room-temperature single-photon emitters in silicon nitride”. *Science Advances* 7.50 (2021), eabj0627.

[80] P Michler. *Single semiconductor quantum dots*. Vol. 28. Springer, 2009.

[81] DM Toyli, CD Weis, GD Fuchs, T Schenkel, and DD Awschalom. “Chip-scale nanofabrication of single spins and spin arrays in diamond”. *Nano Letters* 10.8 (2010), pp. 3168–3172.

[82] S Lagomarsino et al. “Optical properties of silicon-vacancy color centers in diamond created by ion implantation and post-annealing”. *Diamond and Related Materials* 84.March (2018), pp. 196–203.

[83] T Iwasaki et al. “Germanium-Vacancy Single Color Centers in Diamond”. *Scientific Reports* 5 (2015), pp. 1–7.

[84] T Iwasaki et al. “Tin-Vacancy Quantum Emitters in Diamond”. *Physical Review Letters* 119.25 (2017), pp. 1–6. arXiv: 1708.03576.

[85] YC Chen et al. “Laser writing of coherent colour centres in diamond”. *Nature Photonics* 11.2 (2017), pp. 77–80.

[86] X Gao et al. “Femtosecond Laser Writing of Spin Defects in Hexagonal Boron Nitride”. *ACS Photonics* 8.4 (2021), pp. 994–1000. arXiv: 2012.03207.

[87] E Ampem-Lassen et al. “Nano-manipulation of diamond-based single photon sources”. *Optics Express* 17.14 (2009), p. 11287.

[88] AW Schell, G Kewes, T Schröder, J Wolters, T Aichele, and O Benson. “A scanning probe-based pick-and-place procedure for assembly of integrated quantum optical hybrid devices”. *Review of Scientific Instruments* 82.7 (2011), pp. 4–7. arXiv: 1107.0612.

[89] T Van Der Sar et al. “Nanopositioning of a diamond nanocrystal containing a single nitrogen-vacancy defect center”. *Applied Physics Letters* 94.17 (2009), pp. 10–13.

[90] M Geiselmann, R Marty, J Renger, FJ García de Abajo, and R Quidant. “Deterministic Optical-Near-Field-Assisted Positioning of Nitrogen-Vacancy Centers”. *Nano Letters* 14.3 (2014), pp. 1520–1525.

[91] O Shimoni et al. “Development of a templated approach to fabricate diamond patterns on various substrates”. *ACS Applied Materials and Interfaces* 6.11 (2014), pp. 8894–8902.

[92] AH Heffernan, AD Greentree, and BC Gibson. “Nanodiamond arrays on glass for quantification and fluorescence characterisation”. *Scientific Reports* 7.1 (2017), pp. 1–8. arXiv: 1705.03610.

[93] M Kianinia et al. “Robust, directed assembly of fluorescent nanodiamonds”. *Nanoscale* 8.42 (2016), pp. 18032–18037.

[94] C Bradac et al. “Observation and control of blinking nitrogen-vacancy centres in discrete nanodiamonds”. *Nature Nanotechnology* 5.5 (2010), pp. 345–349.

[95] D Mampallil and HB Eral. “A review on suppression and utilization of the coffee-ring effect”. *Advances in colloid and interface science* 252 (2018), pp. 38–54.

[96] TPM Alegre, C Santori, G Medeiros-Ribeiro, and RG Beausoleil. “Polarization-selective excitation of nitrogen vacancy centers in diamond”. *Physical Review B* 76.16 (2007), p. 165205. arXiv: 0705.2006.

[97] S Chakravarthi et al. “Window into NV center kinetics via repeated annealing and spatial tracking of thousands of individual NV centers”. *Physical Review Materials* 4.2 (2020), pp. 1–7. arXiv: 1907.07793.

[98] PR Dolan, X Li, J Storteboom, and M Gu. “Complete determination of the orientation of NV centers with radially polarized beams”. *Optics Express* 22.4 (2014), p. 4379.

[99] L Novotny and B Hecht. *Principles of nano-optics*. Cambridge university press, 2012.

[100] I Arun and M Venkatapathi. “Analysis of numerical solutions to Sommerfeld integral relation of the half-space radiator problem”. *Applied Numerical Mathematics* 106 (2016), pp. 79–97.

[101] MY Su and RP Mirin. “Enhanced light extraction from circular Bragg grating coupled microcavities”. *Applied physics letters* 89.3 (2006), p. 033105.

[102] T Erdogan, O King, GW Wicks, DG Hall, EH Anderson, and MJ Rooks. “Circularly symmetric operation of a concentric-circle-grating, surface- emitting, AlGaAs/GaAs quantum-well semiconductor laser”. *Applied Physics Letters* 60.16 (1992), pp. 1921–1923.

[103] M Davanço, MT Rakher, D Schuh, A Badolato, and K Srinivasan. “A circular dielectric grating for vertical extraction of single quantum dot emission”. *Applied Physics Letters* 99.4 (2011), pp. 1–4. arXiv: 1104.0271.

[104] L Sapienza, M Davanço, A Badolato, and K Srinivasan. “Nanoscale optical positioning of single quantum dots for bright and pure single-photon emission”. *Nature Communications* 6 (2015). arXiv: 1503.07141.

[105] H Wang et al. “On-Demand Semiconductor Source of Entangled Photons Which Simultaneously Has High Fidelity, Efficiency, and Indistinguishability”. *Physical Review Letters* 122.11 (2019), pp. 1–6. arXiv: 1903.06071.

[106] J Liu et al. “A solid-state source of strongly entangled photon pairs with high brightness and indistinguishability”. *Nature Nanotechnology* 14.6 (2019), pp. 586–593.

[107] NMH Duong et al. “Enhanced Emission from WSe2 Monolayers Coupled to Circular Bragg Gratings”. *ACS Photonics* 5.10 (2018), pp. 3950–3955. arXiv: 1806.06515.

[108] O Iff et al. “Purcell-enhanced single photon source based on a deterministically placed WSe$_{2}$ monolayer quantum dot in a circular Bragg grating cavity” (2021). arXiv: 2102.02827.

[109] V Karagodsky, FG Sedgwick, and CJ Chang-Hasnain. “Theoretical analysis of subwavelength high contrast grating reflectors”. *Optics Express* 18.16 (2010), p. 16973.

[110] S Fan and JD Joannopoulos. “Analysis of guided resonances in photonic crystal slabs”. *Physical Review B - Condensed Matter and Materials Physics* 65.23 (2002), pp. 1–8.

[111] HQ Zhao, M Fujiwara, and S Takeuchi. “Suppression of fluorescence phonon sideband from nitrogen vacancy centers in diamond nanocrystals by substrate effect”. *Optics Express* 20.14 (2012), p. 15628.

[112] J Zheng, AC Liapis, EH Chen, CT Black, and D Englund. “Chirped circular dielectric gratings for near-unity collection efficiency from quantum emitters in bulk diamond”. *Optics Express* 25.26 (2017), p. 32420. arXiv: 1611.02427.

[113] V Flauraud et al. “Nanoscale topographical control of capillary assembly of nanoparticles”. *Nature Nanotechnology* 12.1 (2017), pp. 73–80.